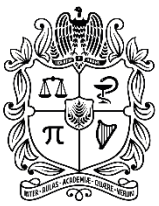

UNIVERSIDAD
NACIONAL
DE COLOMBIA

Fiber Optics Sensing Platform for Monitoring Biological and Chemical Species at Low-concentrations

Brayan de Jesús Patiño Jurado

Universidad Nacional de Colombia
Facultad de Ciencias, Escuela de Física
Medellín, Colombia
2023

Fiber Optics Sensing Platform for Monitoring Biological and Chemical Species at Low-concentrations

Brayan de Jesús Patiño Jurado

Tesis presentada como requisito parcial para optar al título de:

Doctor en Ciencias-Física

(PhD in Physics)

Director:

Ph.D. Jorge Iván García-Sucerquia

Codirector:

Ph.D. Juan F. Botero-Cadavid

Línea de Investigación:

Biosensores a fibra óptica

Grupo de Investigación:

Óptica y Procesamiento Opto-Digital

Universidad Nacional de Colombia

Facultad de Ciencias, Escuela de Física

Medellín, Colombia

2023

Plataforma de Sensado a Fibra Óptica para el Monitoreo de Especies Biológicas y Químicas a Bajas Concentraciones

Brayan de Jesús Patiño Jurado

Tesis presentada como requisito parcial para optar al título de:

Doctor en Ciencias-Física

(PhD in Physics)

Director:

Ph.D. Jorge Iván García-Sucerquia

Codirector:

Ph.D. Juan F. Botero-Cadavid

Línea de Investigación:

Biosensores a fibra óptica

Grupo de Investigación:

Óptica y Procesamiento Opto-Digital

Universidad Nacional de Colombia

Facultad de Ciencias, Escuela de Física

Medellín, Colombia

2023

A mis padres, a mis hermanos y a Crepes

Declaración de obra original

Yo declaro lo siguiente:

He leído el Acuerdo 035 de 2003 del Consejo Académico de la Universidad Nacional. «Reglamento sobre propiedad intelectual» y la Normatividad Nacional relacionada al respeto de los derechos de autor. Esta disertación representa mi trabajo original, excepto donde he reconocido las ideas, las palabras, o materiales de otros autores.

Cuando se han presentado ideas o palabras de otros autores en esta disertación, he realizado su respectivo reconocimiento aplicando correctamente los esquemas de citas y referencias bibliográficas en el estilo requerido.

He obtenido el permiso del autor o editor para incluir cualquier material con derechos de autor (por ejemplo, tablas, figuras, instrumentos de encuesta o grandes porciones de texto).

Por último, he sometido esta disertación a la herramienta de integridad académica, definida por la universidad.

_____

Brayan Patiño-Jurado

Fecha 08/08/2022

Agradecimientos

Agradecimientos por toda la amable colaboración prestada a la Universidad EIA, especialmente al profesor Yeison Montagut Ferizzola, al grupo de investigación de Cerámicos y Vítreos de la Universidad Nacional de Colombia, sede Medellín, dirigido por la profesora Claudia García García y al estudiante de pregrado en Ingeniería Física Arturo Gaviria Calderón. Todo su apoyo y asesoría hicieron posible el desarrollo de esta tesis.

Además, un agradecimiento especial a la Facultad de Ciencias de la Universidad Nacional de Colombia, sede Medellín, por permitir el uso del laboratorio de Óptica, los cursos ofrecidos, el permanente apoyo los miembros de la facultad y los apoyos económicos aprobados que nos permitieron la participación en las conferencias internacionales. Este agradecimiento también se extiende al Programa Curricular de Física y a la Dirección de la Escuela de Física por toda la gestión, trámite administrativo y apoyo económico otorgado durante el desarrollo del doctorado.

Finalmente, un enorme agradecimiento a los miembros del grupo de investigación de Óptica y Procesamiento Opto-digital por todo el apoyo, consejo y acompañamiento en el desarrollo de este trabajo investigativo.

Resumen

El trabajo investigativo llevado a cabo para la producción de esta tesis de doctorado tiene como objetivo fundamental el desarrollo de una plataforma de sensado soportado en tecnología de fibra óptica que permite la detección de especies químicas y biológicas a bajas concentraciones. Este trabajo se presenta como una alternativa de solución al problema que plantea la falta tecnología portátil de sensado en Colombia, que permita hacer medición in situ y en no más de un minuto de bajas concentraciones de sustancias, particularmente de muestras biológicas como la albúmina de suero bovino o la especie Mycobacterium tuberculosis y los niveles de mercurio en el agua. En respuesta a que las técnicas actuales robustas y rápidas de detección y análisis de sustancias, a baja concentraciones, requieren por lo general de equipos costosos, personal especializado y son poco portátiles, lo que difícilmente contribuye a su aplicación en campo y limita la posibilidad de llegar a las poblaciones vulnerables.

En el desarrollo de esta tesis, que parte de una revisión detallada del estado del arte de la problemática de detección y monitoreo de especies químicas como el mercurio en agua y de especies biológica como la Mycobacterium tuberculosis, se evalúan, modelan, diseñan y construyen sensores interferométricos de bajo costo a fibra óptica que pueden ser funcionalizados para hacer reconocimiento químico o biológico específico de la sustancia a detectar. Se estudian, se implementan y se evalúan protocolos de activación y funcionalización que dotan de selectividad en la detección a los sensores desarrollados. Adicionalmente, se evalúa la implementación de los sensores interferométricos en una plataforma diseñada que permite procesar en segundos la respuesta óptica y la transduce en una medida de la concentración de sustancia.

Los resultados de esta tesis de doctorado fueron consolidados en seis manuscritos publicados en revistas indexadas de circulación internacional, cinco presentaciones en eventos internacionales y una solicitud de patente ante la Superintendencia de Industria y Comercio de Colombia. Estos productos constituyen el núcleo de la presente tesis.

Palabras clave: Plataforma de sensado, sensores interferométricos a fibra óptica, mercurio, anti-BSA, estructura SMS, sensores de extremo inclinado.

Abstract

The undertaken research work for this thesis dissertation aims for the development of a fiber optics sensing platform, which allows for the effective detection of chemical and biological species at low concentrations. This work is presented as an alternative solution to the problem posed by a lack of new portable rapid-detection technology in Colombia for the in-situ measurement of low concentrations of certain substances such as the Bovine serum albumin or Mycobacterium tuberculosis sample or the toxic ions mercury in the drinking water. In response to the robust and rapid techniques generally require complex sample preparation procedures, expensive and bulky instruments, and professionally trained personnel, which limits their portability and making them more difficult to implement in the field for vulnerable populations in remote areas.

This thesis dissertation firstly presents the detailed review of the state of the art of problems involved in the detection and monitoring of chemical species such as mercury in water and biological species such as the Anti-BSA and Mycobacterium tuberculosis. Then, the evaluation, modeling, designing and fabrication of cost-effective optics fiber sensors based on interferometric principles is presented in order to determine the ability to functionalize these sensing structures with chemical or biological specific recognition substances. A reliable functionalization and activation protocol was studied, implemented, and evaluated in order to obtain a sensing surface on the optical fiber structures highly selective to detect the substances at low concentrations. Finally, the implementation and integration of the functionalized optical fiber sensor within a designed platform was evaluated with the aim of demonstrating that the rapid and sensible optical response can be processed to determine and display instantly the concentration of substance.

The results of this thesis dissertation were reported on six manuscripts published in peer-review indexed journals, five presentations in international conferences, and a patent filed to the Colombian Superintendence of Industry and Commerce. These products constitute the core of the present thesis.

Keywords: Sensing platform, interferometric fiber optics sensor, mercury, anti-BSA, SMS structure, optical fiber with slanted end.

Contents

List of Figures

Pág.

List of Tables

Pág.

List of symbols and Abbreviatures

Symbols with Latin letters

Symbol	Term	Units SI	Definition
L	Length	nm	Section 0
NA	Numerical Aperture	1	Equation (3.1)
W	radius of the spot of the beam	nm	Equation (3.3
V	Visibility of the interference pattern	1	Equation (3.6)
T	Temperature	°C	Section 3.2.2
I	Intensity	$\mathrm{W/m^2}$	Section 3.2.2
R	Normalized reflection spectrum	1	Equation (3.11)
b	Excitation coefficient	1	Equation (3.13)
M	Total number of excited modes	1	Section 3.3.2
LP	Linearly polarized propagation modes	V/M	Section 3.3.2
z	Propagation distance	m	Section 3.3.2

Symbols with Greek letters

Symbol	Term	Units SI	Definition
λ	Wavelength	nm	Section 0
λ_B	Bragg wavelength	nm	Equation (2.1)
n_{eff}	modal effective refractive index	1	Section 0
Λ	Period of grating	m	Section 0
λ_m	Resonance wavelengths	nm	Equation (2.2)
δ	Phase difference	1	Equation (2.3)
α	Angle of the cone tip	Degrees	Section 3.1.2
n	Refractive index	1	Section 3.1.2
$\Delta\phi$	Optical path difference	1	Section 3.2.2
γ	Complex degree of coherence	1	Section 3.2.2
ξ	Thermo-optic coefficient	$\mathrm{K^{-1}}$	Section 3.3.2
ϕ_m	Excited eigenmodes	$\mathrm{V/m}$	Section 3.3.2
β	Propagation constant	Radians/m	Equation (3.15)
v	Transverse propagation constants	1	Section 3.3.2
θ	Angle of light deflection	Radians	Equation (6.2)

Subscripts

Subscript	Term
Co	Core
Cl	Cladding
m	Modes
0	Vacuum
T	Thin Film
Max	Maximum
Min	Minimum

Superscripts

superscript	Term
Co	Core
Cl	Cladding
m	Modes

Abbreviatures

Abbreviature	Term
BSA	Bovine Serum Albumin
SMS	Single Mode–Multimode–Single Mode
DLHM	Digital Lensless Holographic Microscopy
FBG	Fiber Bragg Grating
LPG	Long Period Fiber Grating
SPR	Surface Plasmon Resonances
LMR	Lossy Mode Resonances
UV	Ultraviolet
PAH	Polyallylamine hydrochloride
PAA	Polyacrylic acid
FPI	Fabry-Perot interferometer
MZI	Mach-Zehnder interferometers
MI	Michelson interferometers
NA	Numerical Aperture
HF	Hydrofluoric acid
RI	Refractive Index
FWHM	Full width at half maximum
TIR	Total internal reflection
RIU	Refractive Index Unit
OSA	Optical Spectrum Analyzer
MMF	Multimode fiber
SMF	Single-mode fiber
E-SMS	Etched SMS

Abbreviature	Term
ICP-MS	Inductively coupled plasma mass spectrometry
ASS	Atomic absorption spectroscopy
AFS	Atomic fluorescence spectrometry
CNC	Computer numerical control
ELISA	Enzyme-linked immunosorbent assays
LOD	Limit of detection
NIR	Near infrared spectrometer
PCR	Polymerase chain reaction

Introduction

1. Introduction and Background

Water contamination by chemical pollutants such as mercury, and highly contagious bacterial diseases such as tuberculosis, are two of the most prevalent public health problems in the world [1]–[3]. Tuberculosis is thought to be responsible for about 2 million deaths every year [3] and it is estimated that about 10 million people in 55 countries are exposed to mercury-contaminated water sources as a result of artisanal mining activities [4], [5]. In Colombia, approximately fifteen thousand people are infected with tuberculosis every year and it is suggested that for at least 80 rivers could be contaminated with mercury [6][7], [8]. In both cases, the prominence of these difficulties is primarily due to the lack of adequate technology for the timely detection and appropriate monitoring of biological and chemical species [9]–[12]. A precise review of the prevalence of these troubles throughout the Colombian territory reveals that, as a consequence of the scarcity of suitable technology for the health care services and drinking water supply systems, remote regions and rural populations are the most affected by the water contamination and the tuberculosis. [13]–[22]

In developing countries, the tuberculosis and the mercury contamination in water are two serious problems compounded by the conditions of poverty [18], [23]. On one hand, tuberculosis is an infectious disease caused by Mycobacterium tuberculosis bacteria that mainly affects the lungs and is one of the 10 major causes of mortality worldwide [3]. In the most recent report from the World Health Organization, it is showed that in developed nations there were less than 10 new cases of tuberculosis per 100.000 inhabitants, whereas

that in developing countries this incidence is somewhere between 200 and 400 cases per 100.000 inhabitants; supporting the fact that the poverty is determining for the prevalence of this pathology [24]. As far is concern to mercury contamination, according to the World Health Organization, it is estimated that 100 million people in 55 countries are dependent on this toxic metal for their livelihoods, mainly through gold small-scale mining activities [2]. Mercury released into environment can be inhaled and absorbed through the skin, accumulating in the liver, brain and bone tissues; causing renal failure disease, disorder of the nervous system, intellectual impairment and even death [4], [25], [26]. In Colombia, classified as the third country that produces the highest pollution of this metal after China and Indonesia, the main sources of mercury contamination are those places where illegal gold mining is carried out [7], [27], [28]. In these artisanal mining sites, due the lack of adequate technology-based pollution controls to reduce emissions of liquid and gaseous pollutants, the mercury is disposed directly on water sources. Levels of mercury in water of up to 3 ug/L have been reported [8], which exceeds concentration permitted level of 2 ug/L in drinking water as stipulated by the World Health Organization [29].

Reduction of the incidence rate of Tuberculosis in vulnerable populations and the anthropogenic sources of mercury pollution in aquatic systems present the common challenge of detecting and monitoring the evolution of low concentration levels of biological and chemical species. With respect to Tuberculosis, the World Health Organization indicates that while this infectious disease is curable with a suitable treatment, detection in early stages, improving diagnostic techniques, and the continuous monitoring are basic requirements that should be improved to encourage the reduction of mortality rates in the world [24]. Similarly, for the problem of the contamination of water sources with mercury, there is a need to improve the detection and analysis techniques in order to measure the concentration of methylmercury produced in water sources, the most toxic form of mercury, which readily can be accumulated in the fish's tissue, shellfish and crustaceans [26]. These animals are, therefore, bioconcentrators and biomagnifiers that act mobilizing methylmercury through the food chains to human beings [30].

The most affordable methods for detection of Tuberculosis are sputum smear microscopy and isolation and cultivation of mycobacteria [31]. Although these diagnostic strategies are simple, inexpensive and highly specific in areas with very high prevalence, their primary limitations include low sensitivity, delay in diagnosis due to the slow growth rate of the

bacteria (this method usually requires 1-2 months for completion), and contamination susceptibility [1], [32], [33]. This often-unreliable results in delayed diagnosis difficult the tuberculosis control, care of the patient and facilities the spread of infection. Sophisticated techniques such as the serologic enzyme-linked immunosorbent assay (ELISA) [34] and the test based on polymerase chain reaction (PCR) DNA detection [35] are faster, more sensitive, and accurate, but requires highly trained personnel, additional reagents, and complex technological devices, which increase the cost of the analysis [36]. On the other hand, the most advanced techniques for the determination and detection of mercury in water include, but are not limited to, the chromatography–inductively coupled plasma mass spectrometry (GC-ICP-MS) [37], [38], the atomic absorbing spectrophotometry (AAS) [39], [40], atomic fluorescence spectroscopy (AFS) [41], inductively-coupled plasma atomic emission spectroscopy (ICP-AES) [42], [43], and high-performance liquid chromatography (HPLC) [44]. Although these powerful techniques have proved effective and reliable, these require complex sample preparation procedures, expensive and bulky instruments, and professionally trained personnel [45]. Therefore, alike in the tuberculosis detection methods, these approaches are not well suited for rapid on-site detection of chemical species and may not even be available for use in developing countries.

In this thesis, the problem of rapid on-site detection and monitoring of biological species as Mycobacterium tuberculosis, or a similar protein as the Anti-BSA (bovine serum albumin), and mercury in low concentration is addressed. To meet the challenge of detecting chemical and biological species with concentrations in order of 1 ug/L and 1ug/mL correspondingly, optical fiber sensors technology was used. This thesis presents the results of very affordable, low-cost and with potential for remote sensing methodologies fiber optics interferometric sensors based on SMS (single mode–multimode–single mode) structures and fibers with slanted ends to rapidly detect biological and chemical species selectively [46]–[49]. Throughout the development of this work, the fiber optics interferometric sensors were modeled, fabricated, functionalized, tested and integrated into a cost-effective (less than $150 USD for materials and manufacturing) and portable platform.

1.1 Justification and research questions

According to the World Health Organization, tuberculosis is one of the leading causes of death from infectious diseases in the world, affects people in more than 180 countries and

it is responsible for nearly 10 million incident cases worldwide, resulting in over 1.5 million deaths each year [24]. In Colombia, almost 15 thousand cases of tuberculosis and more than one thousand deaths for this pathology are reported each year [9]. Concerning this public health problem, the Colombian Government has made a commitment to reduce the incidence of new cases of tuberculosis including as one of the objectives of particular priority in the *Plan Decenal de Salud Pública 2012 – 2021* (Decennial Plan of Public Health 2012-2021) *and* the *Plan Estratégico Colombia Hacia el Fin de la Tuberculosis 2016-2025* (Colombia's Strategic Plan Towards the End of Tuberculosis 2016-2025), the progressive reduction of mortality due to tuberculosis over the whole national territory [50]. It is proposed, consequently, the fundamental challenge of reduction to zero the mortality associated with tuberculosis through monitoring and evaluation of epidemiological behavior of all the cases diagnosed, generating complete, reliable, comprehensive, and timely information in order to guide prevention and control measures of this pathology [6]. However, it is very difficult to achieve these objectives if the conventional methods take a long time to determine diagnosis, in an average of 6 weeks, and the robust methods for detecting tuberculosis are complex and difficult to implement in most infected and affected populations by this disease. Therefore, it is necessary to adapt and improve the technologies used to detect tuberculosis in order to carry out the diagnosis and monitoring in those places where access to health services is poor and limited. In response to this challenge, and as a relevant contribution to the development of biosensors technology, a cost-effective, portable, biocompatible fiber optics sensor is designed, modeled, fabricated and tested in this thesis. This sensor in addition, has the potential for remote sensing and rapid detection of biological species in low concentrations, in the case of tuberculosis it would be able to detect concentrations as low as 1 ug/mL.

On the other hand, in 2011 Colombia ranked first in the list of countries that emit more mercury per capita, predominantly during gold mining and processing activities [27]. However, for 2019, when Colombia agreed to ratify the Minamata Convention for the reduction of mercury pollution, the country was still classified as the third country that produces the highest pollution of this metal [7], [51], in the absence of any new information about total pollution levels of mercury in the atmosphere and water sources. Despite significant efforts of the Government of Colombia during the last decade to control, reduce and ultimately to eliminate the use of mercury in 2023 [7], [52], to date there is an estimate

of 80 rivers contaminated with this toxic element throughout the country [53]. One of the key challenges facing the Colombian government in the *Plan de Acción Sectorial Ambiental de Mercurio* (Mercury environmental sector action plan) in order to reduce to zero the mercury levels for 2023, it is to research and report the level of contamination in water, sediments and air assessing the impact on flora and fauna throughout the length and breadth of the national territory [10]. Undoubtedly, this action plan should include an effective and reliable methodology to measure levels of mercury in water resources.

One of the first measures to be taken is to consolidate the complete inventory and effective monitoring of the abandoned and active sources of mercury in Colombia, because contamination levels are dynamic [54]. Today, it is quite uncertain the contamination status of mercury in rivers and their effluents throughout the national territory, largely because anthropogenic emissions of mercury can be discharged directly into water and soils via rainfalls and spreading to other regions by way of rivers. Therefore, the problem of detecting and monitoring contamination levels of mercury in water is no different to the problem of rapid detection and monitoring of tuberculosis; in both cases, a portable and cost-effective technology which enables the rapid detection of low concentration of substances is required to address these public health problems which particularly affect vulnerable populations in remote regions.

The challenge of rapid detection, in seconds, of low concentrations of mercury in water is addressed in this doctoral thesis. A cost-effective sensor (less than $10 USD for materials and manufacturing) based in fiber optics technology is developed to detect concentrations of mercury in water up to 1 µg/L. This mercury sensor is incorporated, along with the biosensor, into a portable sensing platform which was developed in this work to enable the processing of sensors data and clearly display low-concentration measures of biological and chemical species. The results presented in this doctoral thesis provide answers to the following research questions: 1. How can the fiber optics technology be implemented as biosensors of Mycobacterium tuberculosis or a similar protein such as the Anti-BSA? 2. How can the cone-shaped fiber optics technology be implemented as mercury sensors? 3. How can fiber optics sensors be developed at cost-effective and with the ability to detect concentrations as low as 1 µg/L of mercury in water and 1 µg/mL of Anti-BSA. 4. How can a portable sensing platform based on fiber optics sensors be developed for low-concentration monitoring of biological and chemical species?

1.2 Objectives and structure of the thesis

The main objective of this thesis was to develop a fiber optics sensing platform for monitoring biological species at low concentrations such as the anti-BSA, as a model molecule for potential detection of Mycobacterium tuberculosis, and chemical species such as the mercury. A set of specific objectives were addressed in order to reach the main objective. In this sense, the research questions were answered as the specific objectives contemplated in this doctoral thesis were fulfilled. As a summary, the specific objectives of the thesis were:

i. To evaluate optical fiber sensors based on geometrically modified end tips for measuring refractive index and temperature. The ability to scale up the cone-shaped and a slanted end optical fibers technology from illumination sources to sensors of chemical species was studied with this objective.

ii. To evaluate a sensor based on etched Sigle-Multi-Single mode (SMS) fiber optics structures for measuring refractive index. The geometrical characteristics of the etched SMS sensors that optimize their sensitivity were studied insofar as this objective is achieved.

iii. To identify and evaluate a suitable protocol for immobilizing biomarkers (biological recognition elements), such as BSA or the protein antigen 38kDA, on the surface of the etched SMS sensor. With this objective, the specificity of the SMS sensor for detecting only biological species such as BSA or Mycobacterium tuberculosis in concentration as low as 1 ug/mL was studied.

iv. To identify and evaluate a suitable activation protocol for immobilizing a chemical recognition element on the sensors based on optical fiber with geometrically modified end tips for detecting chemical species such as mercury in water. With this objective, the reflective fiber structures are evaluated as sensors for specific detection of low-concentrations, up to 1 ug/L, of mercury ions in water.

v. To functionalize both the etched SMS structure and the cone-shaped optical fiber and characterize the optical responses in order to obtain the calibration curves.

This objective allowed to determine interest parameters of the sensors such as the sensibility, the limit of detection and the working range.

vi. To design, model, build and evaluate a portable sensing platform which integrates the biosensor and the fiber sensor based on geometrically modified end tip in order to detect in seconds and monitor low-concentrations of the biological and chemical species. Achieved this specific aim, the main objective of this thesis is fulfilled.

Accordingly, the structure of this thesis was shaped providing a detailed description of the background, theory, methodology, and results of the evaluation of each specific objective. Consequently, this thesis is divided as follows:

I. Introduction.

In this section, the identification of the problem, the background of detection methods, the justification of this thesis and the proposed alternatives for detecting and monitoring mercury in water and Mycobacterium tuberculosis are described. At the same time, the research questions and the objectives are enunciated in order to demarcate the thread that runs through the research carried out in this thesis.

II. Optical Fiber Sensors

In this section, the description of the main concepts concerning optical fiber sensors technology related to this thesis are introduced. Throughout the chapter, a brief summary of the most used optical fiber sensors techniques and their applications is presented.

III. Optical Fiber Sensors for Measuring temperature and Refractive Index

In this section, the evaluation of cone-shaped optical fiber, fibers with slanted ends and SMS structures for measuring some physical variables such as temperature and refractive index is presented. The inability of the cone-shaped optical fibers to form an interferometric structure is demonstrated what leads however to study the feasibility of this cost-effective structure as illumination source in Digital Lensless Holographic Microscopy (DLHM). In contrast, the implementation of optical fiber with slanted end tip as cost effective and practical temperature and refractive index

sensors is reported in the second part of this section. In the last part of the chapter the optimization of sensor based on SMS-structures for measuring refractive index is described.

IV. Optical Fiber Sensor for Measuring Mercury in water.

The state of the art of sensors for detecting chemical species in water, the operation principle of sensors based on optical fiber with slated end tip and the SMS structure, and the functionalization protocol for detecting mercury with these sensors is described in detail in the first part of this section. In the second part, the results of the design, modeling and fabrication of the optical fiber sensors is presented. Finally, the procedure for the preparation of the samples and the results of the measured concentrations of mercury in water are reported in the last part of this chapter.

V. Optical Fiber Sensor for Detecting Biological Species.

The background of the biosensor, the operation principle of sensors based on etched SMS structures, and the functionalization protocol for detecting Anti-BSA or Mycobacterium tuberculosis specie with etched SMS sensors is detailed in the first part of this chapter. In the second part of this chapter, the results of the design, modeling and fabrication of sensors based on etched SMS structures are presented. Finally, the procedure for preparation of the samples and the results of measured biological samples are reported in the last part of this chapter.

VI. Fiber Optics Sensing platform for Low-Concentration Monitoring of Biological and Chemical Species.

In this chapter, the state of the art of portable sensing platforms for monitoring of chemical and biological species is revised. Subsequently, the design, modeling, fabrication, integration of sensors and preliminary evaluation is reported in detail. Finally, the fabricated fiber optics sensing platform for low-concentration monitoring of biological and chemical species is evaluated measuring low concentrations of mercury in water and anti-BSA under laboratory conditions.

VII. Conclusions and Recommendations.

This chapter summarizes the conclusions, current and future work consequence of this dissertation.

VIII. Annexes.

The supplementary material used in this thesis and the manuscripts submitted to indexed journals are reported in this last section.

1.3 References for Chapter 1

[1] M. M. Rahman and R. S. Giasuddin, “Tuberculosis,” in *Anwer Khan Modern Medical College Journal*, vol. 3, no. 2, 2012, pp. 3–5.

[2] World Health Organization, *REPORTE DE TUBERCULOSIS GLOBAL 2017 OMS*. 2017.

[3] World Health Organization, “Global tuberculosis report 2018 - Geneva,” 2018. doi: 10.1016/j.pharep.2017.02.021.

[4] G. Liu, Y. Cai, and N. O’Driscoll, *Environmental Chemistry and Toxicology of Mercury*. John Wiley & Sons, Ltd, 2011.

[5] S. L. Zuber and M. C. Newman, *Mercury pollution: A transdisciplinary treatment*, 1st ed. CRC Press, 2016.

[6] M. L. Ospina Martinez, M. E. Martines Duran, O. E. Pacheco Garcia, and H. Quijada Bonilla, “Protocolo de vigilancia En salud pública en Tuberculosis.,” *Ministerio de Salud y Protección Social Colombia.*, 2016. .

[7] T. E. I.-C. DEPARTAMENTO ADMINISTRATIVO DE CIENCIA, “EVALUACION DEL GRADO DE CONTAMINACIÓN POR MERCURIO Y OTRAS SUSTANCIAS TÓXICAS, Y SU AFECTACIÓN EN LA SALUD HUMANA EN LAS POBLACIONES DE LA CUENCA DEL RIO ATRATO, COMO CONSECUENCIA DE LAS ACTIVIDADES DE MINERÍA,” *Minist. salud*, 2018, [Online]. Available: https://www.minsalud.gov.co/sites/rid/Lists/BibliotecaDigital/RIDE/VS/PP/SA/protocolo-sentencia-t622-vcolciencias.pdf.

[8] F. A. Díaz-Arriaga, “Mercurio en la minería del oro: Impacto en las fuentes hídricas destinadas para consumo humano,” *Rev. Salud Publica*, 2014, doi: 10.15446/rsap.v16n6.45406.

[9] M. de Salud, “Plan-estrategico-fin-tuberculosis-colombia-2016-2025,” *Bibl. Digit. Minist. Salud*, 2015.

[10] El Ministerio de Ambiente y Desarrollo, “Plan de Acción Sectorial Ambiental de Mercurio,” 2018. [Online]. Available: http://www.minambiente.gov.co/images/PLAN_NACIONAL_AMBIENTAL_MERCURIO.pdf.

[11] A. R. Arévalo Barea, “El avance de la tuberculosis multiagresiva en los paises que no gerencian los adelantos que brinda la tecnolog{\’\i}a,” *Rev. Médica La Paz*, vol. 21, no. 1, pp. 3–4, 2015.

[12] M. Jaramillo-Grajales *et al.*, “Diagnóstico de tuberculosis: desde lo tradicional hasta el desarrollo actual,” *Med. y Lab.*, 2015, doi: 10.36384/01232576.129.

[13] J. D. Park and W. Zheng, “Human exposure and health effects of inorganic and elemental mercury,” *J. Prev. Med. Public Heal.*, 2012, doi: 10.3961/jpmph.2012.45.6.344.

[14] K. H. Kim, E. Kabir, and S. A. Jahan, “A review on the distribution of Hg in the environment and its human health impacts,” *Journal of Hazardous Materials*. 2016, doi: 10.1016/j.jhazmat.2015.11.031.

[15] I. N. de Salud, “Es hora de actuar. Pon fin a la Tuberculosis,” *Boletín Epidemiológico Sem.*, Mar. 2019.

[16] J. M. Hernández Sarmiento *et al.*, “Tuberculosis in indigenous communities of antioquia, Colombia: Epidemiology and beliefs,” *J. Immigr. Minor. Heal.*, 2013, doi: 10.1007/s10903-012-9688-1.

[17] S. S. de Salud y Protección Social de Antioquia, “SITUACIÓN DE LA TUBERCULOSIS EN EL DEPARTAMENTO DE ANTIOQUIA 2015 - 2016,” *Boletín Inf. para la acción*, May 2017.

[18] C. A. Ugarte Gil, *Tuberculosis: Un enfoque de Derechos Humanos*, 1st ed., vol. 26, no. 1. Colegio Médico del Perú, 2009.

[19] N. Gil, “Los Agentes Comunitarios en Salud como enlaces entre la comunidad y los servicios de salud: una experiencia hacia la eliminación de la tuberculosis en poblaciones vulnerables de Colombia 2012 - 2016,” *reponameRepositorio Inf. la Organ. Int. para las Migr. OIM*, 2017, Accessed: Jan. 22, 2023. [Online]. Available: https://repository.iom.int/handle/20.500.11788/1688.

[20] C. Y. Chen *et al.*, “A Critical Time for Mercury Science to Inform Global Policy,” *Environ. Sci. Technol.*, 2018, doi: 10.1021/acs.est.8b02286.

[21] M. Gaioli, D. Amoedo, and B. D. González, “Impacto del mercurio sobre la salud humana y el ambiente,” *Archivos Argentinos de Pediatria*. 2012, doi: 10.5546/aap.2012.259.

[22] I. C. Casas, E. Gómez, L. M. Rodríguez, S. L. Girón, and J. C. Mateus, “Hacia un plan nacional para el control de los efectos del mercurio en la salud en Colombia,” *Biomedica*, 2015, doi: 10.7705/biomedica.v35i0.2458.

[23] R. A. Benavides, “Desafios, más allá de la producción limpia y la responsabilidad social minera, en Colombia,” *Medio Ambient. Derecho. Rev. electrónica derecho Ambient. Medio Ambient. Derecho. Rev. electrónica derecho Ambient.*, 2012.

[24] WHO, “WHO | Global tuberculosis report 2019,” 2020. doi: .1037//0033-2909.I26.1.78.

[25] M. Lippmann, *Environmental Toxicants: Human Exposures and Their Health Effects:*

Third Edition, 3rd ed. John Wiley & Sons Inc, 2008.

[26] "Methylmercury. A Review of health hazards and side effects associated with the emission of mercury compounds into natural systems," *Food Cosmet. Toxicol.*, 1973, doi: 10.1016/s0015-6264(73)80437-7.

[27] P. Cordy *et al.*, "Mercury contamination from artisanal gold mining in Antioquia, Colombia: The world's highest per capita mercury pollution," *Sci. Total Environ.*, 2011, doi: 10.1016/j.scitotenv.2011.09.006.

[28] J. Pinedo-Hernández, J. Marrugo-Negrete, and S. Díez, "Speciation and bioavailability of mercury in sediments impacted by gold mining in Colombia," *Chemosphere*, 2015, doi: 10.1016/j.chemosphere.2014.09.044.

[29] W. H. O. WHO, "Mercury in Drinking-water, Background document for development of WHO Guidelines for Drinking-water Quality," 2005.

[30] K. H. Kim and R. J. C. Brown, *Mercury: Sources, applications and health impacts*, 1st ed. Nova Science Publishers, Incorporated, 2013.

[31] T. M. Doherty *et al.*, "Effect of sample handling on analysis of cytokine responses to Mycobacterium tuberculosis in clinical samples using ELISA, ELISPOT and quantitative PCR," *J. Immunol. Methods*, vol. 298, no. 1–2, pp. 129–141, Mar. 2005, doi: 10.1016/j.jim.2005.01.013.

[32] M.-C. Dombret, "Tuberculosis pulmonar del adulto," *EMC - Tratado Med.*, 2018, doi: 10.1016/s1636-5410(17)87873-9.

[33] R. McNerney *et al.*, "Tuberculosis diagnostics and biomarkers: Needs, challenges, recent advances, and opportunities," *Journal of Infectious Diseases*. 2012, doi: 10.1093/infdis/jir860.

[34] C. Boehme *et al.*, "Detection of mycobacterial lipoarabinomannan with an antigen-capture ELISA in unprocessed urine of Tanzanian patients with suspected tuberculosis," *Trans. R. Soc. Trop. Med. Hyg.*, vol. 99, no. 12, pp. 893–900, Dec. 2005, doi: 10.1016/j.trstmh.2005.04.014.

[35] C. R. Friedman, M. Y. Stoeckle, W. D. Johnson, and L. W. Riley, "Double-repetitive-element PCR method for subtyping Mycobacterium tuberculosis clinical isolates.," *J. Clin. Microbiol.*, vol. 33, no. 5, 1995.

[36] P. K. Mehta *et al.*, "Immuno-PCR, a new technique for the serodiagnosis of tuberculosis," *Journal of Microbiological Methods*, vol. 139. pp. 218–229, 2017, doi: 10.1016/j.mimet.2017.05.009.

[37] B. Jackson, V. Taylor, R. A. Baker, and E. Miller, "Low-level mercury speciation in freshwaters by isotope dilution GC-ICP-MS," *Environ. Sci. Technol.*, 2009, doi: 10.1021/es802656p.

[38] G. Nageswaran, Y. S. Choudhary, and S. Jagannathan, "Inductively Coupled Plasma Mass Spectrometry," in *Spectroscopic Methods for Nanomaterials Characterization*, Elsevier, 2017, pp. 163–194.

[39] M. Ghaedi, M. R. Fathi, A. Shokrollahi, and F. Shajarat, "Highly selective and sensitive preconcentration of mercury ion and determination by cold vapor atomic

absorption spectroscopy," *Anal. Lett.*, 2006, doi: 10.1080/00032710600622167.

[40] S. Akman, B. Demirata-Ozturk, and N. Tokman, "Atomic Absorption Spectroscopy," in *Food Toxicants Analysis: Techniques, Strategies and Developments*, 1st ed., Elsevier, Ed. 2007, pp. 637–665.

[41] H. Morita, H. Tanaka, and S. Shimomura, "Atomic fluorescence spectrometry of mercury: principles and developments," *Spectrochim. Acta Part B At. Spectrosc.*, 1995, doi: 10.1016/0584-8547(94)00116-D.

[42] J. L. Todolí and J. M. Mermet, "Sample introduction systems for the analysis of liquid microsamples by ICP-AES and ICP-MS," *Spectrochimica Acta - Part B Atomic Spectroscopy*. 2006, doi: 10.1016/j.sab.2005.12.010.

[43] F. X. Han, W. D. Patterson, Y. Xia, B. B. M. Sridhar, and F. Su, "Rapid determination of mercury in plant and soil samples using inductively coupled plasma atomic emission spectroscopy, a comparative study," *Water. Air. Soil Pollut.*, 2006, doi: 10.1007/s11270-006-3003-5.

[44] Q. Hu, G. Yang, Y. Zhao, and J. Yin, "Determination of copper, nickel, cobalt, silver, lead, cadmium, and mercury ions in water by solid-phase extraction and the RP-HPLC with UV-Vis detection," *Anal. Bioanal. Chem.*, 2003, doi: 10.1007/s00216-003-1828-y.

[45] N. Kallithrakas-Kontos and S. Foteinis, "Recent Advances in the Analysis of Mercury in Water - Review," *Curr. Anal. Chem.*, 2015, doi: 10.2174/1573411012011510071203 24.

[46] Y. C. Maya, I. Del Villar, A. B. Socorro, J. M. Corres, and J. F. Botero-Cadavid, "Optical Fiber Immunosensors Optimized with Cladding Etching and ITO Nanodeposition," 2018, doi: 10.1109/IPCon.2018.8527306.

[47] B. Patino-Jurado, J. F. Botero-Cadavid, and J. Garcia-Sucerquia, "Optical Fiber Point-Source for Digital Lensless Holographic Microscopy," *J. Light. Technol.*, vol. 37, no. 22, 2019, doi: 10.1109/JLT.2019.2921307.

[48] B. Patino-Jurado, J. F. Botero-Cadavid, and J. Garcia-Sucerquia, "Step-Index Optical Fibers with 0.88 Numerical Aperture," *J. Light. Technol.*, vol. 37, no. 15, 2019, doi: 10.1109/JLT.2019.2919669.

[49] B. Patiño-Jurado, J. F. Botero-Cadavid, and J. García-Sucerquia, "Analysis of the dependence of the numerical aperture on cone angle in a tapered step-index optical fiber," in *Optics InfoBase Conference Papers*, 2018, vol. Part F123-, doi: 10.1364/LAOP.2018.Tu4A.6.

[50] Colombia Ministerio de Salud y Protección Social, "Plan Decenal de Salud Pública, PDSP, 2012 - 2021: La salud en Colombia la construyes tú," *Minist. salud*, 2013, doi: 10.1177/1757975912453861.

[51] M. M. Veiga and B. G. Marshall, "The Colombian artisanal mining sector: Formalization is a heavy burden," *Extr. Ind. Soc.*, 2019, doi: 10.1016/j.exis.2018.11.001.

[52] F. A. Fajardo Rodríguez, “Convenio de Minamata sobre el mercurio - implicaciones jurídicas de la ratificación : el caso de la Ley 1658 de 2013,” *Univ. los Andes*, pp. 1–26, 2015, Accessed: Jan. 24, 2023. [Online]. Available: http://hdl.handle.net/1992/17816.

[53] M. C. Beltrán Márquez, “Comercialización de oro por parte de mineros de subsistencia en el municipio de Caucasia, Antioquia y problemática asociada.” Universidad Externado de Colombia, 2020, Accessed: Jan. 24, 2023. [Online]. Available: https://bdigital.uexternado.edu.co/handle/001/3601.

[54] S. Vallejos *et al.*, “A selective and highly sensitive fluorescent probe of Hg2+ in organic and aqueous media: The role of a polymer network in extending the sensing phenomena to water environments,” *Sensors Actuators, B Chem.*, 2011, doi: 10.1016/j.snb.2011.05.041.

2. Optical Fiber Sensors

2.1 Introduction and Background

Optical fiber sensors display several features that make them especially attractive for a wide variety of applications in scientific research and technological industrial development [1]. Among the many unique properties of fiber optics sensors their good overall durability, cost-effectiveness, low weight, installation flexibility, possibility of remote sensing, low wear due to corrosion, temperature resistance, and electromagnetic interference immunity are the most prominent [2]. Furthermore, fiber optics sensors have proven to be highly sensitive for detection of environment changes and rapid for monitoring in real-time due primarily to the lineal response that present these optical devices [3][4]. Therefore, relevant to the challenge of developing portable, robust, affordable, and highly sensitive technology, a large number of techniques based on optical fiber sensors have been reported in the last decade as an effort to demonstrate the advantages of using this technology, compared to the traditional sensing methods for detecting external perturbations through physical, chemical, or biological variables [5].

According to their operating principle, variables to measure, parameters or configuration, fiber optics sensors can be classified within a wide variety of schemes [5]. More recently, however, it is becoming very common to find a structure that classifies the techniques based on fiber optics sensors as follows:

i. **Application**: Temperature, intensity, capacitance, pressure, humidity, refractive index, strain, displacement, current, magnetic fields, torsion, bending, vibration, detection of biological or chemical species, among many others [6][7].

ii. **Operating principle:**

   a. **Interferometric**: Mach-Zehnder, Fabry-Perot, Michelson, Sagnac, multimode, and high-birefringence interferometers [8].

b. **Optical Fiber Grating**: Fiber Bragg, chirped fiber Bragg, tilted fiber Bragg, and long period gratings [4].

c. **Distributed Sensors:** Raman, Rayleigh, and Brillouin scattering [9].

d. **Reflectometry sensors:** Based on optical frequency domain or based on optical time domain [10].

iii. **Modulation parameters:** Intensity, phase, wavelength shift, and polarization state [11].

iv. **Number of sensing points:** Point sensors, quasi-distributed sensors, and fully distributed sensors [12].

The vast number of techniques based on fiber optics sensors that have being developed in the last decade are being recently implemented in the industry. Various applications in medicine [13][14], chemistry [4], materials science [15], optics [16], biology [17], and aerospace engineering [18], as well as in industries of energy generation [12], metallurgy [19], gas [19], and oil [20]; have been reported in the literature. In recent years, fiber optics sensor for monitoring chemical or biological species are in the focus of attention because of the increased need for non-destructive, fast, and portable techniques that can monitor low concentration of substances in solutions. This ability of optical fiber sensors to detect with high sensitivity and selectivity substances of interest, brings about new opportunities in biomedical and biochemical applications [21]. Regarding the last-mentioned research field, this thesis has been developed with the aim of contributing to the knowledge on fiber optics interferometric sensors for monitoring chemical and biological species in low concentrations.

In this chapter, the description of the main concepts concerning optical fiber sensors technology are introduced. A brief description of the most used optical fiber sensors techniques is presented throughout this section. In the last part of the chapter, the principles of techniques based on fiber optics interferometric sensors and their applications are detailed.

2.2 Techniques and Applications Based on Optical Fiber Sensors

Fiber optics sensor consists of an optical device through which a physical, chemical, biological, or other measurand interacts with the light guided in a fiber optics, or guided to and returned from an interaction by an optical fiber, to produce a modulated optical signal with information related to the parameter being measured [22]. The basic concept of a fiber optics sensor is shown in Figure 2-1**.** The light of a power source is coupled to the fiber optics and interacts with an external parameter producing a modulated signal which is guided by the fiber and carried to the detector. In the detection and processing system the input measurements information of the external parameter is extracted from this modulated optical signal. Depending on the operating principle of the fiber optics sensor, the sensing system can operate either in transmission-, the light is guided from the source to detector in one-way only; or in reflection-mode, when the light is guided to the sensing region and reflected in the same fiber to the detector [6].

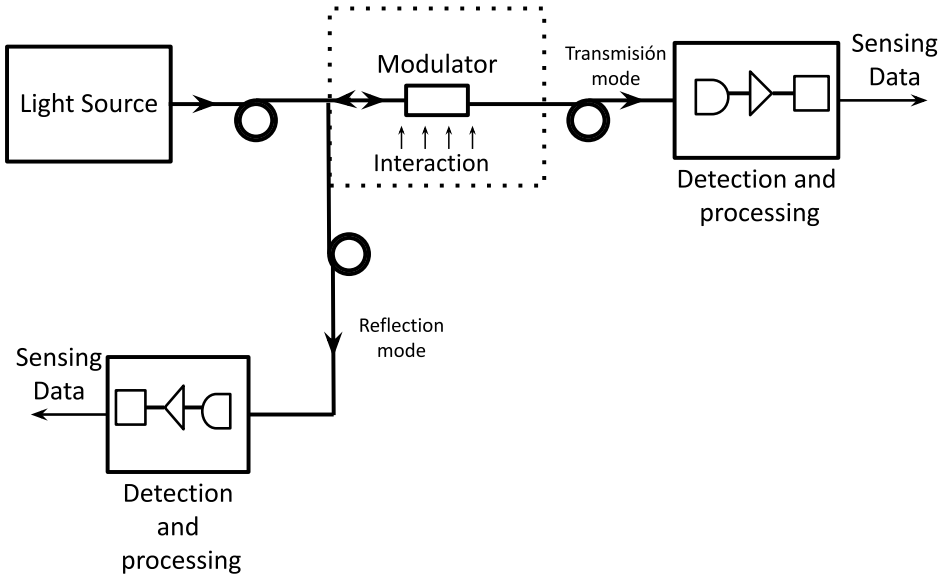

Figure 2-1: Basic scheme of a fiber optics sensor. Adapted from [22]

Considering the working principle, the fiber optics sensors are normally classified as extrinsic and intrinsic. In the former ones, the optical fiber is only a medium to transmit light to and from a separate element or space; while in the latter ones, the optical fiber constitutes the sensing element [11]. Furthermore, depending on the light property that is being

modified with the interaction, or modulation process, fiber optics sensors are typically classified into four main groups:

i. **Intensity-modulated sensors**: In the fiber optics sensors based on this modulation process, the optical signal is transmitted through optical fiber and the irradiance of the light is modulated by various means such as fiber bending, reflectance, or changes in the medium in which the light is transmitted. The cost-effective, easy fabrication, and simple detection system and signal processing requirements are the main advantages of these intensity-modulated sensors [23].

ii. **Phase-modulated sensors:** Also referred to as interferometric sensors, this type of sensors work based on the phase difference of coherent light traveling through two different paths along the same or different optical fibers [8]. These sensors are considered as high-sensitivity sensors because of its proven capability to respond to small changes in the external measurements. Some common fiber sensors of this category include fiber-optic versions of well-known interferometric configurations such as Mach–Zehnder [24], Michelson [8], Fabry–Perot [25], and Sagnac [26].

iii. **Wavelength shift-modulated sensors**: Wavelength-modulated fiber sensors are also known as spectrometric sensors. These optical fiber sensors show a change in the propagating optical wavelength (spectral modulation) when an external perturbation occurs [3]. Some common wavelength-based fiber sensors include Fiber Bragg Grating sensors (FBG) [27], Long Period Fiber Grating Sensors (LPG) [28], Surface Plasmon Resonances (SPR) [29], and Lossy Mode Resonances (LMR) [30].

iv. **Polarization-modulated sensors**: These transductors are also referred to as polarimetric sensors. The light that propagates along a birefringent optical fiber changes its state of polarization due to the difference in the phase velocity of the two polarization modes supported by the fiber [31]. In the fiber optics polarimetric sensors, the polarization properties of the light propagating through an optical fiber can be modulated by stress, strain, pressure, and temperature [32].

There is no doubt that depending on the operating principle, variables to measure, parameters, or configuration for which the sensors are developed, the possibilities of

applications are countless. In this thesis, however, the most common techniques, which include the major applications of fiber optics sensors for chemical and biological detection are described in more detail below: The spectrometric and the interferometric sensors.

2.2.1 Spectrometric Sensors

I. Optical Fiber Gratings.

Sensors based on fiber grating optical technology, including fiber Bragg gratings (FBG) and long-period fiber gratings (LPG), emerged three decades ago and have been widely reported in numerous applications [33]. These types of sensors are extensively applied in the measurement of different physical variables, for instance: temperature, strain, pressure [27] and refractive index [3]; concentration of chemical species [34], and concentration of biological variables such as antigens [35] and proteins [36], thanks to their properties like high sensitivity and high multiplexing capabilities [27].

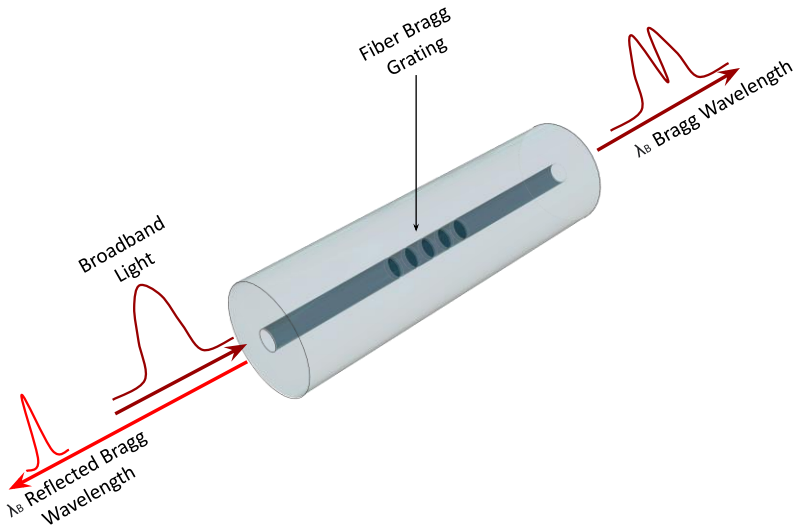

Figure 2-2: Schematic Fiber Bragg grating.

FBG and LPGs consist of periodically spaced modulated refractive index zones in the core of a fiber optics. These sensing devices are typically about 5 mm in length and fabricated commonly using one of three most reported methods which create a periodic variation in the refractive index of the optical fiber's core: i. Applying an intense ultraviolet (UV) light like the one produced by a UV laser [37], ii. Inducing a periodic

mechanical stress [27], or iii. Applying a repeatable electrical discharge [38]. Structurally, both types of gratings are identical except that the FBGs are two orders of magnitude smaller than those of LPGs and the LPGs are known to have high refractive index sensitivity in comparison to its counterpart FBG [39].

FBGs and LPGs operate as surrounding refractive index optical fiber sensors. When a FGB is illuminated by a broadband light source a set of the guide beams in the fiber are reflected of the partially reflecting planes formed by the periodic core index modulation producing interference with each other. This interference is destructive unless each beam is in phase with all the others. By the effect of this interference, FBG reflects a range of wavelengths of light and transmits all others, as shown in Figure 2-2. The reflected wavelength (λ_B), called the Bragg wavelength derived of the Bragg's law, is defined by the following equation [40]:

$$\lambda_B = 2n_{eff}\Lambda \tag{2.1}$$

where n_{eff} is the modal effective refractive index and Λ is the pitch of the periodic core index modulation of the FGB.

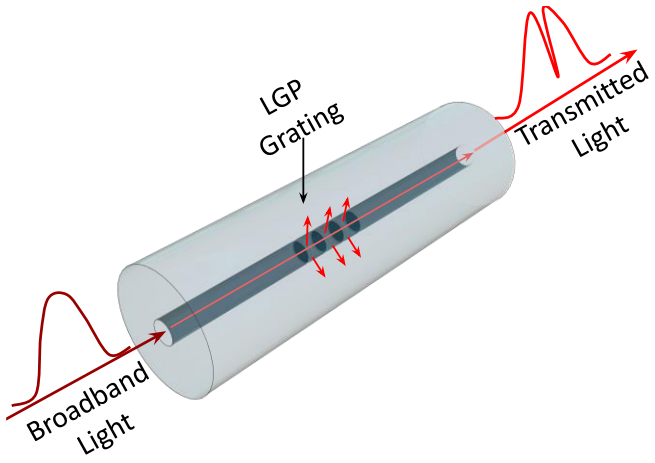

Figure 2-3: Schematic Long Period Fiber grating.

The effective refractive index of the fiber core and the period of the grating, n_{eff} and Λ, vary with physical parameters such as the temperature, the refractive index, and the strain. For this reason, FBGs can be used in sensing applications, by measuring the central wavelength shift of the FBG when any external perturbation, such as stress, strain, voltage,

temperature, etc., is applied to the FBG [40]. In particular, strain and temperature measurements with FBG are the most common sensing applications. 0.6 pm/με, 1 pm/με, and 1.2 pm/με (με = micro-strain) are the typical strain responses of the Bragg wavelength for the Bragg wavelength of around 830, 1300, and 1550 nm, respectively [27]. For its part, the typical temperature responses are approximately 7 pm/°C, 10 pm/°C, and 13 pm/°C, respectively [37]. In addition to the proven advantages of optical fiber sensors, the FGB provides robustness to noise and enables wavelength multiplexing of a great amount of FBG sensors [27].

On the other hand, an LPG promotes coupling between the incident light guided by the fundamental mode in the core and different forward-propagating cladding modes of high diffraction order m in an optical fiber, as shown in in Figure 2-3. The coupling of the light into the cladding region generates a series of attenuation bands centered at discrete wavelength λ_m, each attenuation band corresponding to the coupling to a different cladding mode in the transmission spectrum of the fiber. The resonance wavelengths λ_m of an attenuation band are solutions of the following phase matched conditions [8]:

$$\lambda_m = \left[n_{eff}^{co} - n_{eff}^{cl,m}\right]\Lambda \tag{2.2}$$

where Λ is the period of grating, n_{eff}^{co} is the effective refractive index of the fundamental core mode at the wavelength of λ_m, and $n_{eff}^{cl,m}$ is the effective refractive index of the radial cladding mode m (m = 2, 3, 4, 5...) at the wavelength λ_m. The period of the LPGs, Λ, is in the range from 100 μm to 1 mm, and the length is in the order of 30 mm. $n_{eff}^{cl,m}$ is also a function of cladding refractive index and the refractive index of the surrounding medium [41].

In addition to UV irradiation, electric arc, and mechanical stress; CO_2 laser [42] and femtosecond laser [43] have also been used to fabricate fiber optics sensors based on LPGs. About their applications, LPGs are sensitivity to the resonance wavelengths, which in turn response to the period of the LPFG and the effective refractive index, which is modified by changes from the surrounding medium: temperature, strain, and refractive index, for instance [44].

II. Surface Plasmon Resonances.

The optical fiber sensors based on surface plasmon resonances (SPR) technology have been widely used for the detection of biological and chemical species, as well as for environmental monitoring in the recent decades [29]. SPRs are coherent oscillations of free electrons at the boundary between a metal and dielectric interface stimulated by incident light [45]. For the resonant condition to take place, the propagation constant of the incident light must match the propagation constant of the surface plasmons, which can be accomplished using a glass prism, in an approach known as the Kretschmann SPR configuration [46]. Although this method remains the gold standard for commercial SPR systems, it is bulky, expensive, and it is not suitable for some applications such as remote sensing. In response to these limitations, optical fiber based SPR sensors have been reported, using the fiber optics the role of the prism for coupling the incident light to the metal-dielectric interface is fulfilled to the surface plasmon resonances occur [47].

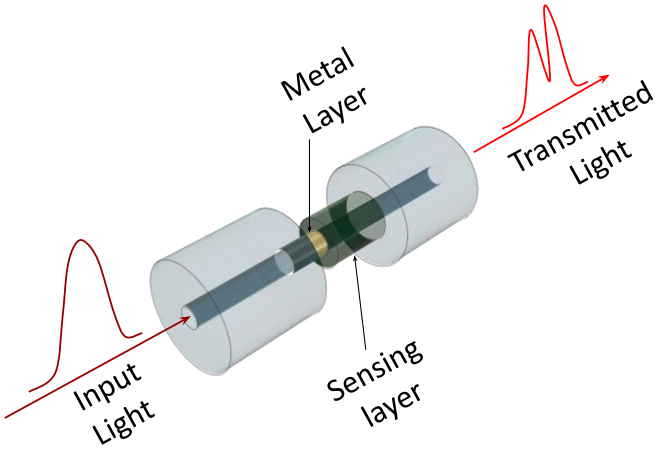

Figure 2-4: A schematic SPR-based fiber optic sensor.

SPR sensors based on fiber optics operate using either wavelength shift or intensity interrogation [48] on a SPR active sensing area that is located either at the end or in the middle of a fiber. In this region the cladding of the optical fiber core is partially or completely removed and this unclad core is coated with a metal layer. The metal layer is further, surrounded by a dielectric sensing layer, as shown in Figure 2-4. The evanescent field produced by the guided beam excites the surface plasmons at the metal-dielectric sensing layer interface. The surface plasmons on the metal surface are affected by the relative permittivities, the wavelength, the fiber geometry, the thin metal film, and the surrounding medium [29]. In the wavelength-interrogation operation, light

of a certain wavelength that impinges at a certain angle produces resonance with the surface plasmons; this wavelength is thus absorbed causing a minimum in the reflectance spectrum. The wavelength of the absorbed light also shifts with the change in the refractive index of the surrounding environment. In the intensity-interrogation operation, the change in intensity is due to refractive-index variation adjacent to the metal surface [49]. D-shape optical fiber and tapered optical fibers are other known configurations to excite plasmons [50], [51].

III. Lossy Mode Resonances.

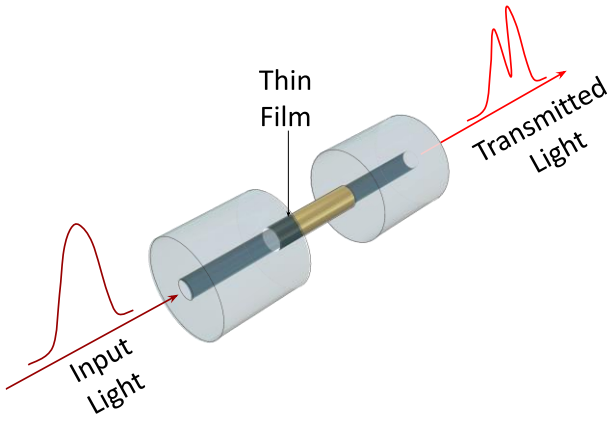

Figure 2-5: A schematic SPR-based fiber optic sensor.

Lossy mode resonances (LMR) occur when the light propagating through a waveguide coated with a support thin-film of appropriate optical properties interacts with this film [30]. If the coating has certain properties, in terms of the real part of the thin-film permittivity, the waveguide modes may couple to coating modes, generating what it is known as a lossy mode which causes an absorption peak at a given wavelength in the transmission spectrum [30], as shown in Figure 2-5. The resonance wavelengths in the spectrum depend on the optical properties (refractive index) of the LMR film, its thickness, and the refractive index of the surrounding medium. In order to generate LMR, the thin-film must have a real positive permittivity part that must also be greater in magnitude than both its imaginary part and the real part of the external medium permittivity. In terms of the refractive index, this means that the chosen thin-film must have a relatively high real part (n) and a comparatively low imaginary part (k). In this respect, LMR can be supported by the fabrication of thin-films made of different materials, such as indium tin oxide (ITO) [52], polymers [53], zinc oxide [54], among others [30].

In terms of applications, LMR are mainly used to develop refractometers because they are only affected by the surrounding media refractive index [30]. This response capacity can be used as the basis for the design of multiple types of sensors to detect chemical and physicals parameters. In addition, given the high number of materials capable of supporting LMR, the fabrication methods and possible combinations are multiple. For instance, an ITO thin-film can be used for the fabrication of hydrogen gas sensors [55] and optical fiber immunosensors [56]; while a zinc oxide thin-film has been used to fabricate a sulfide gas (H_2S) sensors [57]. In recent papers, polymeric coatings of polyallylamine hydrochloride (PAH) were used to fabricate a pH sensor based on LMR [53], and the polyacrylic acid (PAA) thin-film was deposited to generate a relative humidity sensor [58] .

2.2.2 Interferometric Sensors

I. Fiber optics sensors based on Interferometers.

Interferometers based on fiber optics technology to sense various physical parameters such as temperature, strain, pressure, or refractive index have been widely investigated in recent decades [8]. These interferometers operate using the interference between two beams that propagate through different optical paths in a single fiber or through two different fibers. According to their configuration, the interferometric sensors based on fiber optics can be categorized into four types: Fabry-Perot, Mach-Zehnder, Michelson, and Sagnac. In this section, each type of interferometric sensor is briefly reviewed in terms of its operating principles and areas of application.

i. Fabry-Perot Interferometer Sensor

A Fabry-Perot interferometer (FPI) is generally composed of two parallel reflecting surfaces separated a given distance [25]. The interference is generated by the multiple superposition of both reflected and transmitted beams at the two parallel surfaces. Particularly for optical fiber, FPI sensors can be formed based on reflecting surfaces inside (intrinsic FPI sensors) or outside of fibers (extrinsic FPI sensors).

a. Extrinsic FPI sensor:

In this type of Fabry-Perot interferometer, an air cavity is formed by an external support structure. The ends of the fiber serve as parallel reflecting surfaces, as show in Figure

2-6 (a). The fabrication of this type of FPI sensor is relatively simple and high-cost equipment is not required. However, the extrinsic FPI sensors have disadvantages of low coupling efficiency and alignment problem [8]. Despite this, extrinsic FPIs have been applied to a wide range of measurement problems in composites, on metal structures, and on civil structures [59].

b. Intrinsic FPI sensor:

In this type of FPI sensor the air cavity can be formed within the fiber structure by multiple methods that include: Chemical etching [60], micro machining [61], fiber Bragg gratings (FBGs) [62], and thin film deposition [63]. However, they have the problem of high-cost fabrication. The Figure 2-6 (b) shows a schematic of a compact intrinsic FPI sensor.

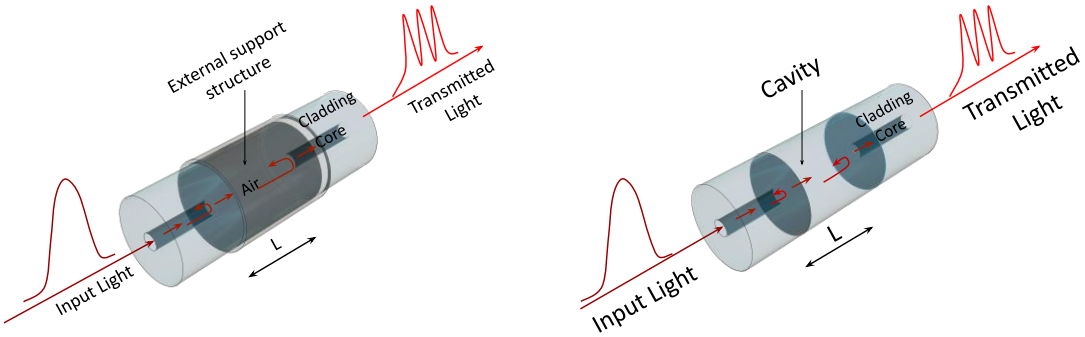

(a) (b)

Figure 2-6: The schematic of a Fabry Perot interferometer sensor. (a) Extrinsic and (b) intrinsic.

The modulated spectrum of a FPI sensor is caused by the optical phase difference between the two reflected or transmitted beams. The maximum and the minimum peaks are generated when both beams, at a wavelength λ, are in 2π phase and out-of-phase, respectively. The phase difference of the FPI is given as [8]:

$$\delta = \frac{2\pi}{\lambda} \cdot 2nL \tag{2.3}$$

where λ is the wavelength of the incident light, n is the refractive index of the cavity material and L is the length of the cavity. In this way, applying a longitudinal strain to the FPI sensor changes the physical length of the cavity or/and the refractive index of

the cavity material, which results in a phase variation [8]. The strain applied on it can be quantitatively obtained by measuring the shift of the wavelength spectrum of a FPI.

ii. Mach-Zehnder Interferometer Sensor

Mach-Zehnder interferometers (MZI) consist of two independent arms: a sensing arm, and a reference arm. A first optical coupler splits the incident light into these two arms that carry the light beams on different optical paths to a second optical coupler that recombines them making them to interfere at the detector plane. In this configuration it is necessary that the reference arm is kept isolated from external disturbances, while only the sensing arm is exposed to variations of the environment [24]. Figure 2-7 shows a schematic of this type of interferometer. MZI based on fiber optics are dependent on the coupling between the guided fundamental mode and higher order modes that induces a phase difference [64]. This phase difference is responsible for the generation of an interference pattern which is used to analyze the parameter of interest such as: refractive index, pH, pressure, temperature, strain, among others [64]. In the literature, various configurations and fabrication techniques have been reported to construct MZI sensors including, for instance: singlemode – multimode – singlemode (SMS) fiber structure [65],[66] mismatched or misaligned core diameter [67], small-waist fiber tapers [68], pair of long period fiber gratings [69], and photonic crystal fiber based structures [70]. In particular, the physical principle of MZI sensors based on SMS structures are in detail described in Chapter 3 of this thesis.

A more compact form of an MZI optical fiber sensor can be obtained by techniques such as the core mismatch, small core, and long period fiber gratings (LPFG) [8]. Figure 2-8 shows a schematic of configuration of the first two MZIs: (a) MZI based on core mismatch and (b) the MZI based on small core.

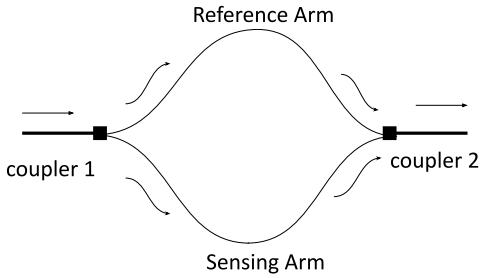

Figure 2-7: Schematic of a Mach-Zehnder Interferometer sensor.

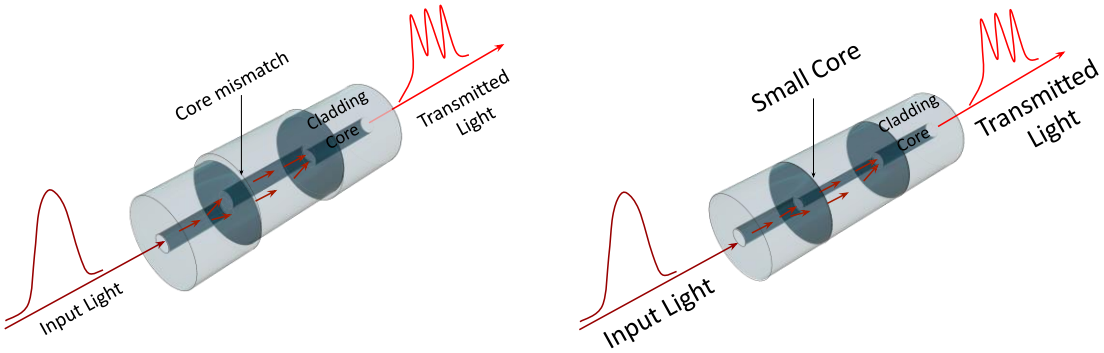

(a) (b)

Figure 2-8: Mach Zehnder interferometer based on: (a) core mismatch, (b) based on small core.

A simple MZI can be fabricated by splicing two fibers with a small intentional deviation, Figure 2-8 (a). In this MZI, light traveling through the core splits and part of it stays guided through the core, while another part excites cladding modes and travels through that region due to the offset. Figure 2-8 (b) shows another MZI, in which a small core fiber is spliced between two optical fibers with larger cores. In this case, the input beam is guided at the small core fiber through both, the core mode and the cladding modes [24].

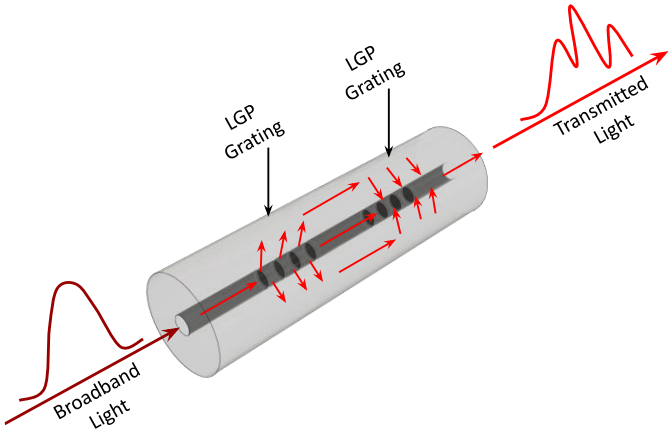

Figure 2-9: Mach Zehnder Interferometer based on long period fiber gratings (LPFG).

For its part, MZI sensors based on LPFG are fabricated by UV-light irradiation, CO_2 or other infrared laser pulses, or mechanical periodical stress [37]–[39], [42] ,[43]. In this type of interferometers light is coupled in a first LPFG from a guided mode into forward propagating cladding modes of the same fiber and later, cladding modes are recoupled

into the core mode by a second LPFG, as shown in Figure 2-9. For this Mach Zehnder interferometer version, both the sensing arm and the reference arm have the same lengths, but different optical paths since the cladding modes have lower effective refractive indexes than that of the core mode beam [8].

iii. Sagnac Interferometer Sensor

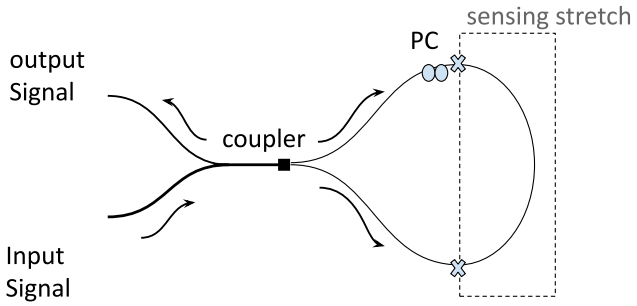

Figure 2-10: The schematic of a Sagnac interferometer sensor

Sagnac interferometer was first demonstrated by Monsieur Sagnac in 1913 [71] and it consists of an optical fiber loop [26]. In this type of interferometer light from a light source splits at the two ends of the loop by a coupler, the beams propagate in opposite directions until being combined again by the same coupler that split the original beam, as shown in Figure 2-10. In the Sagnac interferometer the optical path length is determined by the polarization states depending on the propagating speed of the mode guided along the loop. The polarization states of the propagating light are controlled by a polarization controller (PC) [71]. This type of sensor has been widely investigated in applications such as structure sensing (deformation, torsion, strain, and stress) [72], current [73], acoustic sensing [74], temperature [75], refractive index [8], etc.

Birefringent fibers, fabricated in materials with different indexes of refraction associated with different crystallographic directions, are typically utilized in the sensing stretch. Therefore, the output signal is determined by the interference between the beams polarized along the ordinary and the extraordinary axis [76]. The phase of the interference is given by [8]:

$$\delta = \frac{2\pi}{\lambda} \cdot BL, \ \ where\ B = |n_{eff} - n_0| \tag{2.4}$$

where L is the length of the sensing fiber, n_{eff} and n_0 are the effective indices of the extraordinary and ordinary modes respectively, and λ is the wavelength.

iv. Michelson Interferometer Sensor

Fiber optics sensors based on Michelson interferometers (MI) are quite similar to sensors based on the MZI configuration. In both cases, the basic principle is the interference between the beams in two arms, but in the MI each beam is reflected at the end of each arm [8], as shown in Figure 2-11. The relative phase difference between core mode and cladding modes, with effective refractive index difference Δn_{eff} and the interaction length L, is given as [8]:

$$\delta = \frac{4\pi}{\lambda} \cdot \Delta n_{eff} \ \cdot L \tag{2.5}$$

Several types of MIs have been reported for different configurations on special fibers[11],[3], [15]. For instance, a compact in line configuration of MI based on LPFG can be fabricated from an optical fiber [77], as shown in Figure 2-12. In this configuration, light is coupled from a guided mode into forward propagating cladding modes of the same fiber. Both type of modes, core, and cladding ones, are then reflected by the mirror at the end of the fiber and after travel backwards are recombined by the LPFG where the interference pattern is obtained.

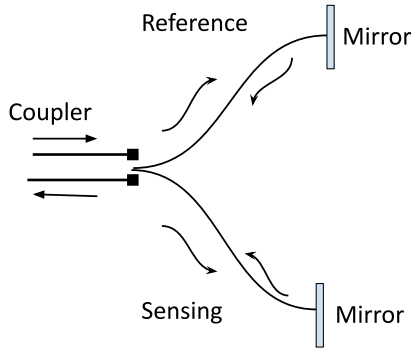

Figure 2-11: The schematic of a Michelson interferometer sensor

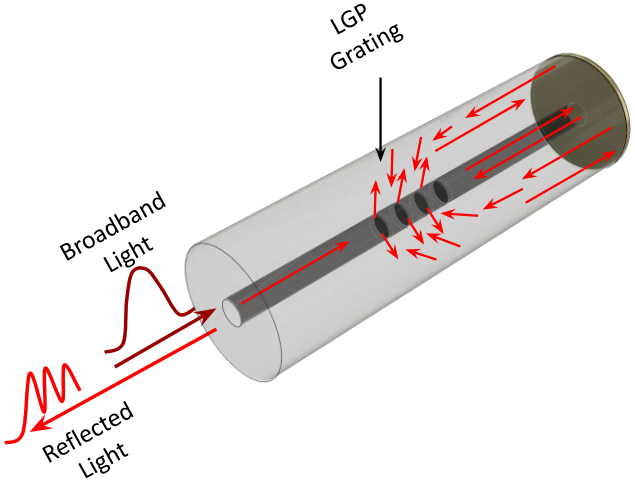

Figure 2-12: Michelson Interferometer based on long fiber grating (LPFG).

Other types of interferometric fiber optics sensors based on Michelson interferometers include fiber taper [78], core-offset structure [79] and peanut-shape fiber structure [80]. These MIs are shown in Figure 2-13. This type of interferometer is especially used for measurements of temperature and refractive index of liquid specimens [8].

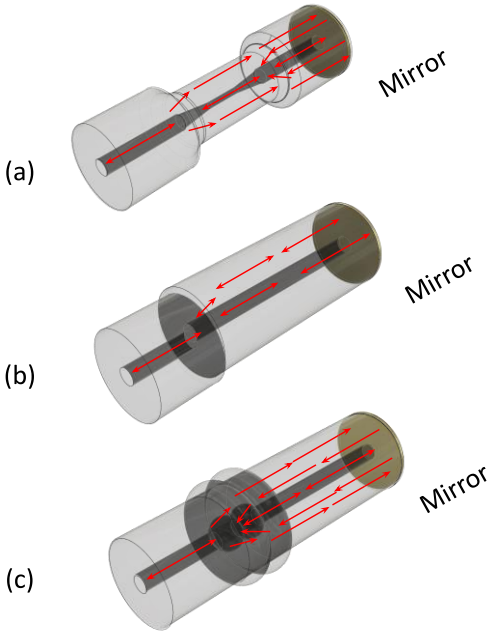

Figure 2-13: Schematic of MIs based on: (a) the fiber taper, (b) the core-offset structure and (c) peanut-shape.

In an MI based on fiber taper, as shown in Figure 2-13 (a) the light in the core is partially coupled into the cladding by the taper. Then, the core and cladding modes are reflected by a mirror and re-coupled by the same taper. In the Figure 2-13 (b), the core-offset structure presents the same behavior on coupling and recoupling between the core and the cladding modes. On the other hand, a MI can be also formed by one peanut-shape structure in SMF based on simple fiber microlens. Here again, high order cladding modes are excited and recoupled to the core modes by the peanut-shape, which functions like splitter and combiner, as shown in Figure 2-13 (c).

2.3 References for Chapter 2

[1] K. Thyagarajan and A. Ghatak, “Optical Fiber,” in *Fiber Optic Essentials*, 1st ed., John Wiley & Sons, 2007, p.82- 256.

[2] E. Udd and W. B. Spillman, *Fiber Optic Sensors: An Introduction for Engineers and Scientists: Second Edition*. 2011.

[3] K. T. V. Grattan and T. Sun, “Fiber optic sensor technology: An overview,” *Sensors Actuators, A Phys.*, 2000, doi: 10.1016/S0924-4247(99)00368-4.

[4] H. E. Joe, H. Yun, S. H. Jo, M. B. G. Jun, and B. K. Min, “A review on optical fiber sensors for environmental monitoring,” *International Journal of Precision Engineering and Manufacturing - Green Technology*. 2018, doi: 10.1007/s40684-018-0017-6.

[5] B. Lee, “Review of the present status of optical fiber sensors,” *Opt. Fiber Technol.*, 2003, doi: 10.1016/S1068-5200(02)00527-8.

[6] “Optical Fiber Sensors: Advanced Techniques and Applications - Google Libros.” https://books.google.com.co/books?hl=es&lr=&id=Vk-3BgAAQBAJ&oi=fnd&pg=PP1&dq=optical+fiber+sensors&ots=YllgpH534-&sig=K-E9UUFH31zpX2fwjPU3VQQLBQk&redir_esc=y#v=onepage&q=optical fiber sensors&f=false (accessed May 02, 2021).

[7] R. A. Perez-Herrera and M. Lopez-Amo, “Fiber optic sensor networks,” *Opt. Fiber Technol.*, vol. 19, no. 6 PART B, pp. 689–699, Dec. 2013, doi: 10.1016/j.yofte.2013.07.014.

[8] B. H. Lee *et al.*, “Interferometric fiber optic sensors,” *Sensors*. 2012, doi: 10.3390/s120302467.

[9] A. Ukil, H. Braendle, and P. Krippner, “Distributed temperature sensing: Review of technology and applications,” *IEEE Sensors Journal*, vol. 12, no. 5. pp. 885–892, 2012, doi: 10.1109/JSEN.2011.2162060.

[10] Z. Ding *et al.*, “Distributed optical fiber sensors based on optical frequency domain reflectometry: A review,” *Sensors*, vol. 18, no. 4, p. 1072, 2018.

[11] H. K. Hisham and H. K. Hisham, “Optical Fiber Sensing Technology: Basics, Classifications and Applications,” *Am. J. Remote Sens.*, vol. 6, no. 1, pp. 1–5, 2018, doi: 10.11648/j.ajrs.20180601.11.

[12] P. Lu *et al.*, “Distributed optical fiber sensing: Review and perspective,” *Applied Physics Reviews*, vol. 6, no. 4. American Institute of Physics Inc., Dec. 01, 2019, doi: 10.1063/1.5113955.

[13] K. K. K. Annamdas and V. G. M. Annamdas, “Review on developments in fiber optical sensors and applications,” in *Fiber Optic Sensors and Applications VII*, Apr. 2010, vol. 7677, p. 76770R, doi: 10.1117/12.849799.

[14] D. Tosi, E. Schena, C. Molardi, and S. Korganbayev, “Fiber optic sensors for sub-centimeter spatially resolved measurements: Review and biomedical applications,” *Opt. Fiber Technol.*, vol. 43, pp. 6–19, Jul. 2018, doi: 10.1016/j.yofte.2018.03.007.

[15] N. Sabri, S. A. Aljunid, M. S. Salim, and S. Fouad, “Fiber optic sensors: Short review and applications,” *Springer Ser. Mater. Sci.*, vol. 204, pp. 299–311, 2015, doi: 10.1007/978-981-287-128-2_19.

[16] B. Patino-Jurado, J. F. Botero-Cadavid, and J. Garcia-Sucerquia, “Optical Fiber Point-Source for Digital Lensless Holographic Microscopy,” *J. Light. Technol.*, vol. 37, no. 22, 2019, doi: 10.1109/JLT.2019.2921307.

[17] A. Leung, P. M. Shankar, and R. Mutharasan, “A review of fiber-optic biosensors,” *Sensors and Actuators, B: Chemical*, vol. 125, no. 2. Elsevier, pp. 688–703, Aug. 08, 2007, doi: 10.1016/j.snb.2007.03.010.

[18] S. Minakuchi and N. Takeda, “Photonic Sensors Review Recent Advancement in Optical Fiber Sensing for Aerospace Composite Structures □,” *Photonic Sensors*, vol. 3, no. 4, pp. 345–354, 2013, doi: 10.1007/s13320-013-0133-4.

[19] J. Li, H. Yan, H. Dang, and F. Meng, “Structure design and application of hollow core microstructured optical fiber gas sensor: A review,” *Optics and Laser Technology*, vol. 135. Elsevier Ltd, p. 106658, Mar. 01, 2021, doi: 10.1016/j.optlastec.2020.106658.

[20] A. G. Leal-Junior, C. Marques, A. Frizera, and M. J. Pontes, “Multi-interface level in oil tanks and applications of optical fiber sensors,” *Opt. Fiber Technol.*, vol. 40, pp. 82–92, Jan. 2018, doi: 10.1016/j.yofte.2017.11.006.

[21] B. Li, H. Xin, Y. Zhang, and Y. Li, “Optical Fiber Technologies for Nanomanipulation and Biodetection: A Review,” *J. Light. Technol. Vol. 39, Issue 1, pp. 251-262*, vol. 39, no. 1, pp. 251–262, Jan. 2021, Accessed: May 02, 2021. [Online]. Available: https://www.osapublishing.org/abstract.cfm?uri=jlt-39-1-251.

[22] G. Rajan, “Introduction to Optical Fiber Sensors,” in *Optical Fiber Sensors*, CRC Press, 2018, pp. 1–12.

[23] P. Roriz, A. Ramos, J. L. Santos, and J. A. Simões, “Fiber optic intensity-modulated sensors: A review in biomechanics,” *Photonic Sensors*, vol. 2, no. 4. Springer, pp. 315–330, Dec. 13, 2012, doi: 10.1007/s13320-012-0090-3.

[24] Y. Zhao, H. Zhao, R. qing Lv, and J. Zhao, “Review of optical fiber Mach–Zehnder interferometers with micro-cavity fabricated by femtosecond laser and sensing applications,” *Optics and Lasers in Engineering*, vol. 117. Elsevier Ltd, pp. 7–20, Jun. 01, 2019, doi: 10.1016/j.optlaseng.2018.12.013.

[25] Z. L. Ran, Y. J. Rao, W. J. Liu, X. Liao, and K. S. Chiang, “Laser-micromachined Fabry-Perot optical fiber tip sensor for high-resolution temperature-independent measurement of refractive index,” *Opt. Express*, 2008, doi: 10.1364/OE.16.002252.

[26] B. Culshaw, “The optical fibre Sagnac interferometer: An overview of its principles and applications,” in *Measurement Science and Technology*, Jan. 2006, vol. 17, no. 1, p. R1, doi: 10.1088/0957-0233/17/1/R01.

[27] A. Méndez, “Fiber Bragg grating sensors: a market overview,” in *Third European Workshop on Optical Fibre Sensors*, Jul. 2007, vol. 6619, p. 661905, doi: 10.1117/12.738334.

[28] P. Pilla *et al.*, “Long Period Grating coated with high refractive index layer,” in *Proceedings of WFOPC2005 - 4th IEEE/LEOS Workshop on Fibres and Optical Passive Components*, 2005, vol. 2005, pp. 370–375, doi: 10.1109/WFOPC.2005.1462157.

[29] J. Homola, S. S. Yee, and G. Gauglitz, “Surface plasmon resonance sensors: review,” *Sensors Actuators, B Chem.*, vol. 54, no. 1, pp. 3–15, Jan. 1999, doi: 10.1016/S0925-4005(98)00321-9.

[30] I. Del Villar *et al.*, “Optical sensors based on lossy-mode resonances,” *Sensors and Actuators, B: Chemical*, vol. 240. Elsevier B.V., pp. 174–185, Mar. 01, 2017, doi: 10.1016/j.snb.2016.08.126.

[31] H. K. Kim, H. G. Park, B. Y. Kim, and S. K. Kim, “Polarimetric fiber laser sensors,” *Opt. Lett.*, vol. 18, no. 4, p. 317, Feb. 1993, doi: 10.1364/ol.18.000317.

[32] “A Polarization-Modulated Fiber-Optic Sensor for Simultaneous Measurement of Two Parameters--《Acta Optica Sinica》2001年01期.” https://en.cnki.com.cn/Article_en/CJFDTotal-GXXB200101021.htm (accessed May 02, 2021).

[33] H. E. Joe, H. Yun, S. H. Jo, M. B. G. Jun, and B. K. Min, “A review on optical fiber sensors for environmental monitoring,” *International Journal of Precision Engineering and Manufacturing - Green Technology*, vol. 5, no. 1. Korean Society for Precision Engineering, pp. 173–191, Jan. 01, 2018, doi: 10.1007/s40684-018-0017-6.

[34] X. Sang, C. Yu, T. Mayteevarunyoo, K. Wang, Q. Zhang, and P. L. Chu, “Temperature-insensitive chemical sensor based on a fiber Bragg grating,” *Sensors Actuators, B Chem.*, vol. 120, no. 2, pp. 754–757, Jan. 2007, doi: 10.1016/j.snb.2006.03.046.

[35] M. P. DeLisa *et al.*, “Evanescent wave long-period fiber bragg grating as an immobilized antibody biosensor,” *Anal. Chem.*, vol. 72, no. 13, pp. 2895–2900, Jul. 2000, doi: 10.1021/ac9912395.

[36] S. Sridevi, K. S. Vasu, S. Asokan, and A. K. Sood, “Sensitive detection of C-reactive protein using optical fiber Bragg gratings,” *Biosens. Bioelectron.*, vol. 65, pp. 251–256, Mar. 2015, doi: 10.1016/j.bios.2014.10.033.

[37] B. Zhang and M. Kahrizi, “High-temperature resistance Fiber Bragg grating temperature sensor fabrication,” *IEEE Sens. J.*, vol. 7, no. 4, pp. 586–591, Apr. 2007, doi: 10.1109/JSEN.2007.891941.

[38] Y. Ouyang, J. Liu, X. Xu, Y. Zhao, and A. Zhou, “Phase-Shifted Eccentric Core Fiber Bragg Grating Fabricated by Electric Arc Discharge for Directional Bending Measurement,” *Sensors*, vol. 18, no. 4, p. 1168, Apr. 2018, doi: 10.3390/s18041168.

[39] Y. J. Rao, “In-fibre Bragg grating sensors,” *Measurement Science and Technology*, vol. 8, no. 4. Institute of Physics Publishing, pp. 355–375, Apr. 01, 1997, doi: 10.1088/0957-0233/8/4/002.

[40] “Fiber Bragg Gratings - 2nd Edition.” https://www.elsevier.com/books/fiber-bragg-gratings/kashyap/978-0-12-372579-0 (accessed May 02, 2021).

[41] D. J. Webb *et al.*, “Spectral Characteristics of Tapered LPG Device as a Sensing Element for Refractive Index and Temperature,” *J. Light. Technol. Vol. 24, Issue 2, pp. 870-*, vol. 24, no. 2, pp. 870-, Feb. 2006, Accessed: May 02, 2021. [Online]. Available: https://www.osapublishing.org/abstract.cfm?uri=jlt-24-2-870.

[42] O. V. Ivanov, “Fabrication of long-period fiber gratings by twisting a standard single-mode fiber,” *Opt. Lett.*, vol. 30, no. 24, p. 3290, Dec. 2005, doi: 10.1364/OL.30.003290.

[43] Z. M. Zheng, Y. Sen Yu, X. Y. Zhang, Q. Guo, and H. B. Sun, “Femtosecond Laser Inscribed Small-Period Long-Period Fiber Gratings with Dual-Parameter Sensing,” *IEEE Sens. J.*, vol. 18, no. 3, pp. 1100–1103, Feb. 2018, doi: 10.1109/JSEN.2017.2761794.

[44] S. W. James and R. P. Tatam, “Optical fibre long-period grating sensors: Characteristics and application,” *Meas. Sci. Technol.*, vol. 14, no. 5, p. R49, Mar. 2003, doi: 10.1088/0957-0233/14/5/201.

[45] T. Allsop, R. Neal, S. Rehman, D. J. Webb, D. Mapps, and I. Bennion, “Characterization of infrared surface plasmon resonances generated from a fiber-optical sensor utilizing tilted Bragg gratings,” *J. Opt. Soc. Am. B*, vol. 25, no. 4, p. 481, Apr. 2008, doi: 10.1364/josab.25.000481.

[46] S. A. Meyer, B. Auguié, E. C. Le Ru, and P. G. Etchegoin, “Combined SPR and SERS microscopy in the Kretschmann configuration,” *J. Phys. Chem. A*, vol. 116, no. 3, pp. 1000–1007, Jan. 2012, doi: 10.1021/jp2107507.

[47] M. Li, S. K. Cushing, and N. Wu, “Plasmon-enhanced optical sensors: A review,” *Analyst*. 2015, doi: 10.1039/c4an01079e.

[48] J. Cao, Y. Sun, Y. Kong, and W. Qian, “The Sensitivity of Grating-Based SPR Sensors with Wavelength Interrogation,” *Sensors*, vol. 19, no. 2, p. 405, Jan. 2019, doi: 10.3390/s19020405.

[49] J. Homola and M. Piliarik, “Surface Plasmon Resonance (SPR) Sensors,” Springer, Berlin, Heidelberg, 2006, pp. 45–67.

[50] J. N. Dash and R. Jha, “Highly sensitive D shaped PCF sensor based on SPR for near IR,” *Opt. Quantum Electron.*, vol. 48, no. 2, pp. 1–7, Feb. 2016, doi: 10.1007/s11082-016-0423-3.

[51] N. Cennamo, G. D’Agostino, M. Pesavento, and L. Zeni, “High selectivity and sensitivity sensor based on MIP and SPR in tapered plastic optical fibers for the detection of l-nicotine,” *Sensors Actuators, B Chem.*, vol. 191, pp. 529–536, Feb. 2014, doi: 10.1016/j.snb.2013.10.067.

[52] P. Zubiate, C. R. Zamarreño, I. Del Villar, I. R. Matias, and F. J. Arregui, “High sensitive refractometers based on lossy mode resonances (LMRs) supported by ITO coated D-shaped optical fibers,” *Opt. Express*, vol. 23, no. 6, p. 8045, Mar. 2015, doi: 10.1364/oe.23.008045.

[53] C. R. Zamarreño, M. Hernáez, I. Del Villar, I. R. Matías, and F. J. Arregui, “Optical fiber pH sensor based on lossy-mode resonances by means of thin polymeric coatings,” *Sensors Actuators, B Chem.*, vol. 155, no. 1, pp. 290–297, Jul. 2011, doi: 10.1016/j.snb.2010.12.037.

[54] A. Ozcariz, M. Dominik, M. Smietana, C. R. Zamarreño, I. Del Villar, and F. J. Arregui, “Lossy mode resonance optical sensors based on indium-gallium-zinc oxide thin film,” *Sensors Actuators, A Phys.*, vol. 290, pp. 20–27, May 2019, doi: 10.1016/j.sna.2019.03.010.

[55] S. K. Mishra, S. P. Usha, and B. D. Gupta, “A lossy mode resonance-based fiber optic hydrogen gas sensor for room temperature using coatings of ITO thin film and nanoparticles,” *Meas. Sci. Technol.*, vol. 27, no. 4, p. 045103, Feb. 2016, doi: 10.1088/0957-0233/27/4/045103.

[56] A. B. Socorro, J. M. Corres, I. Del Villar, F. J. Arregui, and I. R. Matias, “Fiber-optic biosensor based on lossy mode resonances,” *Sensors Actuators, B Chem.*, vol. 174, pp. 263–269, Nov. 2012, doi: 10.1016/j.snb.2012.07.039.

[57] S. P. Usha, S. K. Mishra, and B. D. Gupta, “Fiber optic hydrogen sulfide gas sensors utilizing ZnO thin film/ZnO nanoparticles: A comparison of surface plasmon resonance and lossy mode resonance,” *Sensors Actuators, B Chem.*, vol. 218, pp. 196–204, Oct. 2015, doi: 10.1016/j.snb.2015.04.108.

[58] P. Sanchez, C. R. Zamarreno, M. Hernaez, I. Del Villar, I. R. Matias, and F. J. Arregui, “Considerations for lossy-mode resonance-based optical fiber sensor,” *IEEE Sens. J.*, vol. 13, no. 4, pp. 1167–1171, 2013, doi: 10.1109/JSEN.2012.2227717.

[59] Y. J. Rao, “Recent progress in fiber-optic extrinsic Fabry-Perot interferometric sensors,” *Opt. Fiber Technol.*, vol. 12, no. 3, pp. 227–237, Jul. 2006, doi: 10.1016/j.yofte.2006.03.004.

[60] P. A. R. Tafulo, P. A. S. Jorge, J. L. Santos, and O. Frazão, “Fabry-Pérot cavities based on chemical etching for high temperature and strain measurement,” *Opt.*

Commun., vol. 285, no. 6, pp. 1159–1162, Mar. 2012, doi: 10.1016/j.optcom.2011.11.097.

[61] C. R. Liao, T. Y. Hu, and D. N. Wang, “Optical fiber Fabry-Perot interferometer cavity fabricated by femtosecond laser micromachining and fusion splicing for refractive index sensing,” *Opt. Express*, vol. 20, no. 20, p. 22813, Sep. 2012, doi: 10.1364/oe.20.022813.

[62] L. Li *et al.*, “Integration of miniature Fabry-Perot fiber optic sensor with FBG for the measurement of temperature and strain,” *Opt. Commun.*, vol. 284, no. 6, pp. 1612–1615, Mar. 2011, doi: 10.1016/j.optcom.2010.11.010.

[63] Y. Zhang, H. Shibru, K. L. Cooper, and A. Wang, “Miniature fiber-optic multicavity Fabry–Perot interferometric biosensor,” *Opt. Lett.*, vol. 30, no. 9, p. 1021, May 2005, doi: 10.1364/ol.30.001021.

[64] L. Li, L. Xia, Z. Xie, and D. Liu, “All-fiber Mach-Zehnder interferometers for sensing applications,” *Opt. Express*, vol. 20, no. 10, p. 11109, May 2012, doi: 10.1364/oe.20.011109.

[65] Y. Cardona-Maya, I. Del Villar, A. B. Socorro, J. M. Corres, I. R. Matias, and J. F. Botero-Cadavid, “Wavelength and Phase Detection Based SMS Fiber Sensors Optimized with Etching and Nanodeposition,” *J. Light. Technol.*, 2017, doi: 10.1109/JLT.2017.2719923.

[66] M. Shao, X. Qiao, H. Fu, H. Li, Z. Jia, and H. Zhou, “Refractive index sensing of sMS fiber structure based mach-Zehnder interferometer,” *IEEE Photonics Technol. Lett.*, vol. 26, no. 5, pp. 437–439, Mar. 2014, doi: 10.1109/LPT.2013.2295375.

[67] Q. Rong, X. Qiao, R. Wang, H. Sun, M. Hu, and Z. Feng, “High-sensitive fiber-optic refractometer based on a core-diameter-mismatch mach-zehnder interferometer,” *IEEE Sens. J.*, vol. 12, no. 7, pp. 2501–2505, 2012, doi: 10.1109/JSEN.2012.2194700.

[68] Z. Tian *et al.*, “Refractive index sensing with Mach-Zehnder interferometer based on concatenating two single-mode fiber tapers,” *IEEE Photonics Technol. Lett.*, vol. 20, no. 8, pp. 626–628, Apr. 2008, doi: 10.1109/LPT.2008.919507.

[69] O. Frazão *et al.*, “All-fiber Mach-Zehnder curvature sensor based on multimode interference combined with a long-period grating,” *Opt. Lett.*, vol. 32, no. 21, p. 3074, Nov. 2007, doi: 10.1364/ol.32.003074.

[70] H. Y. Choi, M. J. Kim, and B. H. Lee, “All-fiber Mach-Zehnder type interferometers formed in photonic crystal fiber,” *Opt. Express*, vol. 15, no. 9, p. 5711, Apr. 2007, doi: 10.1364/OE.15.005711.

[71] B. J. Vakoc, G. S. Kino, and M. J. F. Digonnet, “A Novel Fiber-Optic Sensor Array Based on the Sagnac Interferometer,” *J. Light. Technol. Vol. 17, Issue 11, pp. 2316-*, vol. 17, no. 11, pp. 2316-, Nov. 1999, Accessed: May 02, 2021. [Online]. Available: https://www.osapublishing.org/abstract.cfm?uri=jlt-17-11-2316.

[72] X. Fang, “A variable-loop sagnac interferometer for distributed impact sensing,” *J.*

Light. Technol., vol. 14, no. 10, pp. 2250–2254, Oct. 1996, doi: 10.1109/50.541215.

[73] J. Blake, P. Tantaswadi, and R. T. De Carvalho, “In-line sagnac interferometer current sensor,” *IEEE Trans. Power Deliv.*, vol. 11, no. 1, pp. 116–121, 1996, doi: 10.1109/61.484007.

[74] E. Udd, “<title>Fiber-Optic Acoustic Sensor Based On The Sagnac Interferometer</title>,” in *Single Mode Optical Fibers*, Nov. 1983, vol. 0425, pp. 90–95, doi: 10.1117/12.936219.

[75] A. N. Starodumov, L. A. Zenteno, D. Monzon, and E. De La Rosa, “Fiber Sagnac interferometer temperature sensor,” *Appl. Phys. Lett.*, vol. 70, no. 1, pp. 19–21, Jan. 1997, doi: 10.1063/1.119290.

[76] E. De la Rosa, L. A. Zenteno, A. N. Starodumov, and D. Monzon, “All-fiber absolute temperature sensor using an unbalanced high-birefringence Sagnac loop,” *Opt. Lett.*, vol. 22, no. 7, p. 481, Apr. 1997, doi: 10.1364/ol.22.000481.

[77] P. L. Swart, “Long-period grating Michelson refractometric sensor,” *Meas. Sci. Technol.*, vol. 15, no. 8, pp. 1576–1580, Jul. 2004, doi: 10.1088/0957-0233/15/8/025.

[78] Z. Tian, S. S.-H. Yam, and H.-P. Loock, “Refractive index sensor based on an abrupt taper Michelson interferometer in a single-mode fiber,” *Opt. Lett.*, vol. 33, no. 10, p. 1105, May 2008, doi: 10.1364/ol.33.001105.

[79] H. Sun, M. Shao, L. Han, J. Liang, R. Zhang, and H. Fu, “Large core-offset based in-fiber Michelson interferometer for humidity sensing,” *Opt. Fiber Technol.*, vol. 55, p. 102153, Mar. 2020, doi: 10.1016/j.yofte.2020.102153.

[80] D. Wu, T. Zhu, and M. Liu, “A high temperature sensor based on a peanut-shape structure Michelson interferometer,” *Opt. Commun.*, vol. 285, no. 24, pp. 5085–5088, Nov. 2012, doi: 10.1016/j.optcom.2012.06.091.

3. Optical Fiber Sensors for Measuring Temperature and Refractive Index

3.1 Cone-shaped optical fibers for measuring physical variables

3.1.1 Introduction and Background

Fiber optics have been incorporated in many different research fields during the last decades. The telecommunications booming has resulted not only in a growing interest of doing research and development in this area, but also in alternative applications of the optical fibers as sensor and light sources. The versatility of the optical fibers is because of among others, features such as their good overall durability, low weight, installation flexibility, possibility of remote sensing, low decay due to corrosion, temperature resistance, and electromagnetic interference immunity [1]. Furthermore, thanks to its wide use in telecommunications, optical fibers have decreased in price as well as increased their accuracy, composition, and precise dimensions.

An optical fiber end tip, or simply a fiber tip, is an optical microsystem shaped on the end of an optical fiber which is used to modify the manner in which light behaves while interacting with the surrounding environment at the end of the fiber [2]. By modifying the geometry of the distal end of a cylindrical optical fiber in which the light of a monochromatic laser propagates, it is possible to adjust how light emerges from this tip to the surrounding medium and interacts with the enviroment. In this respect, a wide variety of methods has been reported to alter the geometry of the fiber optics ends. These include mechanical processes [3]–[6], thermal processes [7], laser processing [8], [9] and chemical etching processes [10]–[15].

Shaped optical fiber tips are versatile and useful to change how light behaves at the ends of the optical fibers. Therefore, much research has been undertaken on fiber tips which in turn has motivated the development of numerous medical and industrial applications. These include, but are not limited to, material processing, laser ablation of body tissue, light coupling in communication links, microscopy, and spectroscopy [16]. The most common fiber tips are conical, ball, helical groove, and angled tips. The main functions of these fiber tips can include: increase the spot size [17], increase or decrease the light divergence (lenses) [18], achieve omnidirectional illumination (360 °) through the sides of the fiber tip [19], redirect light sideways, and increase or reduce the back reflection .

Some microscopy techniques have incorporated conical-shaped optical fibers as scanning probe. In particular, the Near-field scanning optical microscopes (NSOM) are designed so that a cone tip fiber probe scans the sample by illuminating a nanometric local area, and the transmitted or reflected light in the near field zone is then detected [6], [14]. Another microscopy technique called Photon scanning tunnelling microscope (PSTM) is analogous to the Electron scanning tunnelling microscopy (ESTM), with the difference that PSTM involves tunnelling of photons instead of electrons from the sample surface to the probe tip. In this form of microscopy, the distribution of the evanescent field is produced by the effect of total internal reflection, modulated by the sample and detected into a tapered optical fiber probe [20], [21].

On the other hand, very limited sensing technologies based on cone-shaped optical fibers have been reported in the literature for measuring temperature, as described in [22], and refractive index, among which are the reported in [23],[24]. However, the former presents a very low sensibility to temperature changes and there are only reports of measurements at high temperature ranges (>200 °C). For the second, refractive index changes due to normal concentrations, above 100 μg/mL, are merely demonstrated. Therefore, the starting point of the experimental research conducted in this thesis is the validation of the ability of the cone-shaped optical fiber to detect small changes in temperature and low concentrations of substances in aqueous solutions to scale this shaped-fiber technique from illumination sources to the sensing technology. Considering that the sensing principle of the optical sensors which

probably lead to detect minor changes of temperature of refractive index is interferometry, in this section the formation of an interferometer from a cone-shaped optical fiber is evaluated.

3.1.2 Operating Principles

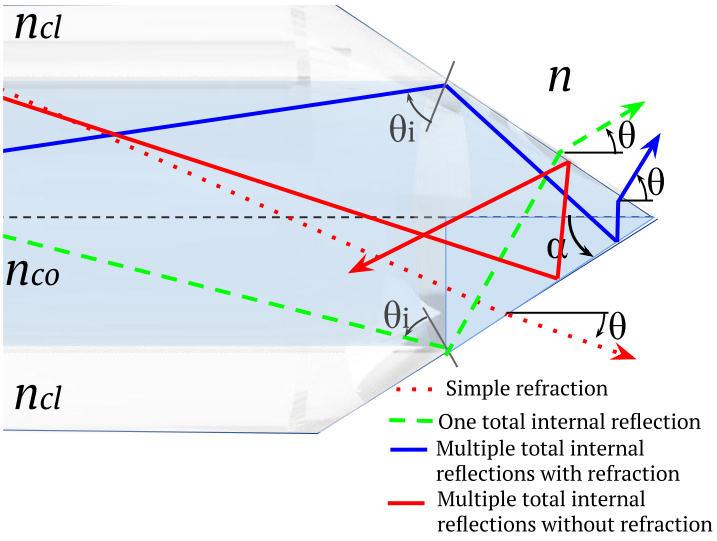

Figure 3-1: Step-index optical fiber with a cone-shaped tip. n, n_{cl} and n_{co} are the refractive indexes of the surrounding medium, the cladding, and the core, in that order. A ray incident on the cone-shaped surface can suffer, depending on α, a simple refraction (red dotted-line), one total internal reflection (green dashed-line), multiple total internal reflections with refraction (blue solid-line), or multiple total internal reflections without refraction (red solid-line).

A conical surface at the distal end of an optical fiber at an angle α is shown in Figure 3-1. A coarse ray tracing analysis in the sagittal plane shows that, when the light propagating in the fiber core impinges on the conical face of the fiber surrounded by air ($n = 1$) can suffer different phenomena according with the angle of the cone tip, α, measured with respect to the optical axis of the step optical fiber: a simple refraction (red dotted-line), one total internal reflection (green dashed-line), multiple total internal reflections (blue solid-line), or multiple total internal reflections without refraction (red solid-line). Among these cases, the latter is the only that could give rise to the formation of an interferometer due to the recombination of two beams. However, a more detailed geometrical analysis, as shown in Figure 3-2 (a), verifies that the formation of two beam with different optical path is not possible unless a thin

film of a dielectric material of refractive index n_T (with $n_T > n_{co}, n_{co}$ the refractive index of the core) is deposited on the conical surface, as shown in the same figure (II). These analyses are validated by means of a numerical study in COMSOL Multiphysics™ on a commercial step index optical fiber (Thorlabs SM600, $n_{\mathrm{co}} = 1.4637$, $n_{cl} = 1.4584$, wavelength $\lambda = 633\, nm$). This analysis demonstrates that only two retroreflected beams are generated to superpose and therefore interfer when the cone-shaped optical fiber is coated with a dielectric material giving rise to the formation of an interference spectrum, which is analyzed from the reflected power flux crossing the output plane placed on the cleaved end, as shown in Figure 3-2 (b).

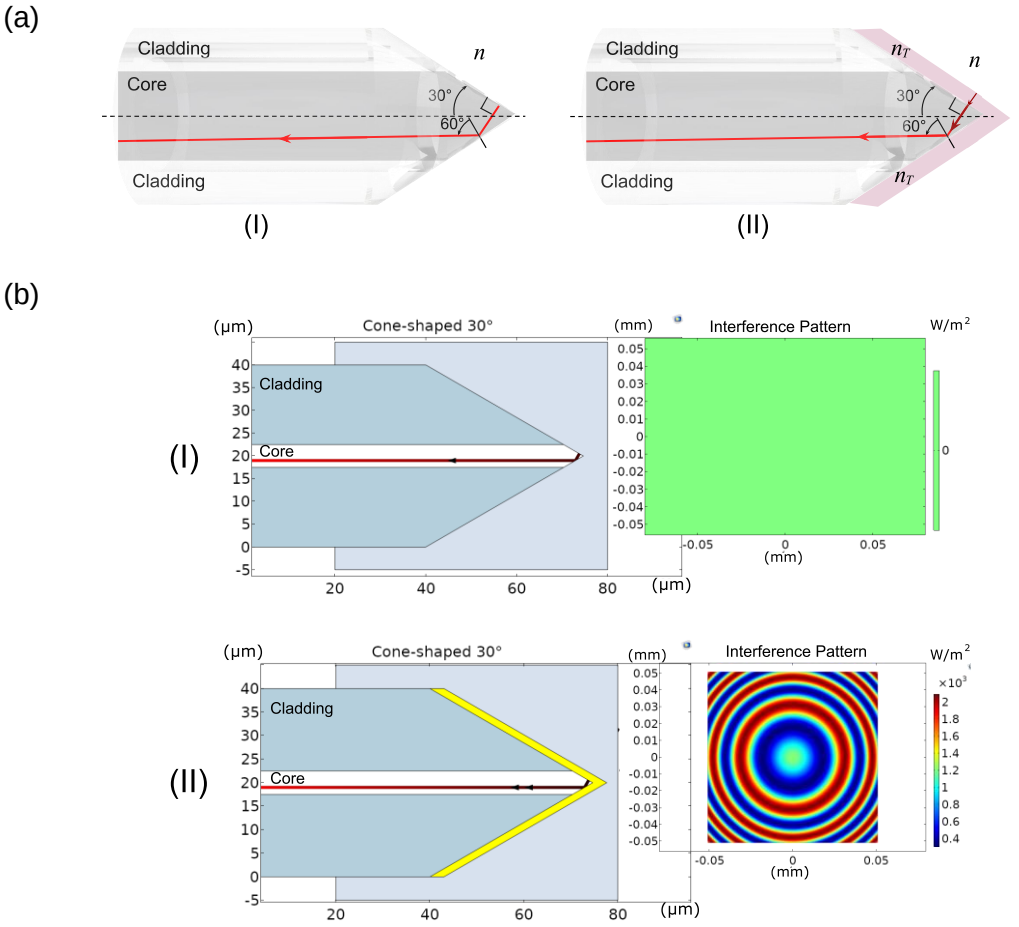

Figure 3-2: (a) (I) Cone-shaped optical fiber without coating and **(II)** with a thin film on the conical surface. **(b)** Numerical validation in COMSOL Multiphysics™. Only two retroreflected beams are generated, superpose and interference when the cone-shaped optical fiber is coating with a dielectric material of refractive index $n_T = 1.5$.

The need to coat in a controlled manner the cone-shaped optical fiber with a thin film of a dielectric material, lessens the development of cost-effective, simple, and easy to implement technology for measuring physical variables such as temperature and refractive index by using this geometry. However, the geometrical analysis carried out until now gives the opportunity to study the design of cone-shaped step-index optical fibers with tunable numerical aperture depending on the refractive index of the surrounding medium n, in such a manner that these shaped fibers immersed in substances with refractive index n can be used as refractive index sensors.

In the most general case, the light guided by the step-index optical fiber undergoes multiple total internal reflection at the conical tip end, as reported in a previous work published by the author of this thesis [25]. As demonstrated in that article, the numerical aperture (NA) at the output of the cone-shaped step-index optical fiber surrounded by a medium with an index of refraction n, is given by:

$$\mathrm{NA}(\alpha) = n\cos\left\{\alpha + \arcsin\left[\frac{n_{\mathrm{co}}}{n}\sin\left(\arcsin\frac{n_{\mathrm{cl}}}{n_{\mathrm{co}}} - (2m+1)\alpha\right)\right]\right\} \tag{3.1}$$

where $m = 1,2,3,\ldots,N$ states for the number of total internal reflections and α is the semi-angle subtended by the cone-shaped optical fiber. The chosen number of total internal reflections m determines the range of angles α for which (3.1) is valid, such that:

$$\left(\arcsin\frac{n_{\mathrm{cl}}}{n_{\mathrm{co}}} - \arcsin\frac{n}{n_{\mathrm{co}}}\right)/(2m+1) < \alpha < \left(\arcsin\frac{n_{\mathrm{cl}}}{n_{\mathrm{co}}} - \arcsin\frac{n}{n_{\mathrm{co}}}\right)/m. \tag{3.2}$$

According to the available manufacturing facilities, (3.1) and (3.2) allow the designer to choose the number of the total internal reflections and therefore, the range of angles that can be fabricated for a given step-index optical fiber. As the fabrication method utilized in this work was static chemical etching applied to a step-index optical fiber (Thorlabs SM600, $n_{\mathrm{co}} = 1.4637$ and $n_{cl} = 1.4584$), $m = 1$ was chosen for the design, which could deliver conical tip semi-angles from 15 to 29 degrees and therefore NAs from 0.02 n to 0.88 n. For purposes of refractive index measurements, in the range of $n = 1$ to $n = 1.5$, in this thesis cone-shaped optical fiber with conical tip semi-angle at 22° (NA=0.6 n) were fabricated and evaluated.

3.1.3 Materials and Methods

The fabrication of the cone-shaped optical fibers was done by means of the Turner method [26]. This static etching is currently the most widely used technique to fabricate cone-shaped optical fibers. It is based on the chemical etching of an optical fiber in an aqueous hydrofluoric acid (HF) solution covered with an organic solvent protection layer [6]. The tip fabrication takes place at the interface of the etching liquid and the protecting layer thanks to the formation of a meniscus which is determined by the acid–protection layer–fiber interface. The cone angle is mainly determined by the height of the meniscus which decreases with time as the fiber diameter decreases due to the etching [27], as shown in Figure 3-3 (a).

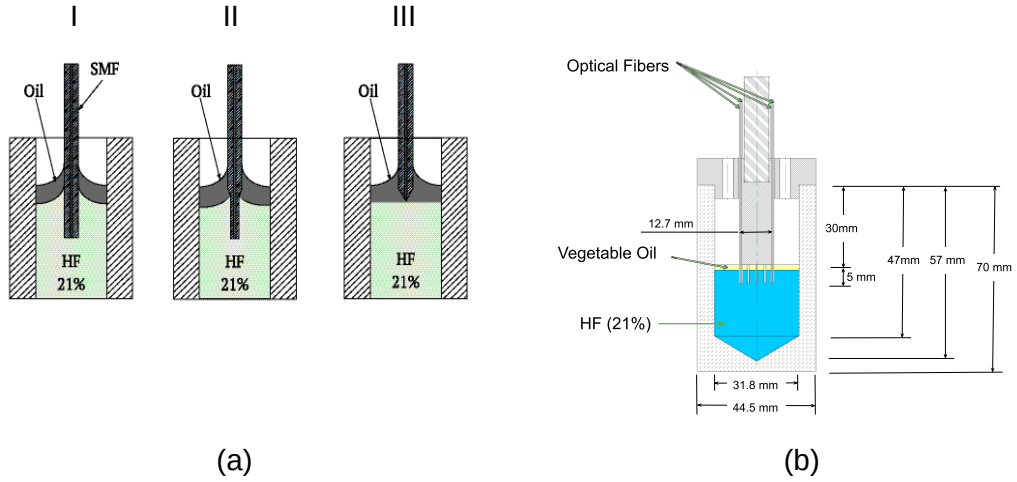

Figure 3-3: (a) Schematic diagram of the fiber during the etching process (I) at the early stages of etching, (II) in the meantime of the process and (III) after 5 hours the cone tip is formed. **(b)** Schematic diagram of the experimental setup used to assist the vertical placement of the optical fiber to be etching.

A Teflon vessel was designed to assist the vertical placement of the optical fibers to be etched, as shown in Figure 3-3 (b). 10 pieces of single mode fiber (Thorlabs SM600) were fastened to the lid of a Teflon vessel guaranteeing the vertical dipping of the fibers into the etchant. The tips of the fibers were prepared before the etching by removing 10 mm of the protective acrylate jacket at the end to be immersed in the etchant. 19 ml of aqueous solution of HF (21%) was poured into the vessel and covered by a 5 mL thin layer of sunflower vegetable oil. This oil cover-layer has two fundamental functions: to form the meniscus between hydrofluoric acid and the fiber to generate the conical tip protecting the rest of the fiber from the etchant, and to protect both the fiber after etching and the environment from toxic HF vapors. The

vessel was covered with the lid containing the aligned optical fibers to be dipped into the etching solution, the etching temperature was maintained at (25 ± 1) °C to form the conical tips with semi-angle at 22° after 20 hours. After each fiber was removed from the vessel, it was immersed in a supersaturated solution of calcium carbonate ($CaCO_3$) to arrest the chemical etching and then rinsed with distilled water.

To study the refractive index (RI) sensing performance of the fabricated cone-shaped optical fibers, a RI response analysis was carried out with the experimental setup shown in Figure 3-4. The cone-shaped optical fibers were put in contact with aqueous NaCl solutions with concentrations of 0, 0.2, 0.4, 0.8, 1.0, 1.7, and 3.4 mol/L, whose corresponding theoretical RI (n) are 1.3095, 1.3119, 1.3131, 1.3143, 1.3188, 1.3210, 1.3285, and 1.3439 [28]. To measure the NA of the fabricated cone-shaped step-index optical fibers, a Gaussian function was used. Under this assumption, the NA is related to the change of the full width at half maximum (FWHM) along a propagation distance Δz according to [29]:

$$\mathrm{NA} = n\sin\left[\arctan\left\{\frac{\Delta FWHM}{\sqrt{2\ln 2}\Delta z}\right\}\right] \tag{3.3}$$

where the FWHM is related to the radius of the spot of the beam w(z) at a distance (z) from the conical tip [29]:

$$w(z) = \frac{FWHM}{\sqrt{2\ln 2}}. \tag{3.4}$$

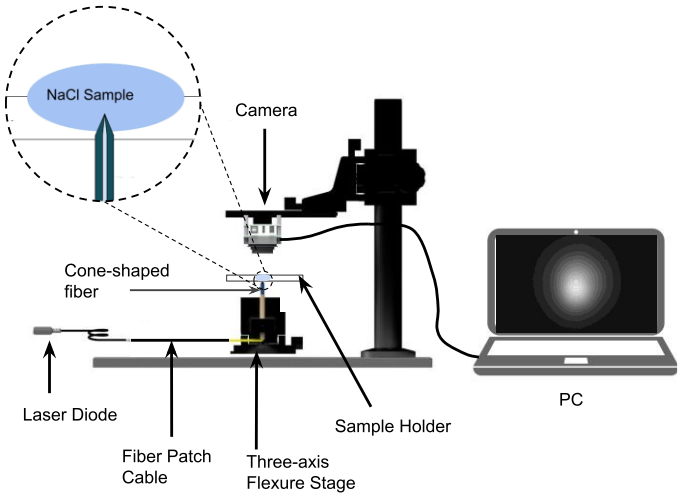

Figure 3-4: Experimental arrangement used for the measurement of the numerical aperture of the cone-shaped step-index optical fibers immersed in NaCl solutions.

Using the aforementioned framework, the different optical fibers with conical tips were spliced into single mode patchcord cables with FC/PC connectors on one end (Thorlabs P1-630A-FC-1); a laser diode emitting at a wavelength of 632.8 nm was coupled to these patchcords. The cone-shaped end of each optical fiber was placed into a side-loading fiber chuck (Thorlabs HFC007) and mounted vertically, as shown in Figure 3-4. The apex of the cone tip submerged in the NaCl solution was placed first at a 4 mm distance from a CMOS camera sensor (Lumenera LU120) where a first spot image was recorded. The camera sensor was then placed 2 mm away from the submerged cone tip and a second spot was registered. The FWHM was determined through a Gaussian fit of the intensity profiles for each recorded spot. With the data of the Gaussian fit and $\Delta z = 2\ \mathrm{mm}$, the NA was finally calculated using equation (3.3).

3.1.4 Results and discussion

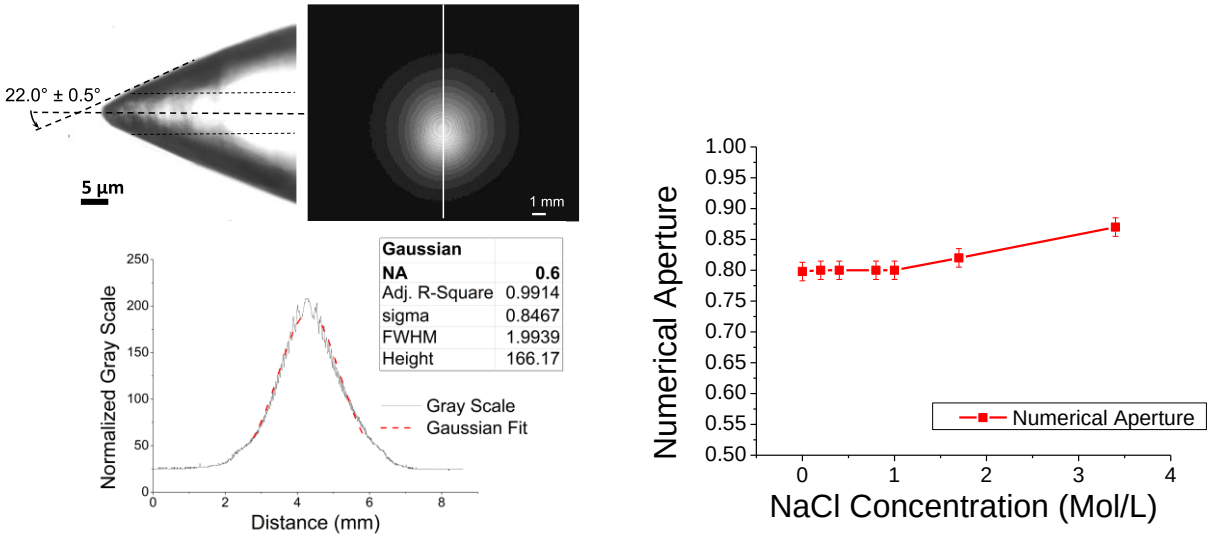

(a) (b)

Figure 3-5: (a) Numerical aperture measurements for the fabricated tip immersed in NaCl solutions. In inset photograph of a cone-shaped step-index optical fiber in air and the recorded illumination spot are shown. Dashed lines represent fiber's core approximate location. The black line is the transverse intensity profile of the spot along the white line and the red dashed line is the Gaussian fit with the parameters in the inset. **(b)** Plot of the numerical aperture vs NaCl concentration for the cone-shaped optical fibers.

A picture of a cone-shaped step-index optical fiber fabricated after 20 hours of etching that produced a semi-angle of 22° and the recorded intensity spot obtained are shown in Figure 3-5 (a). Along the white line over the intensity spot, the illumination profile

was measured and plotted with the black line in panel (b) of the same figure. To validate the premise of Gaussian shape of the intensity spot, the solid line in panel (b) shows the numerical fitting with the parameters presented in the inset. This methodology was repeated for each fabricated cone-shaped optical fiber and for each different aqueous NaCl solution whose concentrations ranges from 0 to 3.4 mol/L. The obtained results of the NA measurements are summarized in the plot of Figure 3-5 (b). The minor refractive index changes could not be detected from the changes in the NA that produce the presence of the different NaCl solutions at the output of the cone tip, only high NaCl concentrations, 1.7 mol/L (0.99 mg/mL) and 3.4 mol/L (199 $\mathrm{mg/mL}$), produce a notable change in the NA. Therefore, it was verified that this sensing methodology was also not a stable and reliable option for measuring refractive index changes of substances at low concentrations.

The results achieved thus far were discouraging because verify that the cone-shaped optical fibers are not a proper alternative to measure refractive index changes of chemical species at low concentrations. However, the literature review and the analytical studio carried out during the course of the research into cone-shaped optical fiber technology led to identify two new research opportunities: Optical fibers with slanted ends for measuring temperature and refractive index and cost-effective cone-shaped optical fibers with tailored NA as point light sources of spherical waves for Digital Lensless Holographic Microscopy. The former is addressed in the following subchapter and the second led to some contributions reported in the following manuscripts submitted to indexed journals of international circulation or presented at an international conference and can be found at the end of this text:

Brayan Patiño-Jurado, Juan F. Botero-Cadavid, and Jorge Garcia-Sucerquia. "Cone-shaped optical fiber tip for cost-effective digital lensless holographic microscopy." Applied optics 59.10 (2020): 2969-2975.

Carlos Buitrago-Duque*, Brayan Patiño-Jurado, and Jorge Garcia-Sucerquia. "Robust and Compact Digital Lensless Holographic Microscope for Label-Free Blood Smear Imaging" HardwareX (2023): e00408.

Carlos Buitrago-Duque, Brayan Patiño-Jurado, and Jorge Garcia-Sucerquia. "Robust Digital Lensles Holographic Microscope for Label-Free Blood Smear Imaging"*".* 10th International Symposium "Optics & its applications. International Centre for Theoretical Physics, 2022.

3.2 Optical fibers with slanted end for measuring temperature and refractive index

3.2.1 Introduction and Background

The demand for reliable high-temperature sensors has become increasingly important over the last decades in different engineering fields, such as turbine engine, structure health monitoring of furnaces, electrical transformers, nuclear reactors, in material processing, and monitoring of exothermic chemical reactions [30], [31]. Compact, resistant, lightweight, with ability to operate remotely, cost-effective, and chemically inert sensing technologies are demanded for the harsh environments in which high-temperature measurements take place [32], [33]. For this purpose, electrical and optical sensors have found a great interest over the last decades becoming the de-facto sensors used to measure temperature in industrial applications [34]. However, the traditional electrical temperature sensors have some disadvantages, including limited sensitivity, low temperature stability, and latent danger of fire accident [35], [36]. Similarly, the measurement of refractive index (RI) is of great significance in diverse research fields and technological applications such as environment monitoring, food safety, biochemistry, and biomedicine, in which cost-effective, accurate and easy to use methods to determine the refractive index of liquids are demanded [37]–[39].

In the last two decades, fiber optics temperature and RI sensors have attracted great interest thanks mainly to their advantages, compared to traditional sensing technologies. These advantaged include: good durability, reliability, small size, biocompatibility, high accuracy, temperature resistance, and electromagnetic interference immunity, [38], [40], [41]. Thus, in general, according with the type of modulation, the different reported temperature and RI based on fiber optics can be classified into two predominant classes: wavelength-modulated and intensity-modulated sensors. The former, such as tapering [24], [42], [43], photonic crystals [16], [44], [45], surface plasmons [46]–[48], long-period grating [49]–[51], fiber Bragg grating [52]–[54], and interferometers [55]–[58] based temperature and RI sensors; have demonstrated high sensitivity (173-370 pm/°C for temperature and 15000-35000 nm/ Refractive Index Unit (RIU), for RI), customized designed, high resolution,

and wide measurement range [58]. However, these wavelength-modulated temperature and RI sensors require precise (and often expensive) equipment for intensity and wavelength measuring, in some cases robust fabrication methods, and are usually sensitive to temperature and strain fluctuations [59], [60]. Conversely, intensity-modulated sensors, such as D-shaped [61], [62], Fabry–Perot interferometers [63], [64], Michelson interferometers (MI) [59], [65], Mach–Zehnder interferometers [66], [67], surface plasmon resonance [68], [69], intensity-modulated fiber Bragg grating sensors [70], [71], and intensity-modulated long-period grating sensors [72], show high sensitivity of RI measurement (-127.2 to -347 dBm/RIU), and temperature measurement (0.02-0.12 dBm/°C) good repeatability, and are often easier to implement than the wavelength-modulated ones, because complex equipment such as spectrometers may not be required [60]. However, in terms of temperature and RI measurements, these approaches have drawbacks including high loss in optical output power because of abrupt increases in RI, complex fabrication methodologies and the requirement of a very stable light source intensity wise.

In response to the mentioned drawbacks, this thesis aims to contribute to the development of a simultaneous wavelength-modulated temperature and an intensity-modulated RI sensor which achieves a sensitivity within the range of formerly reported sensors of its kind, but being inexpensive, compact, and easier to fabricate than others of its type. The second section presents a model that describes the formation of an interference spectrum, the wavelength-modulation due temperature fluctuation, and the intensity-modulation due to RI fluctuation for the sensing probe based on optical fiber with a slanted end. Along with the theoretical analysis, it is included a numerical verification using COMSOL Multiphysics®. Afterwards, the distal end of an optical fiber is mechanically polished to experimentally prove the feasibility of this simple structure to measure temperature changes and RI in NaCl solutions, demonstrating that the sensitivity of this cost-effective sensor can reach to 21.5 pm/°C and -136 dBm/RIU in the RI range from 1.3095 to 1.3439. These sensitivities are comparable to that achieved with other sensors based on Michelson interferometers, as reported in [73], [74] but at a fraction of the cost involved in manufacturing them (at least ten times less costly).

3.2.2 Operating Principles

Theoretical framework

Interferometers can be formed from a slanted surface at the distal end of the fiber at angles of $45°$,$30°$, and $22.5°$, as illustrated in Figure 3-6. A coarse light-ray analysis, based on the Snell's law, shows that when the light propagating in the fiber core impinges on the slanted face of the end of the fiber, one total internal reflection (TIR) takes place. After this TIR, the reflected light reaches the interface of the fiber core and the fiber cladding where it splits into two beams at the interface. One beam I_1 is refracted into the cladding towards the cladding/air interface where the light can suffer: one simple retroreflection, panel (a), one total internal refraction, panel (b), or multiple total internal reflections, panel (c). In the same way, the second beam I_2 in the core can suffer: one simple retroreflection, panel (a), one total internal refraction, panel (b), or multiple total internal reflections, panel (c) on the core/cladding interface. The refracted wave vectors of I_1 and the reflected wave vector of I_2 are guided along the original path and propagate backwards along with a phase difference $\Delta\phi$, superposing and producing an interference at the fiber output whose intensity can be defined by [75]:

$$I = I_1 + I_2 + 2|\gamma|\sqrt{I_1 I_2}\cos\Delta\phi \tag{3.5}$$

where $\Delta\phi = 2\pi L/\lambda$, and L is the optical path difference that can be obtained geometrically for any of the three interferometric structures showed in Figure 3-6. Here n_{cl} is the refractive index of the cladding, r_{cl} is the cladding radius, and r_{co} is the core radius of the optical fiber. For a standard single-mode fiber (Corning SMF-28e), with core diameter of 8.1 μm, cladding diameter of 125 μm, cladding refractive index $n_{cl} = 1.4584$, core refractive index $n_{co} = 1.4637$, and by tuning the angle of the slanted end of the fiber to $45°$, $30°$, and $22.5°$, optical paths differences of $182.6\ \mu m$, $302.3\ \mu m$, and $416.7\ \mu m$ can be achieved respectively. Furthermore, $|\gamma|$ is the complex degree of coherence, $0 \leq |\gamma| \leq 1$, which measures of the ability of the two wave fields to interfere. This term is related to the visibility V of the interference pattern and gives account of the reduction of contrast between $I_{\min}$ and $I_{\max}$, which are two neighboring minimum and maximum of the interference pattern [76]:

$$V = \left(\frac{I_{\max} - I_{\min}}{I_{\max} + I_{\min}}\right) = \frac{2\sqrt{I_1 I_2}}{I_1 + I_2}|\gamma| \tag{3.6}$$

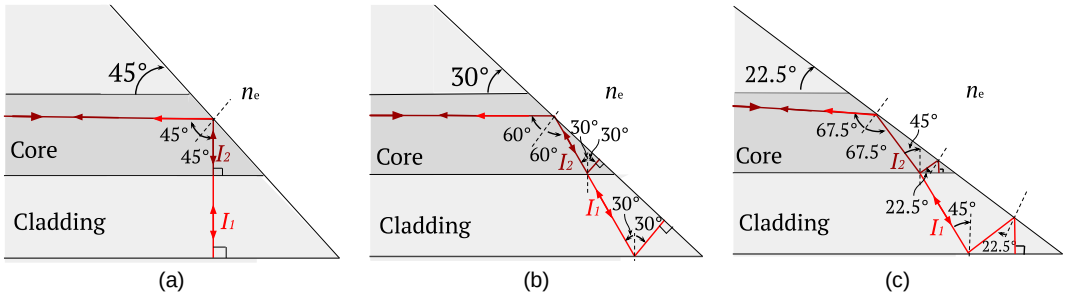

(a) (b) (c)

Figure 3-6: Geometric analysis by ray tracing for three slanted fibers ends with distal end at an angle (a) 45°, (b) 30°, and (c) 22.5°.

In terms of the phase difference $\Delta\phi$, an interference maximum can be obtained when the condition $\Delta\phi = 2\pi L/\lambda = 2m\pi$, with m an integer, is fulfilled. Therefore, the corresponding wavelength of the maximum λ_m can be calculated by $\lambda_m = L/m$. Furthermore, the fringe spacing between two adjacent interference maximums, $m = 2$ and $m = 1$, can be expressed as:

$$\Delta\lambda = \frac{\lambda_2 \lambda_1}{L} \tag{3.7}$$

thus, for optical fibers with angle of the slanted end fiber of $45°$ ($L = 182.6\ \mu\text{m}$), $30°$ ($L = 302.3\ \mu\text{m}$), and $22.5°$ ($L = 416.7\ \mu\text{m}$), fringe spacing of $9.7\ \text{nm}$, $5.9\ \text{nm}$, and $4.2\ \text{nm}$ can be expected when illumination corresponding at $\lambda_2 \cong \lambda_1 = 1330$ nm is used.

On the one hand, optical fiber with their distal end cut at an angle of $45°, 30°$, and $22.5°$ can be analyzed as wavelength-modulated Michelson interferometers fiber sensors for detecting temperature changes. For this purpose, the variation of the position of interference maximum is analyzed with the temperature fluctuation. When the temperature of the slanted fiber end is modified, both refractive index and radius of the fiber are altered because of the thermo-optic effect and the thermal expansion of the fiber [77]. Thus, changes of refractive index of the cladding and the geometry of the fiber in turn modify the optical path difference. This temperature sensitivity can be derived as [77]:

$$\frac{d\lambda_m}{dT} = \left(\frac{1}{n_{cl}} \cdot \frac{dn_{cl}}{dT} + \frac{1}{r_{cl}} \cdot \frac{dr_{cl}}{dT}\right) \cdot \lambda_m = (\xi + \alpha) \cdot \frac{L}{m} \tag{3.8}$$

where ξ is the thermo-optic coefficient and α is the thermal expansion coefficient of the optical fiber, for the silica glass fiber $\xi = 1 \times 10^{-5}\ \mathrm{K}^{-1}$and $\alpha = 1 \times 10^{-6}\ \mathrm{K}^{-1}$. These two coefficients are positive, so they both have a positive contribution to the temperature sensitivity in equation (3.8). As a result, the fluctuation temperature can be monitored by observing the shifting of the maximum, or the minimum, of the wavelength λ_m.

On the other hand, optical fiber with distal end cut at an angle of 45° can be used to detect RI changes of a substance in contact with the cylindrical surface of the cladding, as shown in Figure 3-7 (a). For the other interferometers, those based on optical fiber with their distal end cut at an angle of $30°$ and $22.5°$, RI measurements are not simple to realize due to the rapid loss of power caused by the successive retroflections. However, it has to be taken into consideration that Michelson interference only occurs when light propagating in the fiber core impinges on a fiber-core/air interface, because this condition ensures that TIR takes place. This is owing to the critical angle of TIR being $\arcsin(1/n_{\mathrm{co}}) = 42.9\,° < 45\,°$. Therefore, the slanted face of the end of the fiber cannot be used to measure the refractive index of the surrounding medium n, where $n > 1$. Despite this, the cladding/substance interface, where the light suffers one retroreflection, can be used as the sensing area to obtain refractive index measurements n_S of substances in contact with this surface of the fiber, as show in Figure 3-7 (a). Light propagating in the fiber core I_0 suffers on the slanted face of the end the fiber two retroreflections I_1 and I_2 at the dielectric boundaries core-cladding and cladding/substance. Neglecting the losses, the reflected intensity of the beam I_1 can be obtained by Fresnel equation [76], [78] :

$$I_1 = \left(\frac{n_{co} - n_{cl}}{n_{co} + n_{cl}}\right)^2 I_0. \tag{3.9}$$

Similarly, considering the refractive index of the substance (n_s), the reflected intensity of the beam I_2 can be obtained as:

$$I_2 = \left(\frac{n_{cl} - n_s}{n_{cl} + n_s}\right)^2 I'_0\,, \tag{3.10}$$

where $I'_0 = 4n_{cl}n_{co}I_0/(n_{co}+n_{cl})^2$ is the light refracted into the cladding towards the cladding/substance interface. Thus, the normalized reflection spectrum $R(\lambda)$ can be calculated from equation (3.9) and (3.10) as follows:

$$R(\lambda) = \frac{I(\lambda)}{I_0} = \left(\left(\frac{n_{co}-n_{cl}}{n_{co}+n_{cl}}\right)^2 + \left(\frac{n_{cl}-n_s}{n_{cl}+n_s}\right)^2 \frac{4n_{cl}n_{co}}{(n_{co}+n_{cl})^2}\right)\left(1+V\cos\left(\frac{2\pi L}{\lambda}\right)\right), \quad (3.11)$$

where

$$V = \left(\left(\frac{n_{co}-n_{cl}}{n_{co}+n_{cl}}\right)\left(\frac{n_{cl}-n_s}{n_{cl}+n_s}\right)\frac{\sqrt{4n_{cl}n_{co}}}{(n_{co}+n_{cl})}\right)\cdot\left(\left(\frac{n_{co}-n_{cl}}{n_{co}+n_{cl}}\right)^2 + \left(\frac{n_{cl}-n_s}{n_{cl}+n_s}\right)^2 \frac{4n_{cl}n_{co}}{(n_{co}+n_{cl})^2}\right)^{-1} |\gamma|.$$

This equation expresses the normalized reflection spectrum in terms of the wavelength λ, the refractive index of the solution to be sensed n_s, the geometry of the fiber with slanted end L, and refractive indexes of material of which the fiber is made of. Figure 3-7 (b) shows the plot of the logarithm of the equation (3.11), with λ between $1290\,\text{nm}$ and $1305\,\text{nm}$, under the arbitrary assumption that $|\gamma| = 0.5$, in order to illustrate the behavior for the commercial single mode fiber (Corning® SMF-28e) in contact with substances with theoretical RI (n_s) 1.33, 1.35, and 1.37. As can be seen from that figure, the reflected intensity decreases with the increase of the refractive index.

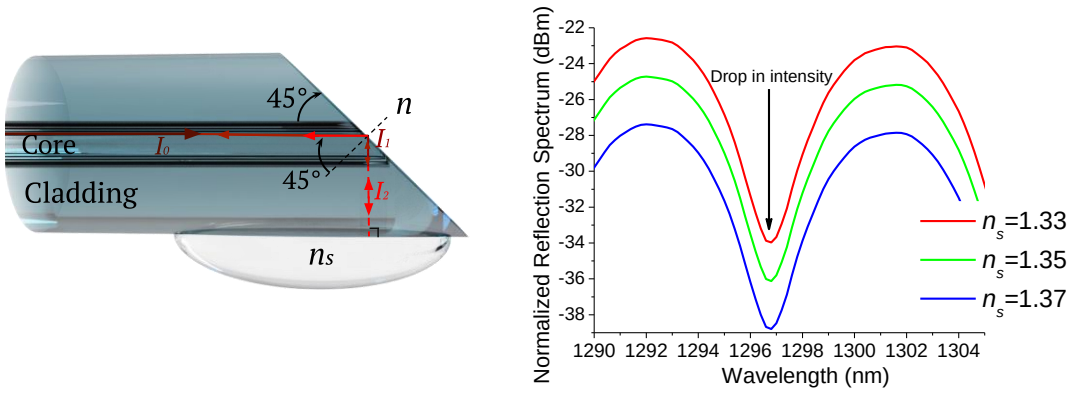

(a) (b)

Figure 3-7: (a) Ray tracing for the slanted fiber end with distal end at an angle of 45°. (b) Plot of equation (3.11) for the commercial single mode fiber (Corning® SMF-28e) in contact with NaCl solutions.

Numerical Analysis

The numerical modeling for the above designed interferometers based on fiber optics with slanted ends was done using COMSOL Multiphysics™ [79]. Standard single-mode step-index optical fibers Corning SMF28e+ surrounded by air with their distal ends cut at 45, 30, and 22.5 degrees were discretized using the standard meshing tool with the mesh setting at Physics-controlled mesh and the element size set to fine. Then, a ray tracing numerical modeling was performed for the tilted end fibers. For this numerical analysis, one ray from a 4-mW He-Ne laser was coupled into each of the modeled distal-end modified fibers, as shown in Figure 3-8. For sake of simplicity only one ray is initially launched from the central point on the proximal face of the cleaved end of the fibers. Note that a secondary ray is emitted for each reflection of the ray at the core/cladding interfaces. The refracted light in this interface is transmitted towards the cladding/air interface where the light suffers one total internal refraction (a), two total internal reflections (b) or a simple retroreflection (c). For its part, the reflected ray suffers one total internal refraction (a), two total internal reflection (b) or a retroreflection (c) on the core/cladding interface. The refracted ray and the reflected ray are guided along the original path and combined into one ray again which propagates backwards causing interference on the output proximal plane which is placed on the cleaved end of the fibers.

The interference pattern obtained at the output of the fiber depends on the radii of curvature, the phase, and the angle of incidence of the two rays as they arrive at the cleaved end [80]. Also, in Figure 3-8 the interference patterns produced by the interferometers based on optical fibers with distal ends cut at (a) 45, (b) 30, and (c) 22.5 degrees are shown. As can be observed, fringe spacing between two adjacent interference peakes is about 10 nm, 6 nm, and 4 nm, respectively. These ray tracing numerical modeling results are consistent with the theoretically forecasted behavior described above.

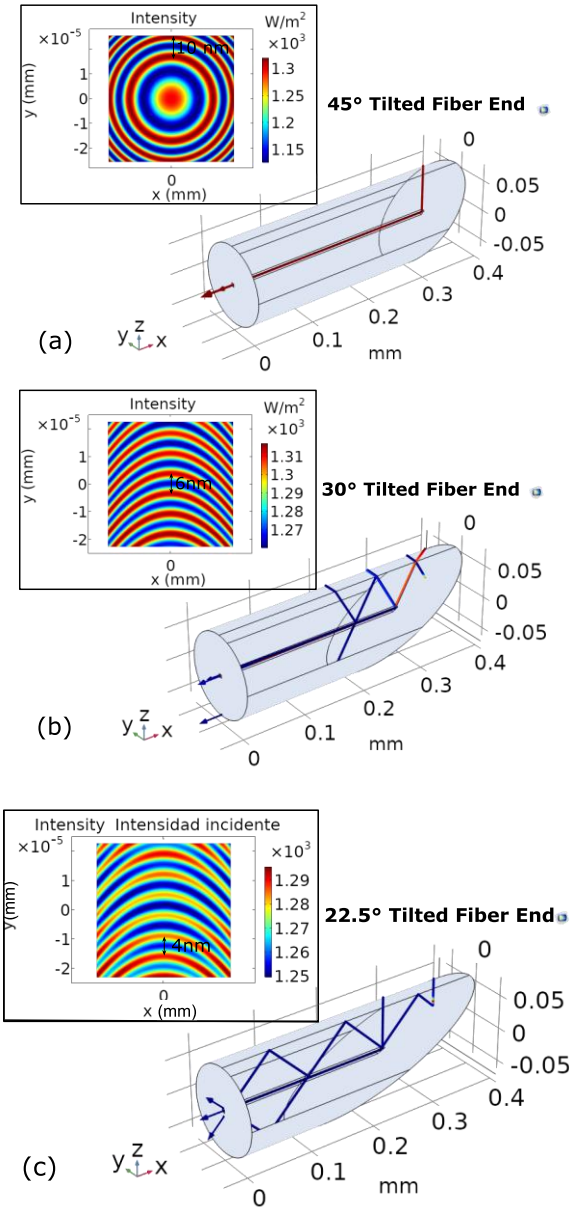

Figure 3-8: Scheme of interferometers based on based on optical fibers with distal ends cut at (a) 45°, (b) 30°, and (c) 22.5 °modeled by ray-tracing using COMSOL Multiphysics™.

On the other hand, the model of the optical fiber with its distal end cut at 45 degrees in contact with a sample that is placed on the external cylindrical surface of the fiber opposing the slanted end was analyzed using the Electromagnetic Wave Propagation Study of COMSOL by exciting a Gaussian beam of a 1300 nm wavelength, with an amplitude of electric field of 1 V/m, and a beam waist of 3500 nm by means of a Scattering Boundary Condition in the proximal flat end of the optical fiber. All the other domain boundaries are modeled using Scattering Boundary Conditions set to zero. As shown in Figure 3-9 (a), the beam propagates through the core fiber, impinges on

the slanted face of the end of the fiber, and experiences a total internal reflection in this interface core/cladding. The reflected beam is split into two beams in the core-cladding interface, one retroreflects into the core and the other one propagates into the cladding towards the cladding/sample interface where the light also retroreflects. The wave vectors of these retroreflected beams superpose and interfere; the interference pattern is analyzed from the reflected power flux crossing the output plane placed on the proximal cleaved end of the fiber. The normalized power crossing this boundary as well as the numerical results of the RI response when the sample is modeled as a NaCl solution with variable refractive index (1.3095, 1.3119, 1.3131, 1.3143, 1.3188, 1.3210, 1.3285, and 1.3439) are also showed in Figure 3-9 (b) and (c). As can be noticed from the slope of the graph, the numerically calculated sensibility of the modeled fiber optics with slanted end is -128.7 dBm/RIU.

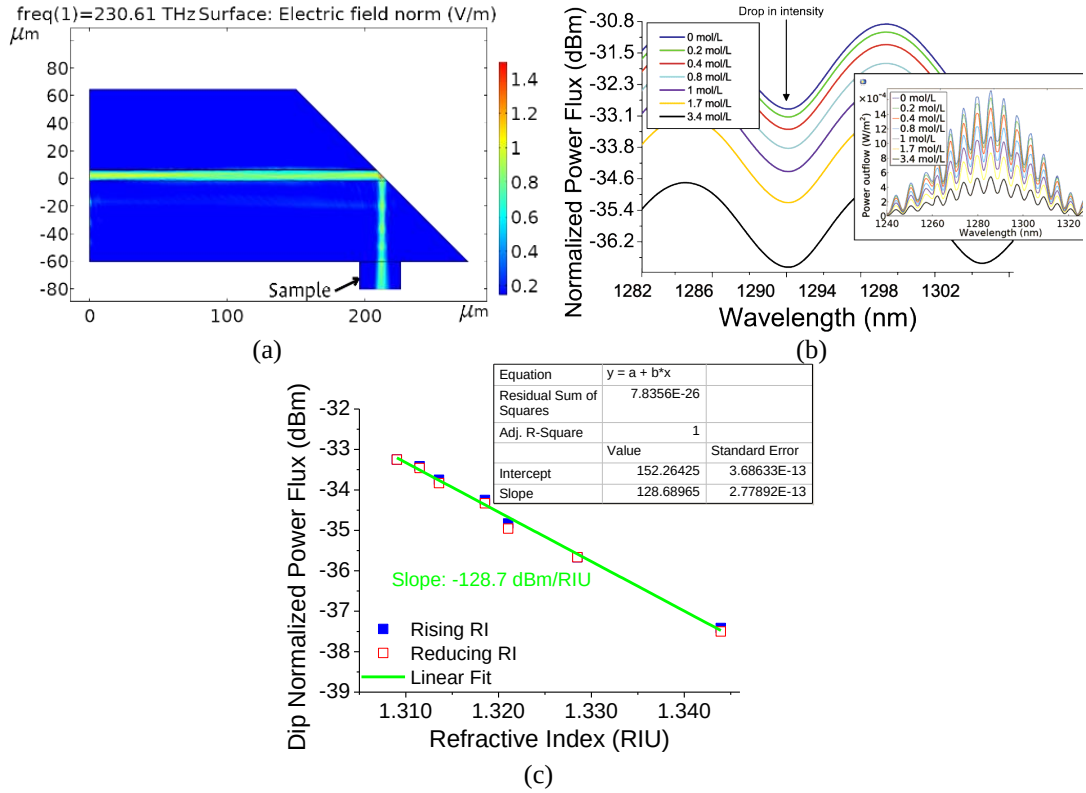

Figure 3-9: (a) Scheme of the optical fiber with slanted end modeled by means of the wave optics module of COMSOL Multiphysics®. (b) Normalized power outflux spectrum with the power outflux spectrum in inset. (c) Numerical results of the power flux responses with the rising and reducing of RI.

3.2.3 Materials and Methods

Fabrication

The fabrication of the slanted fiber ends was done by polishing the distal end on lapping films, as shown in Figure 3-10(a). Thirty slanted fibers ends, ten of each kind, were fabricated at the end of an optical fiber Corning® SMF28e+ with core/cladding diameter of 8.3/125 μm, using CNC machined hand polish pucks with FC/PC connectors. The polishing pucks were designed so that the end of the optical fiber was sloped, with respect to the lapping film, at angles of 45°, 30°, and 22.5°, respectively. The fabrication process of each sensor was completed in two steps: Firstly, three ceramic ferrules with distal ends cut at 45°, 30° and 22.5° were obtained from flat ferrules with 126 μm through-hole. Each FC/PC connector with its ferrule embedded was connected to the slanted polishing puck and placed in contact with a 9 μm diamond lapping film on a slip-free flat working surface. The polishing action took place by gripping this jig with the thumb and forefinger while gently resting it on the polishing lapping moving it with a slight pressure in a shape “8” pattern during five minutes. After obtaining the slanted face on the ferrules, the optical fibers ends were stripped from its polymer jacket and inserted and kept inside the ferrules. A droplet of cyanoacrylate glue kept the fibers inside the connectors. For polishing the fiber, 1 μm diamond lapping film was used in a first grinding stage. After grinding the fiber end face with a slight pressure for about 1 min, coarse 45°, 30° and 45° angled fibers end faces were obtained. To achieve the highest optical properties possible, a second polishing stage using a finer 0.3 μm diamond lapping film and a polishing process of 2 minutes was carried out. Smooth 45°, 30°, and 22.5° angled fibers end faces were thus obtained, as shown in the optical microscopy photographs in Figure 3-10 (b). The slanted angles were measured on the aforementioned images using the angle tool of the open-source software ImageJ [81].

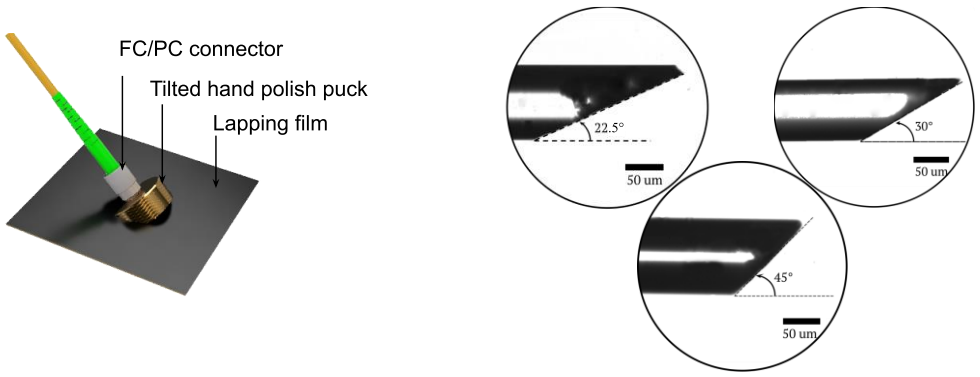

(a) (b)

Figure 3-10: (a) The experimental setup for fabrication of slanted fibers ends by hand polishing using a slanted pucks and lapping films. (b) Optical microscopy images obtained for the optical fibers with their distal end cut at an angle of 22.5°, 30°, and 45°.

Experimental Setup

A temperature analysis was carried out to evaluate the sensing performance of the fabricated sensors based on slanted fibers ends using with the experimental setup shown in Figure 3-11 (a). A SLED S5FC1021S (Thorlabs®) with wavelength in the range of 1240 nm to 1405 nm was used as the light source. The interference pattern was measured using an Optical Spectrum Analyzer (OSA) AQ66370D (Yokogawa Electric). The light from the SLED was coupled into each fiber sensor via a directional coupler TW1300R5F2 (Thorlabs®). The light splits into two beams due to the different reflections of the core and cladding at the slanted surface at the distal end of the fiber sensor, the two beams are retroreflected and their wave vectors are superposed in the fiber core again which propagates backwards causing interference in the output of the fiber which can be observed in the OSA. To study the temperature response of the interferometer pattern, the tip of the optical fiber was placed within a dry block temperature calibrator ETC-400A (Ametek®), which displays an accuracy of ± 0.5° C. For each of the three sensors with distal ends cut at 45°, 30°, and 22.5°, the temperature of the dry block calibrator was gradually risen from 25 °C to 220 °C, with 25 °C steps and then cooled down to room temperature with the same pace of 25 °C per step. At every tested temperature point, the reflection spectrum of the sensor was recorded after the temperature has been steady for 10 min to lead to a more accurate measurement.

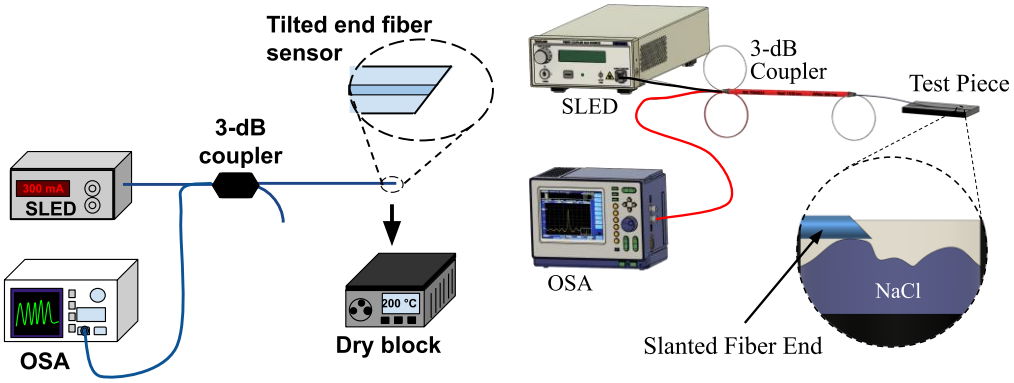

Figure 3-11: (a) The experimental setup used to test the temperature sensing performance of sensors based on slanted fibers ends. (b) The experimental setup used to test the RI sensing performance of fabricated sensor.

Conversely, a study the RI sensing performance of the fabricated sensor based on a slanted fiber end was carried out with the experimental setup shown in Figure 3-11 (b). The same SLED, OSA and directional coupler were also used to measure the reflection spectrum. To study the response of the reflection spectrum in terms of the refractive index of the solution, the optical fiber is placed along the V-groove in the test piece with the slanted surface of the tip facing up, while the NaCl solution in the container was only in contact with the lower cylindrical surface of the optical fiber, as shown in detail in Figure 3-11 (b). RI response was recorded when the cylindrical surface of cladding of the fiber tip was in contact with NaCl solutions whose concentrations range varies from 0 to 3.4 mol/L.

3.2.4 Results and discussion

Temperature Sensor based on Optical Fibers with Slanted Ends

To study the effect of temperature on the interference spectrum recorded by the OSA, one of the interference peaks on each pattern was taken. For the 45° slanted end it was chosen the interference peak at a wavelength near 1313nm; around 1283 nm for the 30°slanted end, and around 1315 nm for the 22.5° slanted end. As can be observed in the insets of Figure 3-12, the fringe spacing between two adjacent interference maxima for each interference pattern were 9.9 nm, 6.5 nm, and 4.1 nm

respectively, which agrees with the fringe spacing calculated in equation (3.7). The behavior of the interference patterns for the complete temperature swept, raising the temperature up to 220 °C, is also shown in Figure 3-12. A very stable shift of each pattern occurs with the increase of temperature. To study the sensitivity, a quadratic fitting is used to all data from each temperature response graph. The temperature response curve shows a slight nonlinear nature due to the nonlinearity of thermo-optic effect in a large and high temperature range. The slope of each fit curve was used to calculate the temperature sensitivity, which is found to be a temperature-dependent value in accordance with equation (3.8). At 200° C, the temperature sensitivities of the fabricated sensors with angle of the slanted end fiber of 45°, 30°, and 22.5° were 10.3 pm/°C, 14.9 pm/°C, and 21.5 pm/°C, respectively. These experimental results showed the feasibility of fiber optics with slanted ends to sense in the range of temperature from 25°C to 220°C, getting sensitivities up to 21.5 pm/°C.

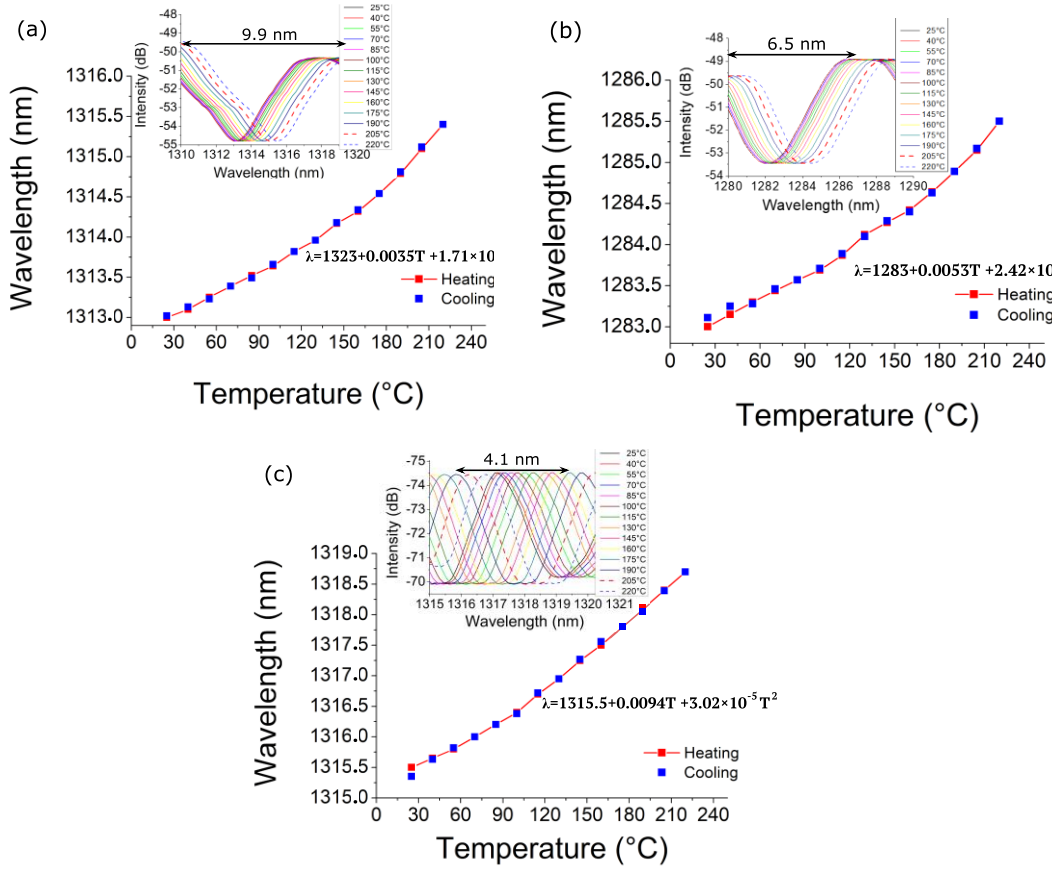

Figure 3-12: The temperature response, and the corresponding quadratic fit curve, of the sensors based on slanted fibers ends at (a) 45°, (b) 30°, and (c) 22.5°.

Refractive Index Sensor based on Optical Fibers with Slanted Ends

The sensor based on an optical fiber with a slated end was tested with NaCl solutions molar concentration of 0, 0.2, 0.4, 0.8, 1.0, 1.7, and 3.4 mol/L, whose corresponding RI were 1.3095, 1.3119, 1.3143, 1.3188, 1.3210, 1.3285, and 1.3439. These RI were determined using an Abbe refractometer (Shtopview FKR-710) with a resolution of 1×10^{-4} RIUs at a wavelength of 1310 nm. At every tested solution point, the reflection spectrum of the sensor was recorded after the optical signal has been steady for 10 min to lead to a more accurate measurement. All tests were carried out at room temperature, considering that, in accordance with the previously described results, to measure a notable spectrum response due to temperature fluctuation is needed to produce a variation of the order of 10 °C. The central interference peaks on each pattern were taken and the intensity fluctuation was analyzed to study the effect of RI change due to the NaCl solutions. The spectrum response of the sensor to these NaCl solutions is shown in power scale in Figure 3-13 and in logarithm scale in inset of the same figure. As expected, the intensity quickly decreased with the increase of NaCl concentration. In addition, the Figure 3-13 (b) shows with stars the average of the intensity variations of the measured normalized reflection spectrums of the sensors to the NaCl solutions, presenting high repeatability of the response, as can be inferred from the error bars, and a high consistence both increasing and decreasing NaCl concentration. Analytical (circles) and numerical (squares) results are also presented in the same plot.

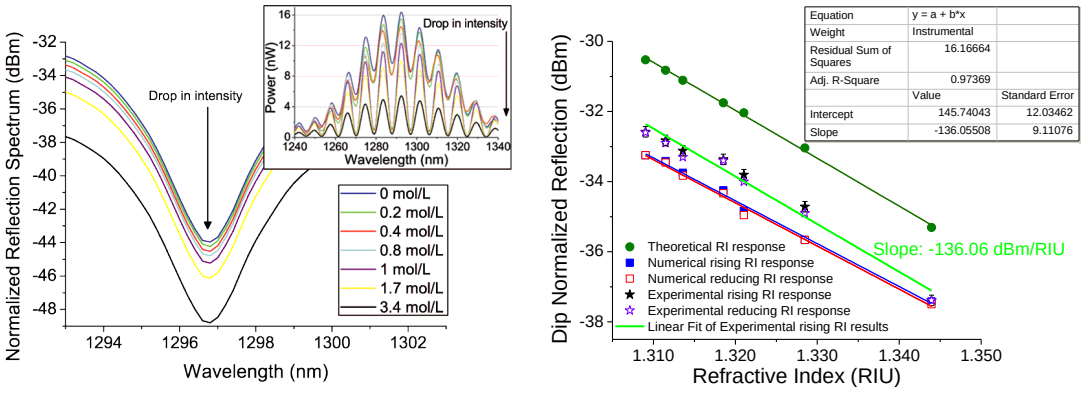

Figure 3-13: Experimental results of the intensity responses of the sensor based on fiber optics with slated end with the rising and reducing of RI. Insets: Intensity spectrum and normalized reflection spectrum.

As can be inferred from the slope of the experimental graph in Figure 3-13 (b), the sensibility of the fabricated fiber optics with slanted end is -136.03 dBm/RIU, in accordance with the theoretically (-140.2 dBm/RIU) and numerically (-128.7 dBm/RIU) forecasted behavior of this cost-effective RI sensor. The obtained results are summarized in the plot of Figure 3-13 (b). The concurrence between the analytical study, the numerical analysis, and the experimental results validated the feasibility of getting sensitivities up to -136 dBm/RIU, in the range of RI from 1.3095 to 1.3439, using very simple, sensitive, easy-to-fabricate, cost-effective, and compact sensor based on slanted fibers end. This practical sensing structure could be used to measure low concentrations of chemical species, which is precisely what will be treated in the next chapter. In addition, the research work carried out with the optical fiber with slanted end led to the publication of some contributions reported in the following manuscripts published in indexed journals of international circulation and presented at an international conference:

Brayan Patiño-Jurado, Luis Fernanda Álvarez Villa, Juan F. Botero-Cadavid, and Jorge Garcia-Sucerquia. "Temperature Sensor based on Optical Fibers with Slanted Ends." Optica pura y aplicada 55.1 (2022): 18.

Brayan Patiño-Jurado, Arturo Gaviria-Calderón, Juan F Botero-Cadavid, and Jorge Garcia-Sucerquia. "Intensity-Modulated Refractive Index Sensor Based on Optical Fiber with Slanted End " Optics & Laser Technology 157 (2023): 108700.

Brayan Patiño-Jurado, Juan F Botero-Cadavid, and Jorge Garcia-Sucerquia*. "Temperature sensor based on tilted optical fiber end with tailored sensitivity".* Latin America Optics and Photonics Conference. Optica Publishing Group, 2022.

Brayan Patiño-Jurado, Arturo Gaviria-Calderón, Juan F Botero-Cadavid, and Jorge Garcia-Sucerquia*. "Refractive Index Sensor Based on Optical Fiber with Slanted End".* Latin America Optics and Photonics Conference. Optica Publishing Group, 2022.

3.3 Etched SMS structures for measuring refractive index.

3.3.1 Introduction and Background

The measurements of refractive index (RI) are widely used in biochemical analysis, food safety inspection, environmental monitoring, and other technological fields [37]–[39]. As aforementioned, the traditional RI sensing technologies include, but are not limited to tapering [24], [42], [43], photonic crystals [16], [44], [45], surface plasmons [46]–[48], long-period grating [49]–[51], fiber Bragg grating [52]–[54], and interferometers [55]–[58]; such as Fabry–Perot [63], [64], Michelson [59], [65], and Mach–Zehnder [66], [67] sensors. These RI sensors have demonstrated high sensitivity 15000-35000 nm/RIU), selectivity, and wide measurement range [58]. However, these sensors usually have the disadvantage that require robust fabrication methods and precise and expensive equipment for wavelength measuring [59], [60], which complicates the implementation. Therefore, compact, cost-effective, and practical sensing technologies are demanded for the diverse environments in which the RI measurements take place. In response to the mentioned drawbacks, this section aims to contribute to the study of a very inexpensive (less than $5 USD for materials and manufacturing), compact, easier to fabricate RI sensor based on a SMS fiber structure.

Firstly, this last section of Chapter 3 presents a model that describes the formation of an optical spectrum as a result of the multimodal interference phenomenon and the wavelength-modulation due to RI fluctuation for the sensing probe based on a singlemode-multimode-singlemode (SMS) fiber structure. Along with the theoretical analysis, it is included a numerical verification of the proposed model using COMSOL Multiphysics®. Secondly, the structures were fabricated to experimentally demonstrate the feasibility to tailor the geometry and the sensitivity of this simple technology and, therefore, reliably measure RI in NaCl solutions; proving at the same time that the sensitivity of this cost-effective sensor can reach to 766 nm/RIU in the RI range from 1.3095 to 1.3439.

3.3.2 Operating Principle

The sensor based on singlemode-multimode-singlemode fiber optics (SMS) structure consists of input and output singlemode fibers (SMFs) spliced to the ends of a coreless multimode fiber (MMF) of a determined length, as shown in Figure 3-14. In order to reduce the fiber cladding, exposing the transmitted light to the external environment, a chemical etching with Hydrofluoric acid (HF) is used to controllably obtain an MMF section with a specific diameter. When the light field that propagates through the input SMF reaches the MMF section, the fundamental mode gets coupled to high-order eigenmodes that can propagate along this multimode segment producing an interference in the output single mode segment, called multimodal interference [82], that modulates the optical output leading to the several resonant dips in the transmitted spectra of the SMS fiber.

Assuming ideal alignment of the SMF segments and the MMF section, and circular symmetry of the input field, only LP_{0m} modes are excited in the MMF segment when light propagates from SMF to MMF section. The input light field at the MMF section has a fundamental mode field distribution $E(r,0)$, which can be decomposed into the eigenmodes LP_{0m} when the light goes through the MMF segment. Denotating the excited eigenmodes as $\phi_m(r)$, the input light field at the MMF can be expressed as [83]:

$$E(r,0) = \sum_{m=1}^{M} b_m \phi_m(r), \tag{3.12}$$

where M is the total number of excited modes, and $\boldsymbol{b_m}$ is excitation coefficient of the $\mathbf{LP0}_{\boldsymbol{m}}$ mode, which can be calculated as [83]

$$b_m = \frac{\int_0^\infty E(r,0)\phi_m(r)rdr}{\int_0^\infty \phi_m(r)\phi_m(r)rdr}. \tag{3.13}$$

Here $\phi_m(r)$ is determined by the fiber core diameters and the refractive index of the fiber core and cladding. With this, the field distribution at propagation distance z can be expressed as

$$E(r,z) = \sum_{m=1}^{M} b_m \phi_m(r) e^{i\beta_m z}, \tag{3.14}$$

where β_m is the propagation constant of each excited eigenmode in the MMF segment. In turn, the relation for two propagation constants β_m and β_n, for the m and n order modes, can be derived as:

$$\beta_m - \beta_n = \frac{\upsilon_m - \upsilon_n}{2k_0 r_c^2 n_c}, \tag{3.15}$$

with r_c and n_c are the radius and the refractive index of the MMF, respectively. In addition, υ_m and υ_n are the normalized transverse propagation constants, where $\upsilon_l = (2l - 1/2)\pi/2$. Here, if L is the length of the MMF segment, and N is a natural number, the constructive interference between these two modes occurs when the phase difference of the two is the integer multiple of 2π:

$$(\beta_m - \beta_n)L = 2\pi N. \tag{3.16}$$

And then the wavelength of the constructive interference can be calculated from equations (3.15) and (3.16) as follows

$$\lambda = \frac{8(2N+1)n_c r_c^2}{(m-n)[2(m+n)-1]L} \tag{3.17}$$

Whereof the wavelength difference of adjacent extreme is obtained as:

$$\Delta\lambda = \frac{16 n_c r_c^2}{(m-n)[2(m+n)-1]L} \tag{3.18}$$

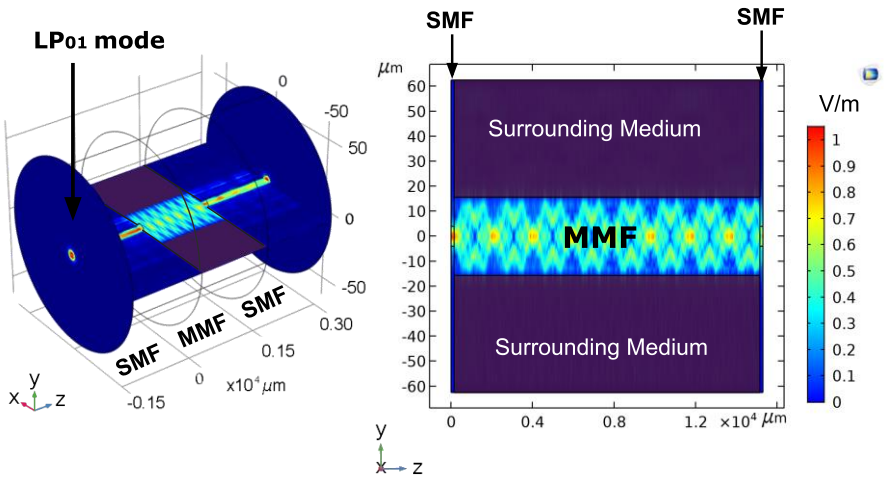

Figure 3-14: Fundamental mode LP_{01} exited in the flat end of the SMF segment and electric field distribution along the direction of light propagation within an SMS fiber structure.

From equation (3.18), it can be realized that the interference peaks, are less spaced when L becomes longer and r_c becomes smaller. Moreover, when the refractive index (RI) of the surrounding medium changes, the effective RI of the cladding of the fiber changes, the eigenmodes excited in the MMFC are alternated resulting in the changes for the propagation constants. Therefore, from equation (3.16), when the propagation constants change, the phase condition of the constructive (or destructive) interference is altered and N changes, producing the shift of the wavelength of the constructive (or destructive) interference, according to equation (3.17).

This behavior of the response of the spectrum to the RI of the surrounding medium changes can be verified from a numerical study by means of the finite element method (FEM). For this purpose, a numerical electromagnetic wave propagation study in COMSOL Multiphysics™ was realized to simulate the light transmission characteristics within the sensor based on the E-SMS structure [79]. Two standard singlemode step-index optical fibers segments (Corning SMF-28e, refractive index 1.464 for the core and 1.458 for the cladding) and one coreless optical fiber (Thorlabs FG125LA, refractive index 1.444) surrounded by air for the MMF segment, were discretized using the standard meshing tool with the mesh setting at Physics-controlled mesh and the element size set to Extremely fine. The electromagnetic wave propagation was performed by exciting a TE wave at the flat end of the input (left) SMF segment. The propagation modes found by the COMSOL solver were those which fulfilled the Maxwell equations with an effective modal index, n_{eff}, between the refractive indexes of the cladding and the core $n_{core} < n_{eff} < n_{cladding}$. In the performed analysis, the effective modal index obtained for input SMF segment corresponded to that one of the fundamental modes. The simulated amplitude distribution of the propagating light within an SMS fiber structure is shown in Figure 3-14. The LP_{01} mode profile at a z position of 200 μm is shown in the same figure, where z is the propagation direction of the field.

In order to study the dependence of the optical interference spectrum with the geometry and the refractive index of the surrounding medium, around the MMF section, the simulation was performed slightly modifying these parameters on a wide

range of values. However, in order to illustrate the numerical spectrum response, only some separated points are plotted. It can be seen from Figure 3-15 (a), the simulated spectrum is influenced by the core diameter of MMF (d) verifying that the dips and peaks blue-shift when the core diameter becomes smaller. Moreover, when the surrounding RI (n) changes from 1.3 to 1.5, the transmission spectrum red-shifts, as shown in Figure 3-15 (b).

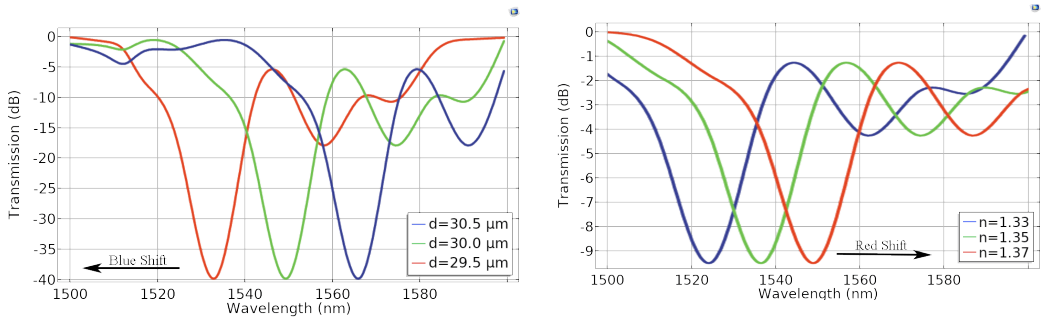

Figure 3-15: Simulation of the transmission spectrum of the E-SMS structure with different (a) core diameter of MMF and (b) surrounding refractive indexes.

3.3.3 Materials and Methods

Fabrication and Experimental Setup

Coreless MMF segments ((Thorlabs FG125LA, refractive index 1.444)), standard SMF pigtails (Corning SMF-28e, refractive index 1.464 for the core and 1.458 for the cladding), and Hydrofluoric acid 40% (Sigma-Aldrich) were used for fabrication of the E-SMS structures. SMF pigtails were splicing on each end of 15-mm segments of MMF using a conventional fusion splicer (FITEL S178A V2) in automatic mode. The choice of MMF length was defined by the volume of sample to study, considering that that longitude only affects the spacing between peaks and dips, as described above The SMS structures were placed in a plastic container with small lateral slits to hold them in place and the cavity of the container was filled with aqueous solution HF at a 40% concentration until the diameter of the structures were approximately 30 µm.

In order to make the fabrication highly reproducible and allowing the production of mechanically solid etching SMS (E-SMS) sensors, the method was optimized by the continuous monitoring of the wavelength response during the chemical etching. Light from a broadband source (Thorlabs S5FC1550S-A2) was used as light source, and an optical spectrum analyzer (OSA, Yokogawa AQ6370) with a wavelength resolution

of 10 pm was used to measure transmission spectra of the E-SMS sensor, as shown in Figure 3-16 (a). This etching stage took 45 min at a rate of about 2 μm/min for the MMF at room temperature.

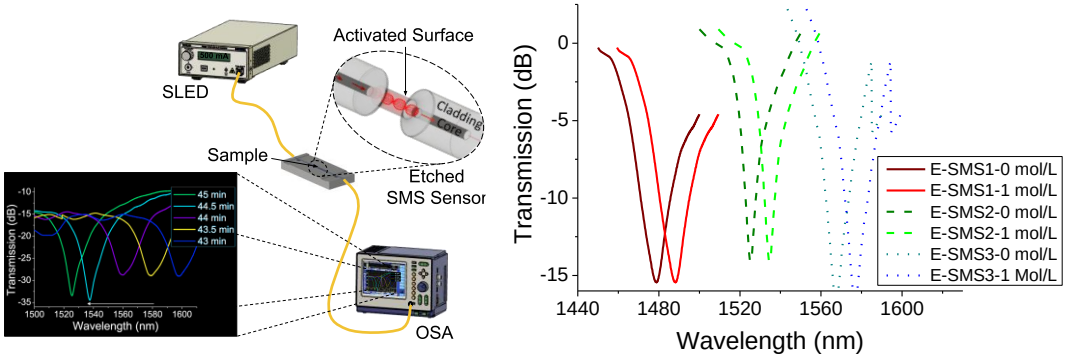

(a) (b)

Figure 3-16: Experimental setup used to measure transmission spectra of the E-SMS sensor. (b) Spectral response to aqueous NaCl solutions for three E-SMS sensors. The interference peak can be tuned.

The continuous monitoring of the wavelength response during the chemical etching allows to tailor the geometry and the sensitivity of the sensor based on E-SMS structure and also to tune the wavelength at which the interference peak is centered, as shown in the response spectrums to sodium chloride (NaCl) for three different sensors (SMS1 solid red line, SMS2 green dashes, and SMS3 blue dots) in Figure 3-16 (b). As can be observed, it was possible to tune the spectrum between 1400 and 1600 nm by arresting the chemical etching when the peak being tracked is at the desired wavelength. Centering the interference dip in 1530 nm, the sensitivity of the E-SMS structure was evaluated performing a complete characterization in aqueous solutions of NaCl.

3.3.4 Results and discussion

The E-SMS sensor was submerged in each calibrated sample of NaCl solutions molar with concentration of 0, 0.2, 0.4, 0.8, 1.0, 1.7, and 3.4 mol/L, whose corresponding RI are 1.3089, 1.3117, 1.3139, 1.3193, 1.3208, 1.3295, and 1.344. These RI were determined using an Abbe refractometer (Shtopview FKR-710) with a resolution of 1 $\times 10^{-4}$ RIUs at a wavelength of 1500 nm. The spectrum response of

the sensor to these NaCl solutions is shown in inset of Figure 3-17 (a). In the same figure, the wavelength shift of the tuned dip is plotted versus the refractive index, tracing the lineal correlation. The slope of the straight-line response is 766.13 nm/RIU, which corresponds to the sensitivity of the sensors to measurements of NaCl concentration. The Figure 3-17 (b) resumes the sensitivity to NaCl measurements for seven E-SMS sensors fabricated using the same methodology described above. As can be observed, this fabrication method allows to obtain reproducible and repeatable E-SMS sensors with tailored spectral response and sensitivity in the same order of magnitude. Those characteristics are very suitable in order to obtain reliable sensors to detecting chemical and biological substances at low concentrations; however, an additional process of activation is required in order to produce a selective detection of the molecule of interest. The activation/immobilization protocols of the sensor based on slanted fibers end and the sensor based on a E-SMS structure are addressed in the following chapters.

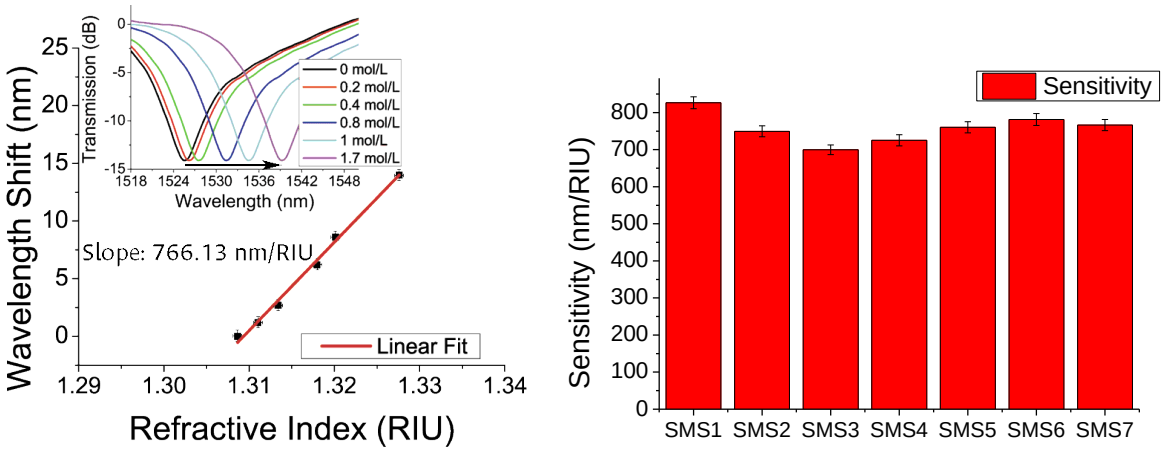

(a) (b)

Figure 3-17: (a) Response of the E-SMS sensor to the NaCl solutions. Inset: the wavelength shift of the tuned dip. (b) sensibility to NaCl measurements for seven E-SMS sensors fabricated under the same conditions.

3.4 Performance comparison of analytical parameters of proposed sensor with existing sensors

Table 3-1: Comparation of analytical parameters of the fabricated sensor with other fiber optics technologies proposed for measuring RI and temperature.

Physical property	Sensing technique	Sensitivity	Measuring range	Simplicity of fabrication and application	Cost-effective ratio (cost/ sensitivity)	References
Refractive index	E-SMS	766 nm/RIU	1.309-1.343	Simple	1 (reference)	-
	Slanted Ends	-136 dBm/RIU	1.309-1.343	Very simple	10	-
	Tapering	1500 nm/RIU 998 dBm/RIU	1.332-1.334 1.331-1.338	Mildly complex	2 10	[23], [24]
	Photonic crystals	3000 nm/RIU -347 dBm/RIU	1.333- 1.422 1.333-1.349	Complex	10 13	[86]–[88]
	Surface plasmons	25000 nm/RIU -333.4 dBm/RIU	1.333-1.371 1.306-1.340	Complex	1.5 15	[46]–[48]
	Long-period grating	20000 nm/RIU -165 dBm/RIU	1.327-1.401 1.333-1.435	Complex	2 10	[49]–[51]
	Fiber Bragg grating	885 nm/RIU -234 dBm/RIU	1.348–1.378 1.333–1.377	Complex	10 10	[52]–[54]
	D-shaped	1350 nm/RIU -327 dBm/RIU	1.352-1.414 1.333-1.370	Simple	2.5 12	[61], [62]
	Fabry–Perot	1225 nm/RIU 108.07 dBm/RIU	1332-1339 1.450-1.531	Mildly complex	6 12	[63], [64]
	Michelson	165.77 nm/RIU 204.25 dBm/RIU	1.334-1.371 1.331-1342	Simple	12 13	[59], [65]
	Mach–Zehnder	1520 nm/RIU 252.69 dBm/RIU	1.315-1.341 1.333-1.345	Mildly complex	5 15	[66], [67]
Temperature	E-SMS	9.2 pm/°C	25 - 65 °C	Simple	2	[89]
	Slanted Ends	21.5 pm/°C	25 –225 °C	Very simple	1 (reference)	-
	Tapering	20 pm/°C	50-150 °C	Mildly complex	5	[50], [90]
	Photonic crystals	284 pm/°C	20-90 °C	Complex	3	[35], [91]
	Surface plasmons	720 pm/°C	25-100 °C	Complex	1	[92]
	Long-period grating	84.5 pm/°C	20-80 °C	Complex	10	[93], [94]
	Fiber Bragg grating	34.3 pm/°C	20-60 °C	Complex	15	[70], [95]
	D-shaped	28.7 pm/°C	21-50 °C	Simple	4	[62]
	Fabry–Perot	13.7 pm/°C	25-150 °C	Mildly complex	11	[45], [56]
	Michelson	13.32 pm/°C	19-290 °C	Simple	8	[73], [96]
	Mach–Zehnder	11.7 pm/°C	22-100 °C	Mildly complex	12	[97]–[99]

To emphasize the feasibility of the fabricated sensors, the sensor based on optical fiber with slanted end and the E-SMS sensor, a performance comparison of analytical parameters has been performed with the most representative RI and temperature sensors based on optical fibers that can be found in the literature. As a preliminary step to organize the data, an overview of estimated costs of materials and manufacturing of those sensors was developed from the comparative cost analysis that can be found in different reviews, such as that reported in [99]–[103]. The Table 3-1 organizes the comparative parameters of the sensors taking as degree of

complexity of manufacturing and implementation the robustness of the equipment, materials, methodologies, and trained personnel used in those techniques. As can be observed, the sensitivity to the RI and temperature changes of the proposed sensors is in the middle range in comparation to the widely reported sensors. Furthermore, the main advantages of the proposed sensors are their cost effectiveness, estimated from the cost/sensitivity ratio, simplicity of construction, and relative ease of implementation.

3.5 References for Chapter 3

[1] E. Udd and W. B. Spillman, *Fiber Optic Sensors: An Introduction for Engineers and Scientists: Second Edition*. 2011.

[2] G. Kostovski, P. R. Stoddart, and A. Mitchell, “The optical fiber tip: An inherently light-coupled microscopic platform for micro- and nanotechnologies,” *Advanced Materials*. 2014, doi: 10.1002/adma.201304605.

[3] E. Betzig, A. Lewis, A. Harootunian, M. Isaacson, and E. Kratschmer, “Near Field Scanning Optical Microscopy (NSOM): Development and Biophysical Applications,” *Biophys. J.*, 1986, doi: 10.1016/S0006-3495(86)83640-2.

[4] M. Garcia-Parajo, E. Cambril, and Y. Chen, “Simultaneous scanning tunneling microscope and collection mode scanning near-field optical microscope using gold coated optical fiber probes,” *Appl. Phys. Lett.*, 1994, doi: 10.1063/1.112024.

[5] B. I. Yakobson, A. LaRosa, H. D. Hallen, and M. A. Paesler, “Thermal/optical effects in NSOM probes,” *Ultramicroscopy*, 1995, doi: 10.1016/0304-3991(95)00121-2.

[6] P. Hoffmann, B. Dutoit, and R. P. Salathé, “Comparison of mechanically drawn and protection layer chemically etched optical fiber tips,” *Ultramicroscopy*, vol. 61, no. 1–4, pp. 165–170, 1995, doi: 10.1016/0304-3991(95)00122-0.

[7] G. A. Valaskovic, M. Holton, and G. H. Morrison, “Parameter control, characterization, and optimization in the fabrication of optical fiber near-field probes,” *Appl. Opt.*, 1995, doi: 10.1364/AO.34.001215.

[8] Z. L. Ran, Y. J. Rao, W. J. Liu, X. Liao, and K. S. Chiang, “Laser-micromachined Fabry-Perot optical fiber tip sensor for high-resolution temperature-independent measurement of refractive index,” *Opt. Express*, 2008, doi: 10.1364/OE.16.002252.

[9] R. S. Taylor, C. Hnatovsky, E. Simova, D. M. Rayner, V. R. Bhardwaj, and P.

B. Corkum, “Femtosecond laser fabrication of nanostructures in silica glass,” *Opt. Lett.*, 2003, doi: 10.1016/j.ijmedinf.2006.12.004.

[10] Y. Ju, H. Sato, and H. Soyama, “Fabrication of the tip of GaAs microwave probe by wet etching,” in *ASME 2005 Pacific Rim Technical Conference and Exhibition on Integration and Packaging of MEMS, NEMS, and Electronic Systems collocated with the ASME 2005 Heat Transfer Summer Conference*, 2005, pp. 1919–1922.

[11] H. Nikbakht, H. Latifi, M. Oraie, and T. Amini, “Fabrication of tapered tip fibers with a controllable cone angle using dynamical etching,” *J. Light. Technol.*, vol. 33, no. 23, pp. 4707–4711, 2015, doi: 10.1109/JLT.2015.2453365.

[12] P. Lambelet, A. Sayah, M. Pfeffer, C. Philipona, and F. Marquis-Weible, “Chemically etched fiber tips for near-field optical microscopy: a process for smoother tips,” *Appl. Opt.*, vol. 37, no. 31, p. 7289, 1998, doi: 10.1364/AO.37.007289.

[13] A. Barucci *et al.*, “Optical fibre nanotips fabricated by a dynamic chemical etching for sensing applications,” *J. Appl. Phys.*, 2015, doi: 10.1063/1.4906854.

[14] P. Burgos *et al.*, “Near-field scanning optical microscopy probes: A comparison of pulled and double-etched bent NSOM probes for fluorescence imaging of biological samples,” *J. Microsc.*, 2003, doi: 10.1046/j.1365-2818.2003.01197.x.

[15] Y. K. Cheong, K. S. Lim, W. H. Lim, W. Y. Chong, R. Zakaria, and H. Ahmad, “Note: Fabrication of tapered fibre tip using mechanical polishing method,” *Rev. Sci. Instrum.*, vol. 82, no. 8, pp. 26–29, 2011, doi: 10.1063/1.3627374.

[16] J. P. Clarkin, R. J. Timmerman, and J. H. Shannon, “Shaped fiber tips for medical and industrial applications,” in *Optical fibers and sensors for medical applications IV*, 2004, vol. 5317, pp. 70–81.

[17] R. M. Verdaasdonk and C. Borst, “{R}ay tracing of optically modified fiber tips. 2: laser scalpels,” *Appl. Opt.*, 1991, doi: 10.1364/AO.30.002172.

[18] R. M. Verdaasdonk and C. Borst, “Ray tracing of optically modified fiber tips. 1: spherical probes,” *Appl. Opt.*, vol. 30, no. 16, pp. 2159–2171, 1991.

[19] L. Lilge, L. Vesselov, and W. Whittington, “Thin cylindrical diffusers in multimode Ge-doped silica fibers,” *Lasers Surg. Med.*, 2005, doi: 10.1002/lsm.20150.

[20] A. Klini *et al.*, “Reproducible optical fiber tips for photon scanning tunneling microscopy with very small (<5°) cone angle,” *J. Light. Technol.*, vol. 16, no. 7, pp. 1220–1227, 1998, doi: 10.1109/50.701400.

[21] S. I. Hosain, Y. Lacroute, and J. P. Goudonnet, “A simple low-cost highly reproducible method of fabricating optical fiber tips for a photon scanning

tunneling microscope," *Microw. Opt. Technol. Lett.*, 1996, doi: 10.1002/(SICI)1098-2760(19961205)13:5<243::AID-MOP1>3.0.CO;2-G.

[22] P. Wang, L. Bo, Y. Semenova, Q. Wu, G. Farrell, and G. Brambilla, "A multimode fiber tip based temperature sensor," *Adv. Photonics 2013 (2013), Pap. SM2D.4*, p. SM2D.4, Jul. 2013, doi: 10.1364/SENSORS.2013.SM2D.4.

[23] P.-K. Wei and Y.-H. Tai, "Sensitive liquid refractive index sensors using tapered optical fiber tips," *Opt. Lett. Vol. 35, Issue 7, pp. 944-946*, vol. 35, no. 7, pp. 944–946, Apr. 2010, doi: 10.1364/OL.35.000944.

[24] V. Bhardwaj and V. K. Singh, "Optical fiber cone taper tip sensor for refractive index measurement," *Indian J. Pure Appl. Phys.*, vol. 55, no. 5, pp. 345–348, 2017, Accessed: Jul. 12, 2021. [Online]. Available: http://14.139.47.23/index.php/IJPAP/article/view/10721.

[25] B. Patiño-Jurado, J. F. Botero-Cadavid, and J. Garcia-Sucerquia, "Analytical study of the numerical aperture of cone-shaped optical fibers: A tool for tailored designs," *Heliyon*, vol. 5, no. 5, 2019, doi: 10.1016/j.heliyon.2019.e01612.

[26] D. R. Turner, "Etch procedure for optical fibers," 4469554, 1984.

[27] M. Tao, Y. Jin, N. Gu, and L. Huang, "A method to control the fabrication of etched optical fiber probes with nanometric tips," *J. Opt. A Pure Appl. Opt.*, vol. 12, no. 1, 2010, doi: 10.1088/2040-8978/12/1/015503.

[28] X. Li, L. Liu, J. Zhao, and J. Tan, "Optical Properties of Sodium Chloride Solution Within the Spectral Range from 300 to 2500 nm at Room Temperature.," *Appl. Spectrosc.*, vol. 69, no. 5, pp. 635–40, May 2015, doi: 10.1366/14-07769R.

[29] L. Mandel, E. Wolf, and P. Meystre, "Optical Coherence and Quantum Optics," *Am. J. Phys.*, 1996, doi: 10.1119/1.18450.

[30] A. Ukil, H. Braendle, and P. Krippner, "Distributed temperature sensing: Review of technology and applications," *IEEE Sensors Journal*, vol. 12, no. 5. pp. 885–892, 2012, doi: 10.1109/JSEN.2011.2162060.

[31] P. R. N. Childs, J. R. Greenwood, and C. A. Long, "Review of temperature measurement," *Rev. Sci. Instrum.*, vol. 71, no. 8, p. 2959, Jul. 2000, doi: 10.1063/1.1305516.

[32] A. Ghosh, C. Zhang, S. Q. Shi, and H. Zhang, "High-Temperature Gas Sensors for Harsh Environment Applications: A Review," *CLEAN – Soil, Air, Water*, vol. 47, no. 8, p. 1800491, Aug. 2019, doi: 10.1002/CLEN.201800491.

[33] M. R. Werner and W. R. Fahrner, "Review on materials, microsensors, systems, and devices for high-temperature and harsh-environment applications," *IEEE Trans. Ind. Electron.*, vol. 48, no. 2, pp. 249–257, Apr. 2001, doi: 10.1109/41.915402.

[34] M. Mansoor, I. Haneef, S. Akhtar, A. De Luca, and F. Udrea, "Silicon diode

temperature sensors—A review of applications," *Sensors Actuators A Phys.*, vol. 232, pp. 63–74, Aug. 2015, doi: 10.1016/J.SNA.2015.04.022.

[35] H. Y. Choi, M. J. Kim, and B. H. Lee, "All-fiber Mach-Zehnder type interferometers formed in photonic crystal fiber," *Opt. Express*, vol. 15, no. 9, p. 5711, Apr. 2007, doi: 10.1364/OE.15.005711.

[36] J. Chen, Y. Zhu, Z. Guo, and A. G. Nasibulin, "Recent progress on thermo-electrical properties of conductive polymer composites and their application in temperature sensors," *Eng. Sci.*, vol. 12, pp. 13–22, 2020, doi: 10.30919/ES8D1129.

[37] J. J. Patil, Y. H. Patil, and A. Ghosh, "Comprehensive and Analytical Review on Optical Fiber Refractive Index Sensor," *Proc. 4th Int. Conf. Trends Electron. Informatics, ICOEI 2020*, pp. 169–175, Jun. 2020, doi: 10.1109/ICOEI48184.2020.9142916.

[38] T. Takeo and H. Hattori, "Optical Fiber Sensor for Measuring Refractive Index," *Jpn. J. Appl. Phys.*, vol. 21, no. 10, pp. 1509–1512, Oct. 1982, doi: 10.1143/JJAP.21.1509/XML.

[39] P. Nath, H. K. Singh, P. Datta, and K. C. Sarma, "All-fiber optic sensor for measurement of liquid refractive index," *Sensors Actuators A Phys.*, vol. 148, no. 1, pp. 16–18, Nov. 2008, doi: 10.1016/J.SNA.2008.06.027.

[40] J. Li, "A review: Development of novel fiber-optic platforms for bulk and surface refractive index sensing applications," *Sensors and Actuators Reports*, vol. 2, no. 1, p. 100018, Nov. 2020, doi: 10.1016/J.SNR.2020.100018.

[41] N. Sabri, S. A. Aljunid, M. S. Salim, R. B. Ahmad, and R. Kamaruddin, "Toward Optical Sensors: Review and Applications," *J. Phys. Conf. Ser.*, vol. 423, no. 1, p. 012064, Apr. 2013, doi: 10.1088/1742-6596/423/1/012064.

[42] S. Mononobe and M. Ohtsu, "Fabrication of a pencil-shaped fiber probe for near-field optics by selective chemical etching," *J. Light. Technol.*, 1996, doi: 10.1109/50.541212.

[43] M. A. Mahdi, M. H. A. Bakar, R. Narayanaswamy, T. K. Yadav, and Y. M. Kamil, "Single mode tapered fiber-optic interferometer based refractive index sensor and its application to protein sensing," *Opt. Express, Vol. 22, Issue 19, pp. 22802-22807*, vol. 22, no. 19, pp. 22802–22807, Sep. 2014, doi: 10.1364/OE.22.022802.

[44] J. E. Betancur-Ochoa, V. P. Minkovich, and Y. J. Montagut-Ferizzola, "Special Photonic Crystal Modal Interferometer for Highly Sensitive Biosensing," *J. Light. Technol. Vol. 35, Issue 21, pp. 4747-4751*, vol. 35, no. 21, pp. 4747–4751, Nov. 2017, Accessed: Jul. 19, 2021. [Online]. Available: https://www.osapublishing.org/abstract.cfm?uri=jlt-35-21-4747.

[45] B. H. Lee, E. S. Choi, H. Y. Choi, K. S. Park, S. J. Park, and U.-C. Paek,

"Miniature fiber-optic high temperature sensor based on a hybrid structured Fabry–Perot interferometer," *Opt. Lett. Vol. 33, Issue 21, pp. 2455-2457*, vol. 33, no. 21, pp. 2455–2457, Nov. 2008, doi: 10.1364/OL.33.002455.

[46] P.-K. Wei and Y.-H. Tai, "Sensitive liquid refractive index sensors using tapered optical fiber tips," *Opt. Lett. Vol. 35, Issue 7, pp. 944-946*, vol. 35, no. 7, pp. 944–946, Apr. 2010, doi: 10.1364/OL.35.000944.

[47] J. N. Dash and R. Jha, "Highly sensitive D shaped PCF sensor based on SPR for near IR," *Opt. Quantum Electron.*, vol. 48, no. 2, pp. 1–7, Feb. 2016, doi: 10.1007/s11082-016-0423-3.

[48] J. Homola and M. Piliarik, "Surface Plasmon Resonance (SPR) Sensors," Springer, Berlin, Heidelberg, 2006, pp. 45–67.

[49] P. Pilla *et al.*, "Long Period Grating coated with high refractive index layer," in *Proceedings of WFOPC2005 - 4th IEEE/LEOS Workshop on Fibres and Optical Passive Components*, 2005, vol. 2005, pp. 370–375, doi: 10.1109/WFOPC.2005.1462157.

[50] D. J. Webb *et al.*, "Spectral Characteristics of Tapered LPG Device as a Sensing Element for Refractive Index and Temperature," *J. Light. Technol. Vol. 24, Issue 2, pp. 870-*, vol. 24, no. 2, pp. 870-, Feb. 2006, Accessed: May 02, 2021. [Online]. Available: https://www.osapublishing.org/abstract.cfm?uri=jlt-24-2-870.

[51] D. Chu, J. Duan, K. Yin, X. Dong, Y. Song, and Z. Xie, "High temperature-sensitivity sensor based on long period fiber grating inscribed with femtosecond laser transversal-scanning method," *Chinese Opt. Lett. Vol. 15, Issue 9, pp. 090602-*, vol. 15, no. 9, pp. 090602-, Sep. 2017, Accessed: Jul. 26, 2021. [Online]. Available: https://www.osapublishing.org/abstract.cfm?uri=col-15-9-090602.

[52] M. A. Riza, Y. I. Go, S. W. Harun, and R. R. J. Maier, "FBG Sensors for Environmental and Biochemical Applications - A Review," *IEEE Sens. J.*, vol. 20, no. 14, pp. 7614–7627, Jul. 2020, doi: 10.1109/JSEN.2020.2982446.

[53] A. Méndez, "Fiber Bragg grating sensors: a market overview," in *Third European Workshop on Optical Fibre Sensors*, Jul. 2007, vol. 6619, p. 661905, doi: 10.1117/12.738334.

[54] X. Sang, C. Yu, T. Mayteevarunyoo, K. Wang, Q. Zhang, and P. L. Chu, "Temperature-insensitive chemical sensor based on a fiber Bragg grating," *Sensors Actuators, B Chem.*, vol. 120, no. 2, pp. 754–757, Jan. 2007, doi: 10.1016/j.snb.2006.03.046.

[55] Q. Wu *et al.*, "Singlemode-Multimode-Singlemode Fiber Structures for Sensing Applications-A Review," *IEEE Sens. J.*, vol. 21, no. 11, pp. 12734–12751, Jun. 2021, doi: 10.1109/JSEN.2020.3039912.

[56] Z. Huang, Y. Zhu, X. Chen, and A. Wang, "Intrinsic Fabry-Pérot fiber sensor for temperature and strain measurements," *IEEE Photonics Technol. Lett.*,

vol. 17, no. 11, pp. 2403–2405, Nov. 2005, doi: 10.1109/LPT.2005.857236.

[57] K. Tian *et al.*, “High sensitivity temperature sensor based on singlemode-no-core-singlemode fibre structure and alcohol,” *Sensors Actuators A Phys.*, vol. 284, pp. 28–34, Dec. 2018, doi: 10.1016/J.SNA.2018.10.016.

[58] P. Lu, L. Men, K. Sooley, and Q. Chen, “Tapered fiber Mach–Zehnder interferometer for simultaneous measurement of refractive index and temperature,” *Appl. Phys. Lett.*, vol. 94, no. 13, p. 131110, Apr. 2009, doi: 10.1063/1.3115029.

[59] J. Zhou *et al.*, “Intensity modulated refractive index sensor based on optical fiber Michelson interferometer,” *Sensors Actuators B Chem.*, vol. 208, pp. 315–319, Mar. 2015, doi: 10.1016/J.SNB.2014.11.014.

[60] C. Zhang, S. Xu, J. Zhao, H. Li, H. Bai, and C. Miao, “Intensity-modulated refractive index sensor with anti-light source fluctuation based on no-core fiber filter,” *Opt. Laser Technol.*, vol. 97, pp. 358–363, Dec. 2017, doi: 10.1016/J.OPTLASTEC.2017.07.023.

[61] T. H. C. De Barros, J. E. S. Sousa, H. P. Alves, and J. F. Martins-Filho, “D-Shaped Plastic Optical Fibers: Fabrication and Characterization as Refractive Index Sensor,” *2021 SBMO/IEEE MTT-S Int. Microw. Optoelectron. Conf. IMOC 2021*, 2021, doi: 10.1109/IMOC53012.2021.9624875.

[62] J. Mohanraj, V. Velmurugan, S. Sathiyan, and S. Sivabalan, “All fiber-optic ultra-sensitive temperature sensor using few-layer MoS2 coated D-shaped fiber,” *Opt. Commun.*, vol. 406, pp. 139–144, Jan. 2018, doi: 10.1016/J.OPTCOM.2017.06.011.

[63] N. Gaber *et al.*, “Volume refractometry of liquids using stable optofluidic Fabry-Pérot resonator with curved surfaces,” *https://doi.org/10.1117/12.2076034*, vol. 9375, pp. 192–200, Feb. 2015, doi: 10.1117/12.2076034.

[64] R. M. André *et al.*, “Simultaneous measurement of temperature and refractive index using focused ion beam milled Fabry-Perot cavities in optical fiber micro-tips,” *Opt. Express, Vol. 24, Issue 13, pp. 14053-14065*, vol. 24, no. 13, pp. 14053–14065, Jun. 2016, doi: 10.1364/OE.24.014053.

[65] D. Wu, T. Zhu, and M. Liu, “A high temperature sensor based on a peanut-shape structure Michelson interferometer,” *Opt. Commun.*, vol. 285, no. 24, pp. 5085–5088, Nov. 2012, doi: 10.1016/J.OPTCOM.2012.06.091.

[66] C. H. Chen, W. Te Wu, and J. N. Wang, “All-fiber microfluidic multimode Mach–Zehnder interferometers as high sensitivity refractive index sensors,” *Microsyst. Technol. 2016 232*, vol. 23, no. 2, pp. 429–440, Apr. 2016, doi: 10.1007/S00542-016-2928-X.

[67] E. I. Pacheco-Chacon *et al.*, “An aluminum-coated asymmetric core-offset

Mach-Zehnder interferometer temperature sensor," *Opt. Fiber Technol.*, vol. 65, p. 102591, Sep. 2021, doi: 10.1016/J.YOFTE.2021.102591.

[68] A. K. Pathak, V. Bhardwaj, R. K. Gangwar, and V. K. Singh, "SPR based fiber sensor to measure refractive index of glycerol and acetone," *Proc. 2015 Int. Conf. Microw. Photonics, ICMAP 2015*, Feb. 2016, doi: 10.1109/ICMAP.2015.7408711.

[69] W. Luo *et al.*, "Temperature effects on surface plasmon resonance sensor based on side-polished D-shaped photonic crystal fiber," *Measurement*, vol. 181, p. 109504, Aug. 2021, doi: 10.1016/J.MEASUREMENT.2021.109504.

[70] T. Guo, T. Zhang, and X. Qiao, "FBG-EFPI sensor for large strain measurement with low temperature crosstalk," *Opt. Commun.*, vol. 473, p. 125945, Oct. 2020, doi: 10.1016/J.OPTCOM.2020.125945.

[71] R. Fiorin, V. De Oliveira, H. J. Kalinowski, R. C. Kamikawachi, and I. Abe, "FBG-Assisted Micro-Channel for Refractive Index Measurements," *IEEE Photonics Technol. Lett.*, vol. 33, no. 1, pp. 35–38, Jan. 2021, doi: 10.1109/LPT.2020.3043088.

[72] B. O. Guan, H. Y. Tam, X. M. Tao, and X. Y. Dong, "Simultaneous strain and temperature measurement using a superstructure fiber Bragg grating," *IEEE Photonics Technol. Lett.*, vol. 12, no. 6, pp. 675–677, Jun. 2000, doi: 10.1109/68.849081.

[73] N. Zhao *et al.*, "High temperature probe sensor with high sensitivity based on Michelson interferometer," *Opt. Commun.*, vol. 343, pp. 131–134, May 2015, doi: 10.1016/J.OPTCOM.2014.12.012.

[74] Z. Tian, S. S.-H. Yam, and H.-P. Loock, "Refractive index sensor based on an abrupt taper Michelson interferometer in a single-mode fiber," *Opt. Lett.*, vol. 33, no. 10, p. 1105, May 2008, doi: 10.1364/ol.33.001105.

[75] K. J. Gåsvik, "Optical metrology," p. 360, 2002.

[76] E. Hecht, *Optics*, 2nd ed. Reading, MA: Addison-Wesley.

[77] H. Gao, Y. Jiang, Y. Cui, L. Zhang, J. Jia, and L. Jiang, "Investigation on the thermo-optic coefficient of silica fiber within a wide temperature range," *J. Light. Technol.*, vol. 36, no. 24, pp. 5881–5886, Dec. 2018, doi: 10.1109/JLT.2018.2875941.

[78] A. Efimov, "Spatial coherence at the output of multimode optical fibers," *Opt. Express, Vol. 22, Issue 13, pp. 15577-15588*, vol. 22, no. 13, pp. 15577–15588, Jun. 2014, doi: 10.1364/OE.22.015577.

[79] COMSOL Multiphysics, "Introduction to COMSOL Multiphysics 5.0," *Manual*, 2009, doi: 10.1108/JCRE-12-2012-0031.

[80] M. Born *et al.*, "Principles of Optics: Electromagnetic Theory of Propagation, Interference and Diffraction of Light," *Princ. Opt.*, Oct. 1999, doi: 10.1017/CBO9781139644181.

[81] ImageJ, “ImageJ User Guide,” *Nat. Methods*, 2012, doi: 10.1038/nmeth.2019.

[82] “S5FC Series Single Channel Fiber-Coupled SLD Sources Operating Manual.”

[83] R. Stöckle *et al.*, “High-quality near-field optical probes by tube etching,” *Appl. Phys. Lett.*, vol. 75, no. 2, pp. 160–162, 1999, doi: 10.1063/1.124305.

[84] Y. C. Maya, I. Del Villar, A. B. Socorro, J. M. Corres, and J. F. Botero-Cadavid, “Optical Fiber Immunosensors Optimized with Cladding Etching and ITO Nanodeposition,” *31st Annu. Conf. IEEE Photonics Soc. IPC 2018*, Nov. 2018, doi: 10.1109/IPCON.2018.8527306.

[85] S. F. S. M. Noor, S. W. Harun, H. Ahmad, and A. R. Muhammad, “Multimode interference based fiber-optic sensor for temperature measurement,” *J. Phys. Conf. Ser.*, vol. 1151, no. 1, p. 012023, Jan. 2019, doi: 10.1088/1742-6596/1151/1/012023.

[86] H. Nikbakht, H. Latifi, T. Amini, and M. I. Zibaii, “Tip sensor probe for changing refractive index measurement in small volumes,” *Int. J. Opt. Photonics*, vol. 8, no. 2, pp. 105–111, 2014, Accessed: Jul. 12, 2021. [Online]. Available: http://ijop.ir/article-1-172-en.html.

[87] Y. E. Marin *et al.*, “Silicon-photonic interferometric biosensor using active phase demodulation,” *https://doi.org/10.1117/12.2287803*, vol. 10510, pp. 20–28, Feb. 2018, doi: 10.1117/12.2287803.

[88] J. E. Betancur-Ochoa, V. P. Minkovich, and Y. J. Montagut-Ferizzola, “Special Photonic Crystal Modal Interferometer for Highly Sensitive Biosensing,” *J. Light. Technol.*, vol. 35, no. 21, pp. 4747–4751, Nov. 2017, doi: 10.1109/JLT.2017.2761738.

[89] Y. Zhang, X. Tian, L. Xue, Q. Zhang, L. Yang, and B. Zhu, “Super-high sensitivity of fiber temperature sensor based on leaky-mode bent SMS structure,” *IEEE Photonics Technol. Lett.*, vol. 25, no. 6, pp. 560–563, 2013, doi: 10.1109/LPT.2013.2245644.

[90] A. D. Gomes and O. Frazao, “Microfiber Knot with Taper Interferometer for Temperature and Refractive Index Discrimination,” *IEEE Photonics Technol. Lett.*, vol. 29, no. 18, pp. 1517–1520, Sep. 2017, doi: 10.1109/LPT.2017.2735185.

[91] Y. H. Chen, W. H. Shi, L. Feng, X. Y. Xu, and M. Y. Shang-Guan, “Study on simultaneous sensing of gas concentration and temperature in one-dimensional photonic crystal,” *Superlattices Microstruct.*, vol. 131, pp. 53–58, Jul. 2019, doi: 10.1016/J.SPMI.2019.05.033.

[92] V. K. Rai, “Temperature sensors and optical sensors,” *Appl. Phys. B 2007 882*, vol. 88, no. 2, pp. 297–303, Jul. 2007, doi: 10.1007/S00340-007-2717-4.

[93] S. W. James and R. P. Tatam, “Optical fibre long-period grating sensors:

Characteristics and application," *Meas. Sci. Technol.*, vol. 14, no. 5, p. R49, Mar. 2003, doi: 10.1088/0957-0233/14/5/201.

[94] Z. M. Zheng, Y. Sen Yu, X. Y. Zhang, Q. Guo, and H. B. Sun, "Femtosecond Laser Inscribed Small-Period Long-Period Fiber Gratings with Dual-Parameter Sensing," *IEEE Sens. J.*, vol. 18, no. 3, pp. 1100–1103, Feb. 2018, doi: 10.1109/JSEN.2017.2761794.

[95] B. Zhang and M. Kahrizi, "High-temperature resistance Fiber Bragg grating temperature sensor fabrication," *IEEE Sens. J.*, vol. 7, no. 4, pp. 586–591, Apr. 2007, doi: 10.1109/JSEN.2007.891941.

[96] T. Wang, K. Liu, J. Jiang, M. Xue, P. Chang, and T. Liu, "A large range temperature sensor based on an angled fiber end," *Opt. Fiber Technol.*, vol. 45, pp. 19–23, Nov. 2018, doi: 10.1016/J.YOFTE.2018.04.008.

[97] Y. M. Raji, H. S. Lin, S. A. Ibrahim, M. R. Mokhtar, and Z. Yusoff, "Intensity-modulated abrupt tapered Fiber Mach-Zehnder Interferometer for the simultaneous sensing of temperature and curvature," *Opt. Laser Technol.*, vol. 86, pp. 8–13, Dec. 2016, doi: 10.1016/J.OPTLASTEC.2016.06.006.

[98] X. Dong, H. Du, X. Sun, and J. Duan, "Simultaneous Strain and Temperature Sensor Based on a Fiber Mach-Zehnder Interferometer Coated with Pt by Iron Sputtering Technology," *Mater. 2018, Vol. 11, Page 1535*, vol. 11, no. 9, p. 1535, Aug. 2018, doi: 10.3390/MA11091535.

[99] F. Mumtaz *et al.*, "A Design of Taper-Like Etched Multicore Fiber Refractive Index-Insensitive a Temperature Highly Sensitive Mach-Zehnder Interferometer," *IEEE Sens. J.*, vol. 20, no. 13, pp. 7074–7081, Jul. 2020, doi: 10.1109/JSEN.2020.2978533.

[100] M. de F. F. Domingues and A. Radwan, "Low Cost Silica Optical Fiber Sensors," pp. 49–59, 2017, doi: 10.1007/978-3-319-47349-9_3.

[101] J. B. Rosolem, C. Floridia, A. A. Juriollo, and E. W. Bezerra, "Comparative analysis of fiber grating versus fiber powering for fiber optical sensing applications," *SBMO/IEEE MTT-S Int. Microw. Optoelectron. Conf. Proc.*, pp. 641–645, 2009, doi: 10.1109/IMOC.2009.5427503.

[102] J. Li *et al.*, "Low-cost wearable device based D-shaped single mode fiber curvature sensor for vital signs monitoring," *Sensors Actuators A Phys.*, vol. 337, p. 113429, Apr. 2022, doi: 10.1016/J.SNA.2022.113429.

[103] Y. Ding, X. Dai, and T. Zhang, "Low-cost fiber-optic temperature measurement system for high-voltage electrical power equipment," *IEEE Trans. Instrum. Meas.*, vol. 59, no. 4, pp. 923–933, Apr. 2010, doi: 10.1109/TIM.2009.2030930.

[104] M. C. P. Soares, T. D. Cabral, B. F. Mendes, V. A. da Silva, E. B. Tambourgi, and E. Fujiwara, "Technical and Economic Viability Analysis of Optical Fiber Sensors for Monitoring Industrial Bioreactors," *Eng. Proc. 2020, Vol. 2, Page 57*, vol. 2, no. 1, p. 57, Nov. 2020, doi: 10.3390/ECSA-7-08161.

4. Optical Fiber Sensor for Measuring Mercury in water

4.1 Introduction and Background

As aforementioned, water contamination by the toxic mercury is one of the most persistent global concern because contamination with this heavy metal ions may have severe effects on human health and the environment as a result of its bioaccumulation and methylation [1]–[3]. Among variants of this metal, mercury ions (Hg^{2+}) are the most stable form of inorganic mercury in the aqueous medium and, due to high penetration property, have the ability to quickly enter in the human body through the skin, the gastrointestinal tissues, and by respiration, causing severe health problems even at low concentrations, such as brain damage, endocrine system damage, and kidney failure [4], [5]. This is a cause for concern because humans are exposed to multiple contaminated sources by industrial activities, including coal and gold mining, solid waste incineration, domestic waste discharge, fossil fuel combustion, and chemical manufacturing [6], [7]. Among these contamination sources, the disposal of mining washing of small-scale gold activities and artisanal mining is the primary origin of mercury pollution in many countries across the globe, including Colombia [8]–[10], where the communities are exposed to contaminated drinking water sources whose concentration for Hg^{2+} can exceed the upper limit of 2 ppb (10 nM), that has mandated the World Health Organization [11]. In poor and remote regions of the country the adequate water quality monitoring is limited by the lack of cost-effective detection technology for the analytical content of Hg^{2+} in their water sources.

Monitoring in situ of low concentration of mercury in drinking water demands the design of reliable techniques for rapid, efficient, and sensitive detection of ions Hg^{2+} in aqueous solutions. In this respect, the traditional techniques for Hg^{2+} monitoring in water include inductively coupled plasma mass spectrometry (ICP-MS) [12], atomic absorption spectroscopy (ASS) [13], [14], anodic stripping voltammetry [15], and atomic fluorescence

spectrometry [16], [17]. In spite of the fast and accurate measurement capabilities of these robust techniques, highly expensive equipment, sophisticated instrumentation, and complicated and multistep sample preparation are required for detection of the ions in water, which complicates the in situ implementation [18]. In response to this drawback, several analytical methods are currently available for heavy metals detection in water such as electrochemical [19], colorimetric [20], and optical sensors employing organic compounds [21], metal nanoparticles [22], polymeric materials [23], nucleic acids [24], and foldamers [25] as chemical recognition elements of Hg^{2+}. Although selective, sensitive, compact, and with rapid detection capabilities, most of these techniques require sophisticated instrumentation for their fabrication and are usually accompanied by robust equipment which limits the implementation in remote regions [26]. With such difficulties in mind, recent research interest has focused on developing optical fiber sensors that take full advantage of the already mentioned virtues of this technology, such as compact size, portability, rapidity, cost-effectiveness, simplicity, label free detection, resistance to degradation, immunity to electromagnetic interference, and remote sensing potential [27].

Within the optical fiber sensing technologies that have been reported for Hg^{2+} detection in water, are included the fiber evanescent wave [28], interferometers [29], surface plasmon resonance (SPR) [24], fluorescence [30], and fiber grating [31]–[33] sensors. All of these techniques have demonstrated the ability to detect concentrations of Hg^{2+} in water up to 1 ppb, but requiring complex and expensive equipment to nano deposit the metal coating and heavy metal ion sensitive films, which make them more complicated to be fabricated and difficult to be effectively implement [28]. Therefore, the need for fast, easy, and economical monitoring technology of drinking water samples on-site and real time persists nowadays.

As a response to the challenges presented, in this chapter a proposal of a cost-effective (less than $10 USD for materials and manufacturing), simple to construct, and relatively easy to implement functionalized sensors based on fiber optics are evaluated in order to selectively detect ions Hg^{2+} in water at low concentrations, up to 1 ppb. This section describes how E-SMS structures and fiber optics with slanted end previously characterized were functionalized and tested as sensors for the selective detection of serial solutions of Hg^{2+} in water. The proposed functionalization protocol was evaluated immobilizing a CS/Fe_2O_3 thin film for the absorption of mercury ions on the sensitive surface of the fiber probes. The experimental results obtained in this chapter demonstrates the ability to detect

selectively chemical interactions up to 1 ppb (0.001µg/mL) of Hg^{2+} in water to both types of sensors, with sensitivities of up 290 pm/(µg/mL) for the sensor based on the E-SMS structure and -0.07 dBm/(µg/mL) for the sensor based on the slanted end structure.

4.2 Materials and Methods

4.2.1 Activation and samples preparation

Sensors based on slanted fiber ends and E-SMS structures are fabricated separately following the methodology described in the Chapter 3, Sections 3.2.3 and 3.3.3. Subsequently, an activation protocol is developed in order to provide these sensors the capability to detect the presence of the specific heavy metal ions in water. The sensing surfaces of the twelve pieces of each type of these structures were activated with a composite that can detect the presence of Hg^{2+}, as illustrated in Figure 4-1. This activation stage is necessary because, although the slated fiber ends and the E-SMS structure can detect optically refractive index changes into water samples [34], the heavy metal ions solution present similar refractive indices for lowest concentration, which makes very difficult the selective measure of Hg^{2+}.

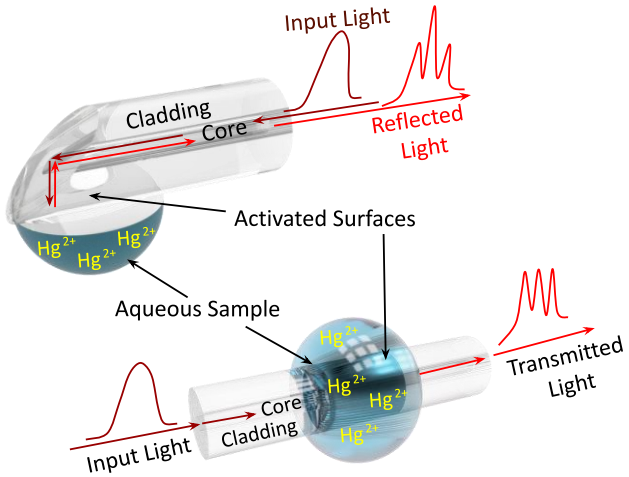

Figure 4-1: Activated slanted fiber end (above) and E-SMS structure (below) with Cs/Fe_2O_3 thin layer for detection of Hg^{2+} in water.

Several different recognition elements for mercury chemical sensors can be founded in literature [35]–[39]. In particular, one that can be implemented with relative ease is the reported in [40] which consists in the coating of the sensing area of the structures with a nanostructured chitosan (CS)/maghemite (γ-Fe_2O_3) composite thin film. The results

obtained in that work validate the ability of a CS/Fe_2O_3 coating for detection of Hg^{2+} using surface plasmon resonance technology, but a selective detection was not demonstrated in that manuscript. In response to this opportunity, the activation protocol-based on a CS/Fe_2O_3 composite was carried out in this thesis in order to verify the capability of the slanted fiber ends and the E-SMS structures to rapidly detect, with high sensitivity and selectivity, Hg^{2+} in water.

Table 4-1: Reagents used in the immobilization of the nanostructured chitosan/maghemite (CS/Fe2O3) composite.

Reagent	Formula	Manufacturer	Property
Iron (III) oxide	Fe_2O_3	Merck Millipore	99.9 %
Medium molecular weight chitosan	CS	Sigma Aldrich	Deacetylation 75–85%
Ammonia	NH_3	Fisher Scientific	25 % w/w
Acetic acid	CH_3COOH	Thermo Scientific	99.7 %
Mercury (II) chloride	$HgCl_2$	Sigma Aldrich	98 %
Nickel (II) chloride	$NiCl_2$	Merck Millipore	97 %
Copper (II) chloride	$CuCl_2$	Merck Millipore	97 %
Platinum (II) chloride	$PtCl_2$	Sigma Aldrich	98 %
Sodium chloride	NaCl	HiMedia Labs	99 %
Iron (III) chloride	$FeCl_3$	Merck Millipore	99 %
Hydrochloric acid	HCl	HiMedia Labs	99 %
Ethylenediaminetetraacetic acid	EDTA	Merck Millipore	99 %

The reagents used in the activation process are listed in the Table 4-1. In the preparation of the CS/Fe_2O_3 solution, 200 mg of Fe_2O_3 were dissolved in 50 ml of distilled water. Then, 10 mL of NH_3 (25%) and 0.615 mg of EDTA were added as precipitating agent and as capping agent to the solution, respectively. The resulting solution was stirred for 2 h at 50 °C until all the dark red precipitate of Fe_2O_3-EDTA was formed. Immediately after, the nano Fe_2O_3-EDTA precipitated was rinsed with distilled water and left to dry at 70 °C for 4 h. Simultaneously, 400 mg of chitosan were dissolved in 50 mL of 1% acetic acid. The solution was stirred for 8 h until all the chitosan was dissolved in the acetic acid. Finally, 30 mg of precipitate of Fe2O3-EDTA were added to 10 mL of the chitosan solution and sonicated at 20 pulses/min at room temperature for 15 min.

To the activation process, the slanted fiber ends and the E-SMS structures were immersed into the prepared chitosan/maghemite solution. Twelve units of each of the two fiber optics structures were cleaned using acetone and dipped into Cs/Fe_2O_3 solution at a feed rate of

70 mm/min, remaining immersed for 7 min, using a CNC milling machine (Haas® TM-1P), which served as dip coating equipment. The coated slanted fiber ends and the coated E-SMS structures were kept in vacuum oven at 50 °C for 5 h and washed with deionized water before detection test of metal ions in water.

The following chlorides of analytical grade: $HgCl_2$, $NiCl_2$, $CuCl_2$, $PtCl_2$, NaCl, and $FeCl_3$, were used for the preparation of solutions of heavy metal ions in water. 1 mg/L stock solutions of all the six heavy metal ions (Hg^{2+}, Ni^{2+}, Cu^{2+}, Pt^{2+}, Na^{+}, and Fe^{3+}) were made by adding 1.4, 2.3, 2.2, 2.5, 1.4, and 3 mg sample accordingly, each in 1 mL of deionized water. The heavy metal ions aqueous solutions were diluted with deionized water to produce solutions with concentrations of 100, 10, 1, 0.1, 0.01, and 0.001 µg/mL.

4.2.2 Experimental setup

Once the activation process was carried out, a series of detection tests were performed using the experimental setup shown in Figure 4-2, (a) for the sensors based on slanted fiber ends and (b) for the sensors-based E-SMS structures. For the former, a SLED with wavelength in the range of 1225 nm to 1405 nm was used as the light source. Here the reflection spectrum was measured using the aforementioned OSA. The light from the SLED was coupled into the sensor based on slated fiber end via a directional coupler TW1300R5F2 (Thorlabs®). To study the response of the reflection spectrum to the aqueous solution with heavy metal ions, whose concentrations range from 0.001 (1 ppb) to 100 µg/mL, the optical fibers were placed along the V-groove in the test piece ensuring that the slanted surface of the end was facing upwards while the container for the aqueous solution was placed underneath, as shown in detail in Figure 4-2 (a). The light that propagates backwards after illuminating the sensing region superposes and causes interference in the output of the fiber which can be observed in the OSA. The intensity response was recorded when the cylindrical surface of the cladding of the fiber tip was in contact with the aqueous solutions. Similarly, a wavelength response was recorded in the OSA when the sensitive surface of the MMF of the E-SMS structure was put in contact with serial aqueous solutions of heavy metal ions using the already descripted setup shown in Figure 4-2 (b). All tests were carried out at room temperature, considering that the temperature fluctuation was not higher than ± 2 °C, which implies an error less than ±20 pm in the spectrum response of the sensors.

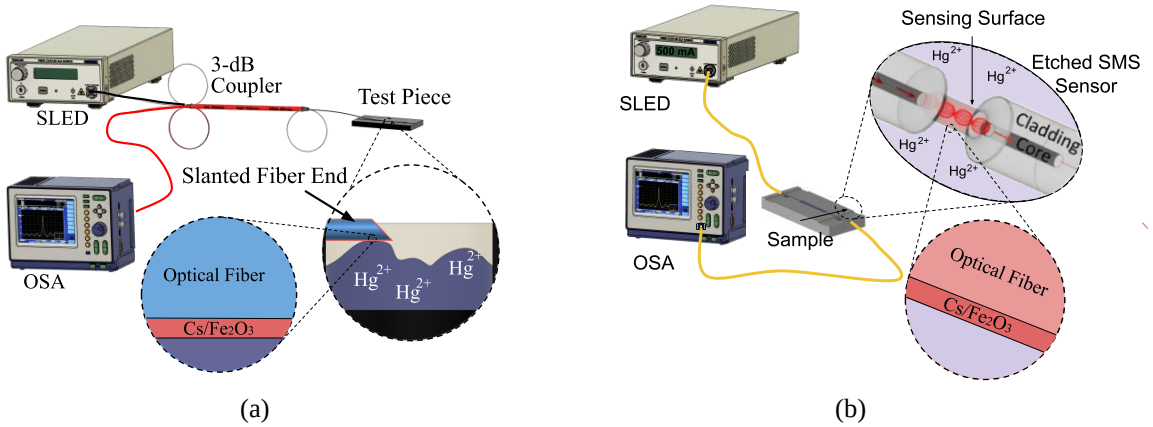

Figure 4-2: The experimental setup used to test the mercury detection performance of fabricated sensors based on slanted fiber (a) and the sensor based on E-SMS fiber (b). The Cs/Fe_2O_3 layer deposited onto the sensing surface of the fiber structures is shown in detail.

The protocol used for the detection consisted of the following steps: (1) A first rinse using deionized water was performed to clean the activated surface of each of the optical fiber structures. (2) The dirty deionized water was removed followed by the filling of the cavity of the test piece with deionized water for 3 min while a measurement of the optical spectrum was recorded with the OSA. This first spectrum corresponded to the base line. (3) deionized water was removed and the desired Hg^{2+} in water sample was put in place while the spectrum measurements were taken for 10 min. For each of the aqueous samples with Hg^{2+} this protocol was repeated. The difference in wavelength between a peak on the base line with deionized water and the same peak measured after 10 min of Hg^{2+} interaction was taken as the sensor response. This response is directly related to the sample concentration due to the refractive index change in the sensing surface of the slanted fiber end and the E-SMS structure that result from the absorption of Hg^{2+} ions.

The selectivity of the slanted fiber end and the E-SMS structures activated with Cs/Fe_2O_3 towards Hg^{2+} ions was determined by testing these optical fiber sensors with other metal ions commonly present in water: Ni^{2+}, Cu^{2+}, Pt^{2+}, Na^{+}, and Fe^{3+}. Using the same procedure described above, the response of the other activated sensors was evaluated putting in contact the sensitive surfaces with the aqueous solutions of these heavy metal ions at concentration of 1 µg/mL (1 ppm).

4.3 Results and discussion

The above-mentioned sensing protocol was implemented to experimentally evaluate the ability of the activated slanted fiber ends and the E-SMS structures to detect low concentrations of Hg^{2+} ions in water. The Figure 4-3 (a) and Figure 4-3 (c) show correspondingly the spectrum response for the activated optical fibers with slanted ends and the E-SMS structures to the different concentrations of Hg^{2+} in aqueous solutions. A decrease in the normalized reflection spectrum for the slanted end fiber and a red-shift for the E-SMS structure, is clearly observed as Hg^{2+} concentration changes and the absorption of the heavy metal ions on the sensing surface of both the slanted fiber end and the E-SMS sensor takes place. For its part, the spectrum response of the sensors to the concentration of Hg^{2+} in water is showed in the dose-response curves shown in Figure 4-3 (b) and Figure 4-3 (d). The sensitivities were determined from the slopes of the dose-response curves, verifying that sensitivities of up 290 pm/(µg/mL) for the sensor based on the E-SMS structure and -0.07 dBm/(µg/mL) for the sensor based on the slanted end structure, were obtained. These results show that both types of sensors can detect chemical interactions up to a minimum of 0.001µg/mL (one part per billion) of Hg^{2+} in water, proving to be two very promising, rapid, and potentially suitable cost-effective sensing technology to chemical detection at low concentrations of Hg^{2+} ions in drinking water.

Additionally, the response of the sensors to various metal ions in solution at a concentration of 1 µg/mL (1 ppm) were studied to evaluate the selectivity of these fiber structures activated with CS/Fe_2O_3 towards Hg^{2+} ions. As shown in Figure 4-4 (a) and Figure 4-4 (b), compared to Ni^{2+}, Cu^{2+}, Pt^{2+}, Na^{+}, and Fe^{3+} ions, the selective adsorption of Hg^{2+} by the nanostructured CS/Fe_2O_3 thin sensitive film, and therefore the response, was much greater, at least 40% bigger for the worst case, which was obtained with the Ni^{2+} ions in both sensors. This figure proves the selectivity of these practical and cost-effective sensors towards Hg^{2+} ions over other heavy metal ions commonly found in water. Combined with the ability to detect up to a minimum of 0.001µg/mL (one part per billion) of Hg^{2+} in water, this selectivity is comparable to that achieved with other aforementioned robust techniques, but at a fraction of the cost (at least ten times less costly). In that sense, the characteristics of ease of fabrication and low-cost of the optical fiber with slanted ends and the E-SMS structure activated with CS/Fe_2O_3, offer high potential, and makes them very promising for the development of simple, reliable, and cost-effective platform system for on-site detection and low concentrations monitoring of mercury in water sources potentially contaminated,

that is precisely the final objective in this thesis. The integration of theses sensors into a portable platform is detailly reported in the chapter 6.

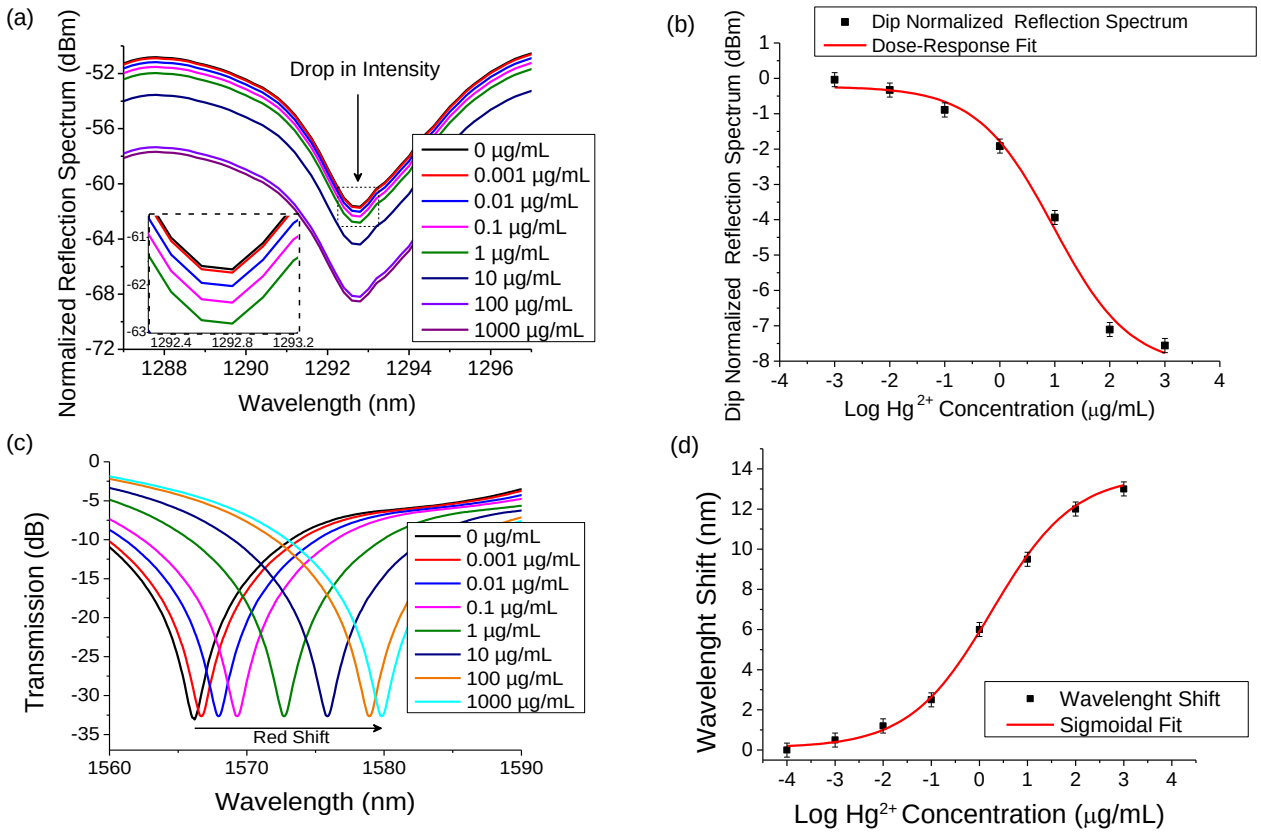

Figure 4-3: (a) Spectral response of the optical fiber sensors with slanted ends for different concentrations of Hg^{2+} ions in water. (b) Dose-response curve of Hg^{2+} ions in water of the slanted fiber end sensor. (c) Spectral response of the E-SMS sensor for different concentrations of Hg^{2+} ions in water. (d) Dose-response curve of Hg^{2+} ions in water of the E-SMS sensor

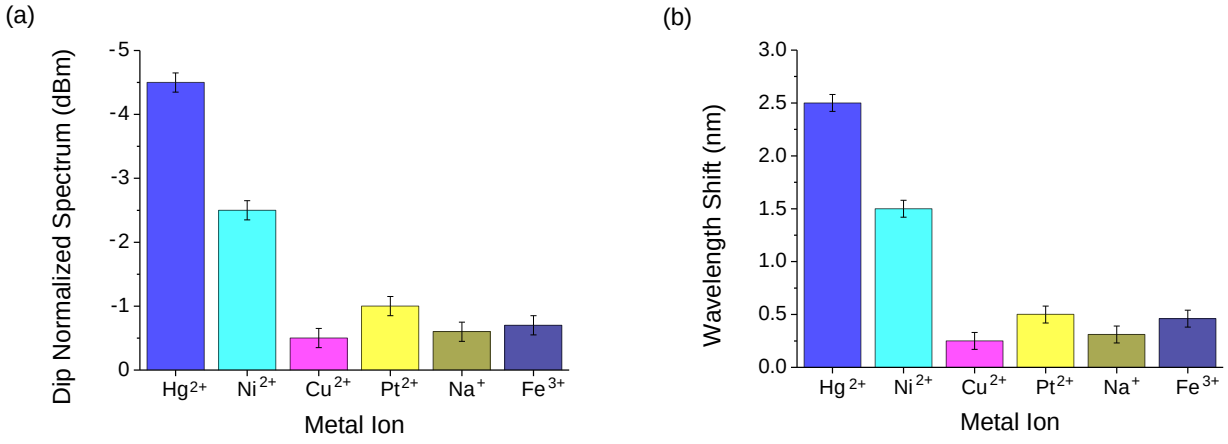

Figure 4-4: (a) Responses of the sensor based on a slanted fiber end and (b) responses of the E-SMS sensor to different metal ions.

Finally, the research work conducted with the optical fibers with slanted ends and the E-SMS structures functionalized for the detection of mercury in water gave rise to some contributions reported in the following manuscript submitted to an indexed journal of international circulation and presented at an international conference:

Brayan Patiño-Jurado, Arturo Gaviria-Calderón, Juan F Botero-Cadavid, and Jorge Garcia-Sucerquia. “Competitive Fiber Optics Sensors for Highly Selective detection of Mercury in Water.” Applied Optics 62.3 (2023): 592-600.

Arturo Gaviria-Calderón, Brayan Patiño-Jurado, Juan F Botero-Cadavid, and Jorge Garcia-Sucerquia*. “Mercury detection in water based on an E-SMS optical fiber structure.”* Latin America Optics and Photonics Conference. Optica Publishing Group, 2022.

4.4 References for Chapter 4

[1] S. M. Ullrich, M. A. Ilyushchenko, I. M. Kamberov, and T. W. Tanton, “Mercury contamination in the vicinity of a derelict chlor-alkali plant. Part I: Sediment and water contamination of Lake Balkyldak and the River Irtysh,” *Sci. Total Environ.*, vol. 381, no. 1–3, pp. 1–16, Aug. 2007, doi: 10.1016/J.SCITOTENV.2007.02.033.

[2] L. Wang *et al.*, “Remediation of mercury contaminated soil, water, and air: A review of emerging materials and innovative technologies,” *Environ. Int.*, vol. 134, p. 105281, Jan. 2020, doi: 10.1016/J.ENVINT.2019.105281.

[3] L. T. Budnik and L. Casteleyn, “Mercury pollution in modern times and its socio-medical consequences,” *Sci. Total Environ.*, vol. 654, pp. 720–734, Mar. 2019, doi: 10.1016/J.SCITOTENV.2018.10.408.

[4] F. Khan, S. Momtaz, and M. Abdollahi, “The relationship between mercury exposure and epigenetic alterations regarding human health, risk assessment and diagnostic strategies,” *J. Trace Elem. Med. Biol.*, vol. 52, pp. 37–47, Mar. 2019, doi: 10.1016/J.JTEMB.2018.11.006.

[5] Natasha *et al.*, “A critical review of mercury speciation, bioavailability, toxicity and detoxification in soil-plant environment: Ecotoxicology and health risk assessment,” *Sci. Total Environ.*, vol. 711, p. 134749, Apr. 2020, doi: 10.1016/J.SCITOTENV.2019.134749.

[6] A. R. C. Grigg, R. Kretzschmar, R. S. Gilli, and J. G. Wiederhold, “Mercury isotope signatures of digests and sequential extracts from industrially contaminated soils and sediments,” *Sci. Total Environ.*, vol. 636, pp. 1344–1354, Sep. 2018, doi: 10.1016/J.SCITOTENV.2018.04.261.

[7] D. Raj and S. K. Maiti, “Sources, toxicity, and remediation of mercury: an essence review,” *Environ. Monit. Assess. 2019 1919*, vol. 191, no. 9, pp. 1–22, Aug. 2019, doi: 10.1007/S10661-019-7743-2.

[8] E. Bernalte *et al.*, “Rapid and on-site simultaneous electrochemical detection of copper, lead and mercury in the Amazon river,” *Sensors Actuators B Chem.*, vol. 307, p. 127620, Mar. 2020, doi: 10.1016/J.SNB.2019.127620.

[9] K. W. Torrance, S. D. Redwood, and A. Cecchi, “The impact of artisanal gold mining, ore processing and mineralization on water quality in Marmato, Colombia,” *Environ. Geochem. Health*, vol. 43, no. 10, pp. 4265–4282, Oct. 2021, doi: 10.1007/S10653-021-00898-Y/TABLES/4.

[10] L. J. Esdaile and J. M. Chalker, “The Mercury Problem in Artisanal and Small-Scale Gold Mining,” *Chem. – A Eur. J.*, vol. 24, no. 27, pp. 6905–6916, May 2018, doi: 10.1002/CHEM.201704840.

[11] A. Riaz, S. Khan, S. Muhammad, and M. T. Shah, “Mercury Contamination in Water and Sediments and the Associated Health Risk: A Case Study of Artisanal Gold-mining,” *Mine Water Environ. 2019 384*, vol. 38, no. 4, pp. 847–854, May 2019, doi: 10.1007/S10230-019-00613-5.

[12] D. Dai *et al.*, “Recent Progress in Functional Materials for Selective Detection and Removal of Mercury(II) Ions,” *Adv. Funct. Mater.*, vol. 31, no. 1, p. 2006168, Jan. 2021, doi: 10.1002/ADFM.202006168.

[13] A. Thongsaw, Y. Udnan, G. M. Ross, and W. C. Chaiyasith, “Speciation of mercury in water and biological samples by eco-friendly ultrasound-assisted deep eutectic solvent based on liquid phase microextraction with electrothermal atomic absorption spectrometry,” *Talanta*, vol. 197, pp. 310–318, May 2019, doi: 10.1016/J.TALANTA.2019.01.018.

[14] A. Thongsaw, R. Sananmuang, Y. Udnan, G. M. Ross, and W. C. Chaiyasith, “Speciation of mercury in water and freshwater fish samples using two-step hollow fiber liquid phase microextraction with electrothermal atomic absorption spectrometry,” *Spectrochim. Acta Part B At. Spectrosc.*, vol. 152, pp. 102–108, Feb. 2019, doi: 10.1016/J.SAB.2018.12.012.

[15] H. Xiao, W. Wang, S. Pi, Y. Cheng, and Q. Xie, “Anodic stripping voltammetry analysis of mercury(II) on a pyridine-Au/pyridine/glassy carbon electrode,” *Sensors Actuators B Chem.*, vol. 317, p. 128202, Aug. 2020, doi: 10.1016/J.SNB.2020.128202.

[16] Y. Zhang, M. Miró, and S. D. Kolev, “A novel on-line organic mercury digestion method combined with atomic fluorescence spectrometry for automatic mercury speciation,” *Talanta*, vol. 189, pp. 220–224, Nov. 2018, doi: 10.1016/J.TALANTA.2018.06.083.

[17] N. Xia *et al.*, “The detection of mercury ion using DNA as sensors based on fluorescence resonance energy transfer,” *Talanta*, vol. 192, pp. 500–507, Jan. 2019, doi: 10.1016/J.TALANTA.2018.08.086.

[18] S. Şahin, M. O. Caglayan, and Z. Üstündağ, “A review on nanostructure-based mercury (II) detection and monitoring focusing on aptamer and oligonucleotide biosensors,” *Talanta*, vol. 220, p. 121437, Dec. 2020, doi:

10.1016/J.TALANTA.2020.121437.

[19] Y. Wang *et al.*, “Electrochemical aptasensor based on gold modified thiol graphene as sensing platform and gold-palladium modified zirconium metal-organic frameworks nanozyme as signal enhancer for ultrasensitive detection of mercury ions,” *J. Colloid Interface Sci.*, vol. 606, pp. 510–517, Jan. 2022, doi: 10.1016/J.JCIS.2021.08.055.

[20] F. Tanvir, A. Yaqub, S. Tanvir, R. An, and W. A. Anderson, “Colorimetric Detection of Mercury Ions in Water with Capped Silver Nanoprisms,” *Mater. 2019, Vol. 12, Page 1533*, vol. 12, no. 9, p. 1533, May 2019, doi: 10.3390/MA12091533.

[21] S. K. Patil and D. Das, “A novel rhodamine-based optical probe for mercury(II) ion in aqueous medium: A nanomolar detection, wide pH range and real water sample application,” *Spectrochim. Acta Part A Mol. Biomol. Spectrosc.*, vol. 225, p. 117504, Jan. 2020, doi: 10.1016/J.SAA.2019.117504.

[22] G. M. Shukla, N. Punjabi, T. Kundu, and S. Mukherji, “Optimization of Plasmonic U-Shaped Optical Fiber Sensor for Mercury Ions Detection Using Glucose Capped Silver Nanoparticles,” *IEEE Sens. J.*, vol. 19, no. 9, pp. 3224–3231, May 2019, doi: 10.1109/JSEN.2019.2893270.

[23] T. Velempini, K. Pillay, X. Y. Mbianda, and O. A. Arotiba, “Application of a Polypyrrole/Carboxy Methyl Cellulose Ion Imprinted Polymer in the Electrochemical Detection of Mercury in Water,” *Electroanalysis*, vol. 30, no. 11, pp. 2612–2619, Nov. 2018, doi: 10.1002/ELAN.201800445.

[24] S. Jia, C. Bian, J. Sun, J. Tong, and S. Xia, “A wavelength-modulated localized surface plasmon resonance (LSPR) optical fiber sensor for sensitive detection of mercury(II) ion by gold nanoparticles-DNA conjugates,” *Biosens. Bioelectron.*, vol. 114, pp. 15–21, Aug. 2018, doi: 10.1016/J.BIOS.2018.05.004.

[25] M. M. Rhaman *et al.*, “Highly selective and sensitive macrocycle-based dinuclear foldamer for fluorometric and colorimetric sensing of citrate in water,” *Sci. Reports 2017 81*, vol. 8, no. 1, pp. 1–11, Jan. 2018, doi: 10.1038/s41598-017-18322-w.

[26] J. W. Lim, T. Y. Kim, and M. A. Woo, “Trends in sensor development toward next-generation point-of-care testing for mercury,” *Biosens. Bioelectron.*, vol. 183, p. 113228, Jul. 2021, doi: 10.1016/J.BIOS.2021.113228.

[27] N. A. M. A. Ghafar, A. M. Markom, M. A. Markom, and A. R. Muhammad, “Optical Fiber Sensor for Heavy Chemical Detection: An Overview,” *J. Phys. Conf. Ser.*, vol. 2075, no. 1, p. 012010, Oct. 2021, doi: 10.1088/1742-6596/2075/1/012010.

[28] Y. nan Zhang, Y. Sun, L. Cai, Y. Gao, and Y. Cai, “Optical fiber sensors for measurement of heavy metal ion concentration: A review,” *Measurement*, vol. 158, p. 107742, Jul. 2020, doi: 10.1016/J.MEASUREMENT.2020.107742.

[29] R. X. Tan, M. Ibsen, and S. C. Tjin, “Optical fiber refractometer based metal ion sensors,” *Chemosensors*. 2019, doi: 10.3390/chemosensors7040063.

[30] N. De Acha, C. Elosúa, and F. J. Arregui, “Development of an Aptamer Based Luminescent Optical Fiber Sensor for the Continuous Monitoring of Hg2+ in Aqueous

Media," *Sensors 2020, Vol. 20, Page 2372*, vol. 20, no. 8, p. 2372, Apr. 2020, doi: 10.3390/S20082372.

[31] S. Y. Tan, S. C. Lee, T. Okazaki, H. Kuramitz, and F. Abd-Rahman, "Detection of mercury (II) ions in water by polyelectrolyte–gold nanoparticles coated long period fiber grating sensor," *Opt. Commun.*, vol. 419, pp. 18–24, Jul. 2018, doi: 10.1016/J.OPTCOM.2018.02.069.

[32] S. Y. Tan, S. C. Lee, H. Kuramitz, and F. Abd-Rahman, "A novel hybrid long period fiber grating-diffusive gradient in thin films sensor system for the detection of mercury (II) ions in water," *Optik (Stuttg).*, vol. 194, p. 163040, Oct. 2019, doi: 10.1016/J.IJLEO.2019.163040.

[33] S. Y. Tan, S. C. Lee, T. Okazaki, H. Kuramitz, and F. Abd-Rahman, "Detection of mercury (II) ions in water by polyelectrolyte–gold nanoparticles coated long period fiber grating sensor," *Opt. Commun.*, 2018, doi: 10.1016/j.optcom.2018.02.069.

[34] B. Patiño-Jurado, A. Gaviria-Calderón, J. F. Botero-Cadavid, and J. Garcia-Sucerquia, "Intensity-modulated refractive index sensor based on optical fiber with slanted end," Opt. Laser Technol., vol. 157, p. 108700, Jan. 2023, doi: 10.1016/J.OPTLASTEC.2022.108700.

[35] G. Elias, S. Díez, H. Zhang, and C. Fontàs, "Development of a new binding phase for the diffusive gradients in thin films technique based on an ionic liquid for mercury determination," *Chemosphere*, vol. 245, p. 125671, Apr. 2020, doi: 10.1016/J.CHEMOSPHERE.2019.125671.

[36] K. Pi, J. Liu, and P. Van Cappellen, "Direct Measurement of Aqueous Mercury(II): Combining DNA-Based Sensing with Diffusive Gradients in Thin Films," *Environ. Sci. Technol.*, vol. 54, no. 21, pp. 13680–13689, Nov. 2020, doi: 10.1021/ACS.EST.0C03870/ASSET/IMAGES/MEDIUM/ES0C03870_M005.GIF.

[37] F. N. Allouche, "A user-friendly Ulva lactuca/chitosan composite bead for mercury removal," *Inorg. Chem. Commun.*, vol. 130, p. 108747, Aug. 2021, doi: 10.1016/J.INOCHE.2021.108747.

[38] I. Zawierucha, A. Nowik-Zajac, J. Lagiewka, and G. Malina, "Separation of Mercury(II) from Industrial Wastewater through Polymer Inclusion Membranes with Calix[4]pyrrole Derivative," *Membr. 2022, Vol. 12, Page 492*, vol. 12, no. 5, p. 492, Apr. 2022, doi: 10.3390/MEMBRANES12050492.

[39] Y. nan Zhang, L. Zhang, B. Han, P. Gao, Q. Wu, and A. Zhang, "Reflective mercury ion and temperature sensor based on a functionalized no-core fiber combined with a fiber Bragg grating," *Sensors Actuators B Chem.*, vol. 272, pp. 331–339, Nov. 2018, doi: 10.1016/J.SNB.2018.05.168.c

[40] N. I. M. Fauzi *et al.*, "Nanostructured Chitosan/Maghemite Composites Thin Film for Potential Optical Detection of Mercury Ion by Surface Plasmon Resonance Investigation," *Polym. 2020, Vol. 12, Page 1497*, vol. 12, no. 7, p. 1497, Jul. 2020, doi: 10.3390/POLYM12071497.

5. Optical Fiber Sensor for Detecting Biological Species.

5.1 Introduction and Background

In recent decades, biological recognition of elements has attracted great interest in diverse research fields such as analytical chemistry, biological engineering, medical diagnosis, and food safety inspection. In all of these research areas the detection and analysis of biological species such as proteins, bacteria, toxins, viruses, glucose, among others, is of significant importance, which creates a need for reliable simple, rapid, highly selective, and in-situ biological sensing technology [1]–[3] [4]–[6]. In particular, to detect proteins various robust monitoring techniques have been reported in the literature, including but not limited to enzyme-linked immunosorbent assays (ELISAs) [7], [8], and the polymerase chain reaction (PCR) test [9], [10]. Although these methods are the most frequently used to detect proteins, they require multi-step processes and well-trained personnel, which increases both the time and cost of the detection [11]–[13]. As a consequence, many alternative methods such as optical [14], electrochemical [15], thermometric [16], [17], piezoelectric [18], or magnetic [19] biosensors have been developed as response to the mentioned difficulties of the robust techniques. The most of these conventional diagnosis methods still have, however, some disadvantages such as long procedures, expensive equipment and reagents, specialized personnel, lack of portability, low sensitivities, and the need of biomarkers [20]. In response to those difficulties, fiber optics biosensing technology is presented as a promising technology to mitigate the issues of the traditional sensing methods.

Many optical fiber biosensors have been reported in recent decades showing promising results for protein detection. These widely investigated techniques based on fiber optics sensors can be divided according the sensing principle into three broad groups: Fiber Bragg gratings-based (FBG) biosensors [21]–[24], surface plasmon resonance based (SPR) biosensors [25]–[27], and interferometric biosensors [1], [28]–[30]. These sensing structures have proven customized designed, high resolution, and wide measurement range; demonstrating high sensitivity and low limit of detection (LOD), up to 6000 dB/(µg/mL) with a LOD of 2 µg/mL (immunoglobulins) for FBG, 8 nm/(ug/mL) with a LOD of 1.5 µg/mL (C-reactive protein) for SPR, and 38 nm/(ug/mL) with a LOD of 1 µg/mL(Anti-BSA/BSA) for interferometer-based sensors [6], [31]–[36].

In this chapter, an innovative E-SMS sensing structure interferometer-based was investigated as a biosensor and applied to immunoassays (detection of an antigen/antibody binding). The modulation produced by the external perturbation used to detect biological interactions was carried out in a similar way to what it has been reported in the literature [37], [38]. In this thesis, however, as an additional novelty, the above demonstrated highly reproducible sensors were functionalized to experimentally prove the feasibility of the simple E-SMS structure to measure low concentration of biological species such as the molecule bovine serum albumin (BSA). This molecule has been used as a model protein in various studies, such as immunodiagnostic procedures [39] and [40]. Detection of BSA on its own, not as a model protein, has also gained interest recently as this protein serves as an indicator of milk and meat quality, and furthermore, it is known as an allergenic and a carrier protein [41]. Therefore, the development of new, efficient, fast, and straightforward methods for selective detection of BSA, as reported in this thesis, is desired. The analytical and experimental studio performed in this chapter demonstrates that the LOD of the optimized sensitive biosensor based on E-SMS structure can reach to 0.7 ug/mL.

5.2 Materials and Methods

5.2.1 E-SMS immobilization

Twelve sensors based E-SMS structures were fabricated following the methodology described in the section 3.3.3. Afterward, a functionalization and immobilization process

was developed depositing a biolayer onto the sensing surface of the E-SMS structures in order to provide these sensors the ability to detect the presence of low concentrations of Anti-BSA. The sensing surfaces of this structures were functionalized with BSA that can detect the presence of Anti-BSA during the antigen/antibody binding, as illustrated in Figure 5-1 (a).

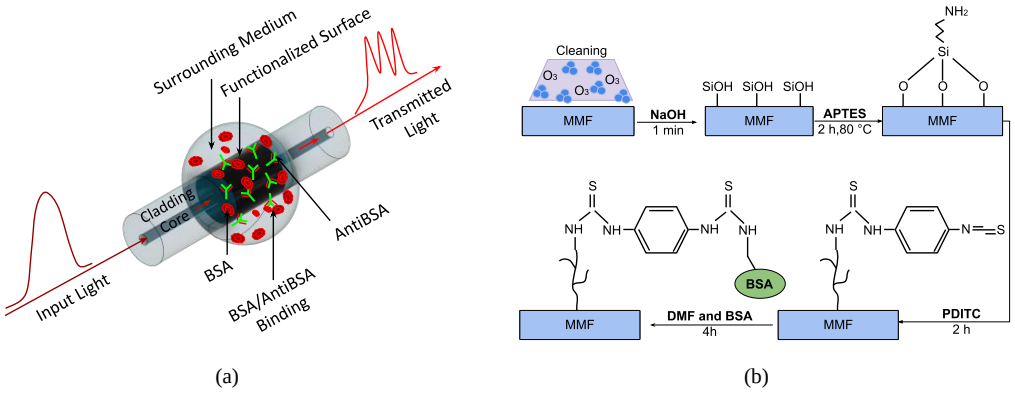

(a) (b)

Figure 5-1: E-SMS structure with immobilized antigen BSA for detection of Anti-BSA. (b) Antigen immobilization and surface functionalization procedure [42].

Table 5-1: Reagents used in the immobilization of the antigen BSA.

Reagent	Manufacturer	Concentration
Bovine serum albumin (BSA)	Sigma Aldrich	20 mg/mL
Anti-BSA	Sigma Aldrich	1 mg/mL
Piranha solution 3:1 (H_2SO_4 + H_2O_2)	Merck Millipore	H_2SO_4 96%, H_2O_2 30%
Sodium hydroxide (NaOH)	Merck Millipore	5 M
Triethoxysilane 3-(Aminopropyl)- (APTES)	Sigma Aldrich	10% (v/v)
Tris-(hydroxymethyl)aminomethane buffer (TRIS buffer)	Thermo Scientific	1 M, PH 7.4
Phosphate-buffered saline (PBS)	Sigma Aldrich	1X, PH 7.4
1,4-phenylenediisothiocyanate (PDITC)	Sigma Aldrich	0.3 M
Hydrochloric acid (HCl)	Honeywell Research	0.1 M
N,N-Dimethylformamide (DMF)	Merck Millipore	1.29
Ethanolamine	Sigma Aldrich	98%

The reagents used in the immobilization process are listed in Table 5-1. The immobilization process of the antigen BSA was based on the procedure detailed in [42] and consisted of three main steps: (1) activation, (2) antigen attachment, and (3) passivation, as shown in Figure 5-1 (b). In the first step, the E-SMS structures were cleaned in the piranha solution

for 5 minutes and immersed in a solution of NaOH 5M for 30 seconds. Then the E-SMS structures were incubated in APTES 10% (v/v) in distilled water for 4 h and dried for 1 h at room temperature. This silanization process modifies the surface affixing amino groups that allow the BSA to be attached onto the fiber surface. For the second step, fibers were incubated for 2 h in the PDITC solution (0.3 M PDITC in DMF) at room temperature, washed with DMF and immersed in a BSA solution culture for 4 hours, and then rinsed using PBS buffer to remove the unattached BSA molecules. Finally, the last step of the immobilization was the passivation which consists in the specific bonds blockage using Ethanolamine (10%), washed with TRIS buffer, washed with doubly distilled water and dried for 1 h at room temperature. The immobilized E-SMS were preserved refrigerating them at 4 °C.

5.2.2 Experimental setup and Anti-BSA detection

After the immobilization of BSA antigen process, the bio detection tests were performed using the experimental setup showed in Figure 5-2 and by placing in contact the sensitive surface of the E-SMS with serial solutions of antibody anti-BSA diluted in PBS buffer at concentrations of 100 µg/ml, 10 µg/ml, 1 µg/ml, 0.1 µg/ml, and 0.001 µg/ml. All tests were carried out at room temperature, considering that the temperature fluctuation was not higher than ± 2 °C, which implies an error less than ±20 pm in the spectrum response of the sensors [43]. The protocol used for the bio detection consisted of the following steps: (1) HCl was applied on the sensing surface of the functionalized E-SMS for 3 min to clean and break previous bonds, thus regenerating the biosensor. (2) The HCl solution was then removed followed by the application of the PBS 1X for 3 min while a measurement of the optical spectrum was being recorded by the OSA. This first spectrum corresponded to the base line. (3) PBS 1X buffer was removed and the desired antibody sample was put in place while the spectrum measurements were recorded for 10 min. For each Anti-BSA sample, this protocol was repeated. The difference in wavelength between a peak on the base line with PBS and the same peak measured after 10 min of antibody interaction was taken as the biosensor response. This response is related to the sample concentration due to the refractive index change in the sensing surface of the E-SMS that result from the anti BSA/BSA bonds.

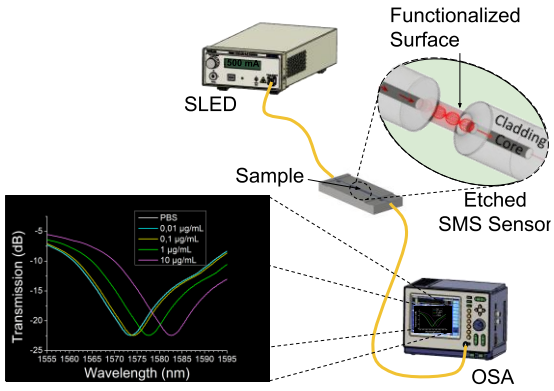

Figure 5-2: Experimental setup used to measure transmission spectra of the E-SMS sensor.

Once the ability of E-SMS biosensor to detect low concentration of Anti BSA was validated, an indirect competitive immunoassay was developed using the same sensing structures in order to determinate the limit of detection (LOD). The optimal concentrations of antigen and antibody were previously determined through numerous direct assays using the different concentrations of immobilized BSA and solutions of anti-BSA. The same experimental setup shown in Figure 5-2 was used and the concentration of immobilized BSA was fixed at 1 mg/ml, and the sample target of anti-BSA was fixed at 1 µg/ml in this competitive immunoassay. In this case, the protocol used for the bio detection was modified as follows: (1) HCl was applied in the sensing surface for 3 min to clean and break previous bonds. (2) The HCl solution was removed followed by the application of the PBS 1X for 3 min and the measurement of the optical spectrum was recorded as a base line. (3) PBS 1X buffer was rinsed and a sample of anti- BSA 1 µg/ml was applied while the measurements of the spectrum were taking for 10 min. The difference in wavelength between a peak on the base line with PBS and the same peak measured after 10 min of antibody interaction was taken as the sample target or maximum biosensor response. (4) The anti-BSA sample was removed and a mixture of equal parts of BSA 1 µg/ml and anti-BSA 0.01 µg/ml was placed onto the sensing surface for 10 min. Here, the difference in wavelength shifts due to the sample target and due to the anti-BSA/BSA mixture with respect to the base line with PBS was taken as the biosensor response. This procedure was repeated for different mixtures of anti-BSA/ BSA, in which the concentration of the former remains constant at 1 µg/ml and the latter varies between 0.01 and 100 µg/ml (in serial solutions).

5.3 Results and discussion

The ability of the E-SMS structure to detect anti-BSA was experimentally studied using the aforementioned biosensing protocol. Figure 5-3 (a) shows the spectrum tracking for the functionalized E-SMS sensors to the serial solutions of anti-BSA indicating the limiting concentration of Anti-BSA. A red-shift is clearly observed due to the change in the concentration of the antibody and the formation of anti-BSA/BSA bonds in the MMF section of the E-SMS structure. The spectrum response of the biosensor to the concentration of anti-BSA is summarized in a dose-response curve shown in Figure 5-3 (b). These results show that the E-SMS biosensor can detect low concentrations of up to 100 ng/mL of Anti-BSA proving to be promising and potentially suitable to bio-molecular detection at low concentrations. Moreover, a sensitivity of 2.3 nm/(µg/ml) is obtained from the slope on the inflection point of Figure 5-3 (b), obtaining a higher value than that reported for similar bio sensing technologies based on optical fibers such as those reported in [35] and [36], outperforming the former in 2 orders of magnitude and the latter in 3 orders of magnitude. This high sensitivity is justified by the fact that the antigen BSA of the target molecule anti-BSA was immobilized onto the transducer surface makes it highly specific to detect this protein. The antigen-antibody bond produces changes in refractive index near the sensing surface that are mostly affected by the coupling of the specific protein Anti-BSA and not by other proteins in the sample.

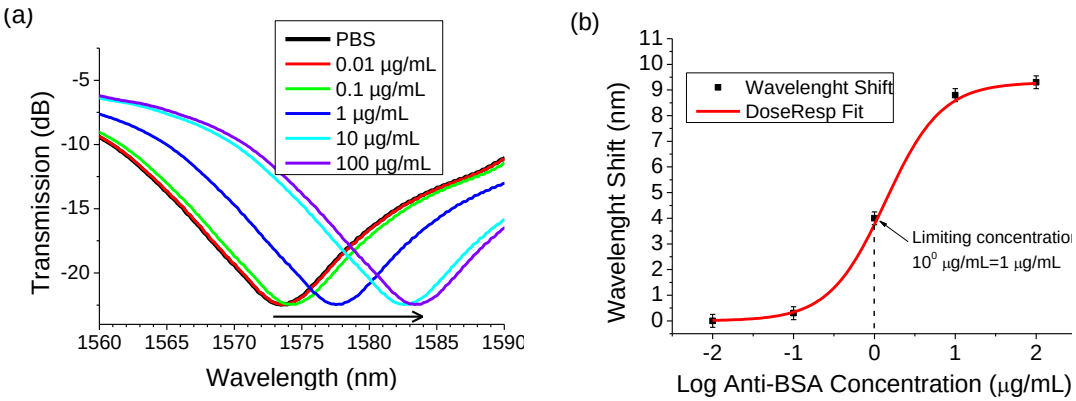

Figure 5-3: (a) Spectral response of the E-SMS biosensor for different concentrations of anti-BSA. (b) Dose-response curve of antiBSA of the E-SMS sensor.

On the other hand, the temporal response of the sensor and the results of the indirect competitive immunoassay are correspondingly summarized in panel (a) and (b) of Figure 5-4. Using the methodology described in [43] and [44], the inverse function of the percentage of inhibition graph is taken and the LOD can be obtained evaluating the point determined by the mean value of the % inhibition due entirely to the sample target of Anti BSA plus three times the maximum standard deviation of the % inhibition due to the mixture of BSA and Anti BSA. The obtained $\mathrm{LDO} = 0.7\ \mu\mathrm{g/ml}$ implies that que biosensor based on E-SMS structure can detect concentrations of Anti-BSA under 1 µg/ml, that is lower than the ones reported in [45], [46], and [34]. In addition, as can be interpreted from the little error bars of the standard deviation of the measurements of all functionalized sensors, the implemented protocol allows to obtain reproducible and repeatable E-SMS biosensors with response and sensitivity in the same order of magnitude. These obtained results validated that cost-effective (less than $10 USD for materials and manufacturing), compact, and highly sensitive E-SMS fiber structures can be immobilized to detect with high specificity Anti-BSA at concentrations as low as 100 ng/ml, which makes it very promising and potentially suitable for sensing in biomedical applications such as the bio-molecular detection of species such as Mycobacterium tuberculosis.

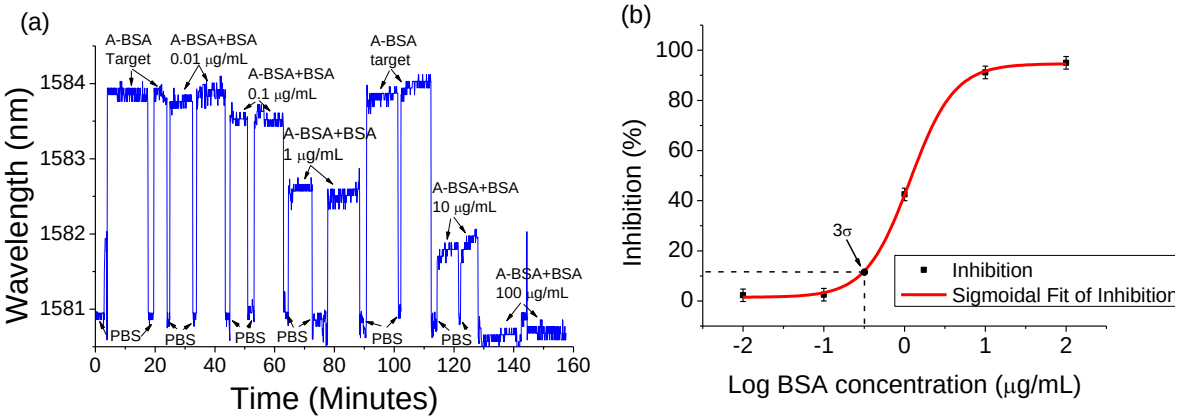

Figure 5-4: (a) Temporal response of the E-SMS biosensor during the competitive assay. (b) Percentage of inhibition against concentration of BSA.

The results that have been achieved are pleasantly encouraging, validating that the biosensing structures based on E-SMS fiber are some of the simplest, selective, reliable and cost-effective alternatives for detecting biological species at low concentrations, which makes it very promising and potentially suitable for sensing in biomedical applications such as the bio-molecular detection of species such as Mycobacterium tuberculosis. These

biosensors offer high potential for the development of a simple, reliable, and cost-effective platform system for on-site detection and low concentrations monitoring of biological species. The integration of these sensors into a portable platform is reported in detail in the next chapter of this thesis.

Conversely, the results of the E-SMS structure functionalized for detection of Anti-BSA in gave rise to some contributions reported in the following manuscript submitted to indexed journal of international circulation and presented at an international conference:

Brayan Patiño-Jurado, Yamile Cardona-Maya, Marisol Jaramillo-Grajales, Yeison Montagut-Ferizzola, and Juan F. Botero-Cadavid. “A Label-free Biosensor Based on E-SMS Optical Fiber Structure for Anti BSA Detection.” Optical Fiber Technology, 2022.

Brayan Patiño-Jurado, Camilo Buriticá Restrepo, Yamile Cardona-Maya, Yeison Montagut-Ferizzola, Robinson Torres, Marisol Jaramillo-Grajales, Rodrigo Acuña-Herrera, Petro Torres, and Juan F. Botero-Cadavid. “Biosensor based on E-SMS Optical Fiber Structure for Detection of Anti BSA.” Optical Sensors and Sensing Congress. Optica Publishing Group, 2021.

5.4 References for Chapter 5

[1] X. Li *et al.*, “A review of specialty fiber biosensors based on interferometer configuration,” *J. Biophotonics*, vol. 14, no. 6, p. e202100068, Jun. 2021, doi: 10.1002/JBIO.202100068.

[2] H. E. Joe, H. Yun, S. H. Jo, M. B. G. Jun, and B. K. Min, “A review on optical fiber sensors for environmental monitoring,” *International Journal of Precision Engineering and Manufacturing - Green Technology*. 2018, doi: 10.1007/s40684-018-0017-6.

[3] P. Lu *et al.*, “Distributed optical fiber sensing: Review and perspective,” *Applied Physics Reviews*, vol. 6, no. 4. American Institute of Physics Inc., Dec. 01, 2019, doi: 10.1063/1.5113955.

[4] N. De Acha, A. B. Socorro-Leránoz, C. Elosúa, and I. R. Matías, “Trends in the Design of Intensity-Based Optical Fiber Biosensors (2010–2020),” *Biosens. 2021, Vol. 11, Page 197*, vol. 11, no. 6, p. 197, Jun. 2021, doi: 10.3390/BIOS11060197.

[5] S. E. Mowbray and A. M. Amiri, “A Brief Overview of Medical Fiber Optic Biosensors and Techniques in the Modification for Enhanced Sensing Ability,” *Diagnostics 2019, Vol. 9, Page 23*, vol. 9, no. 1, p. 23, Feb. 2019, doi: 10.3390/DIAGNOSTICS9010023.

[6] Y. E. Monfared, “Overview of Recent Advances in the Design of Plasmonic Fiber-Optic Biosensors,” *Biosens. 2020, Vol. 10, Page 77*, vol. 10, no. 7, p. 77, Jul. 2020, doi: 10.3390/BIOS10070077.

[7] L. Wu, G. Li, X. Xu, L. Zhu, R. Huang, and X. Chen, “Application of nano-ELISA in food analysis: Recent advances and challenges,” *TrAC Trends Anal. Chem.*, vol. 113, pp. 140–156, Apr. 2019, doi: 10.1016/J.TRAC.2019.02.002.

[8] M. S. Tabatabaei, R. Islam, and M. Ahmed, “Applications of gold nanoparticles in ELISA, PCR, and immuno-PCR assays: A review,” *Anal. Chim. Acta*, vol. 1143, pp. 250–266, Jan. 2021, doi: 10.1016/J.ACA.2020.08.030.

[9] C. chen Li, Z. yue Wang, L. juan Wang, and C. yang Zhang, “Biosensors for epigenetic biomarkers detection: A review,” *Biosens. Bioelectron.*, vol. 144, p. 111695, Nov. 2019, doi: 10.1016/J.BIOS.2019.111695.

[10] N. A. binte M. Salleh, Y. Tanaka, L. Sutarlie, and X. Su, “Detecting bacterial infections in wounds: a review of biosensors and wearable sensors in comparison with conventional laboratory methods,” *Analyst*, 2022, doi: 10.1039/D2AN00157H.

[11] M. F. Petrucelli *et al.*, “Epidemiology and Diagnostic Perspectives of Dermatophytoses,” *J. Fungi 2020, Vol. 6, Page 310*, vol. 6, no. 4, p. 310, Nov. 2020, doi: 10.3390/JOF6040310.

[12] B. Pérez-López and M. Mir, “Commercialized diagnostic technologies to combat SARS-CoV2: Advantages and disadvantages,” *Talanta*, vol. 225, p. 121898, Apr. 2021, doi: 10.1016/J.TALANTA.2020.121898.

[13] L. Gorski, “Serotype Assignment by Sero-agglutination, ELISA, and PCR,” *Methods Mol. Biol.*, vol. 2220, pp. 57–78, 2021, doi: 10.1007/978-1-0716-0982-8_5.

[14] C. Chen and J. Wang, “Optical biosensors: An exhaustive and comprehensive review,” *Analyst*. 2020, doi: 10.1039/c9an01998g.

[15] S. Menon, M. R. Mathew, S. Sam, K. Keerthi, and K. G. Kumar, “Recent advances and challenges in electrochemical biosensors for emerging and re-emerging infectious diseases,” *J. Electroanal. Chem.*, vol. 878, p. 114596, Dec. 2020, doi: 10.1016/J.JELECHEM.2020.114596.

[16] H. Shaikh and S. Shah, “Thermal biosensors for virus detection,” *Biosens. Virus Detect.*, Dec. 2021, doi: 10.1088/978-0-7503-3867-7CH6.

[17] M. A. Farag, M. Tanios, S. AlKarimy, H. Ibrahim, and H. A. Guirguis, “Biosensing approaches to detect potential milk contaminants: a comprehensive review,” *https://doi.org/10.1080/19440049.2021.1914864*, vol. 38, no. 7, pp. 1169–1192, 2021, doi: 10.1080/19440049.2021.1914864.

[18] M. Pohanka, “Overview of Piezoelectric Biosensors, Immunosensors and DNA Sensors and Their Applications,” *Mater. 2018, Vol. 11, Page 448*, vol. 11, no. 3, p. 448, Mar. 2018, doi: 10.3390/MA11030448.

[19] V. Nabaei, R. Chandrawati, and H. Heidari, “Magnetic biosensors: Modelling and simulation,” *Biosens. Bioelectron.*, vol. 103, pp. 69–86, Apr. 2018, doi:

10.1016/J.BIOS.2017.12.023.

[20] A. Haleem, M. Javaid, R. P. Singh, R. Suman, and S. Rab, “Biosensors applications in medical field: A brief review,” *Sensors Int.*, vol. 2, p. 100100, Jan. 2021, doi: 10.1016/J.SINTL.2021.100100.

[21] N. L. Kazanskiy, S. N. Khonina, M. A. Butt, A. Kaźmierczak, and R. Piramidowicz, “State-of-the-Art Optical Devices for Biomedical Sensing Applications—A Review,” *Electron. 2021, Vol. 10, Page 973*, vol. 10, no. 8, p. 973, Apr. 2021, doi: 10.3390/ELECTRONICS10080973.

[22] D. Lo Presti *et al.*, “Fiber bragg gratings for medical applications and future challenges: A review,” *IEEE Access*, vol. 8, pp. 156863–156888, 2020, doi: 10.1109/ACCESS.2020.3019138.

[23] M. A. Riza, Y. I. Go, S. W. Harun, and R. R. J. Maier, “FBG Sensors for Environmental and Biochemical Applications - A Review,” *IEEE Sens. J.*, vol. 20, no. 14, pp. 7614–7627, Jul. 2020, doi: 10.1109/JSEN.2020.2982446.

[24] P. Salvo *et al.*, “Biosensors for Detecting Lymphocytes and Immunoglobulins,” *Biosens. 2020, Vol. 10, Page 155*, vol. 10, no. 11, p. 155, Oct. 2020, doi: 10.3390/BIOS10110155.

[25] Y. Zhao, R. jie Tong, F. Xia, and Y. Peng, “Current status of optical fiber biosensor based on surface plasmon resonance,” *Biosens. Bioelectron.*, vol. 142, p. 111505, Oct. 2019, doi: 10.1016/J.BIOS.2019.111505.

[26] J. Zhou *et al.*, “Surface plasmon resonance (SPR) biosensors for food allergen detection in food matrices,” *Biosens. Bioelectron.*, vol. 142, p. 111449, Oct. 2019, doi: 10.1016/J.BIOS.2019.111449.

[27] A. Jebelli, F. Oroojalian, F. Fathi, A. Mokhtarzadeh, and M. de la Guardia, “Recent advances in surface plasmon resonance biosensors for microRNAs detection,” *Biosens. Bioelectron.*, vol. 169, p. 112599, Dec. 2020, doi: 10.1016/J.BIOS.2020.112599.

[28] Y. Cardona-Maya, A. B. Socorro, I. Del Villar, J. L. Cruz, J. M. Corres, and J. F. Botero-Cadavid, “Label-free wavelength and phase detection based SMS fiber immunosensors optimized with cladding etching,” *Sensors Actuators B Chem.*, vol. 265, pp. 10–19, Jul. 2018, doi: 10.1016/J.SNB.2018.03.002.

[29] N. P. Mauranyapin, L. Booth, I. Marinkovic, and W. P. Bowen, “Interferometric Biosensing,” *Single Mol. Sens. Beyond Fluoresc.*, pp. 5–36, 2022, doi: 10.1007/978-3-030-90339-8_1.

[30] A. G. Burenin *et al.*, “Direct immunosensing by spectral correlation interferometry: assay characteristics versus antibody immobilization chemistry,” *Anal. Bioanal. Chem. 2015 40714*, vol. 407, no. 14, pp. 3955–3964, Mar. 2015, doi: 10.1007/S00216-015-8600-Y.

[31] Y. Chen, J. Liu, Z. Yang, J. S. Wilkinson, and X. Zhou, “Optical biosensors based on refractometric sensing schemes: A review,” *Biosens. Bioelectron.*, vol. 144, p.

111693, Nov. 2019, doi: 10.1016/J.BIOS.2019.111693.

[32] F. Esposito, A. Srivastava, L. Sansone, M. Giordano, S. Campopiano, and A. Iadicicco, “Label-Free Biosensors Based on Long Period Fiber Gratings: A Review,” *IEEE Sens. J.*, vol. 21, no. 11, pp. 12692–12705, Jun. 2021, doi: 10.1109/JSEN.2020.3025488.

[33] S. M. Tariq, M. A. Fakhri, and U. Hashim, “Fiber Optics for Sensing Applications in a Review,” *Key Eng. Mater.*, vol. 911, pp. 65–76, Feb. 2022, doi: 10.4028/P-K239BA.

[34] K. Takahashi, R. Ozawa, M. Ishida, and K. Sawada, “Estimation of diaphragm deformation induced by molecuar adsorption on mems optical interferometric biosensor,” *Int. Conf. Opt. MEMS Nanophotonics*, pp. 5–6, Oct. 2014, doi: 10.1109/OMN.2014.6924511.

[35] Y. Shi, Z. Yu, M. Chen, and T. Lang, “Bovine serum albumin detection using side-hole fiber sensors,” *Opt. Fiber Technol.*, vol. 65, p. 102596, Sep. 2021, doi: 10.1016/J.YOFTE.2021.102596.

[36] X. Z. Wang and Q. Wang, “A High-Birefringence Microfiber Sagnac-Interferometer Biosensor Based on the Vernier Effect,” *Sensors 2018, Vol. 18, Page 4114*, vol. 18, no. 12, p. 4114, Nov. 2018, doi: 10.3390/S18124114.

[37] K. Wang *et al.*, “Advances in Optical Fiber Sensors Based on Multimode Interference (MMI): A Review,” *IEEE Sens. J.*, vol. 21, no. 1, pp. 132–142, Jan. 2021, doi: 10.1109/JSEN.2020.3015086.

[38] Q. Wu *et al.*, “Singlemode-Multimode-Singlemode Fiber Structures for Sensing Applications-A Review,” *IEEE Sens. J.*, vol. 21, no. 11, pp. 12734–12751, Jun. 2021, doi: 10.1109/JSEN.2020.3039912.

[39] A. Jahanban-Esfahlan, A. Ostadrahimi, R. Jahanban-Esfahlan, L. Roufegarinejad, M. Tabibiazar, and R. Amarowicz, “Recent developments in the detection of bovine serum albumin,” *Int. J. Biol. Macromol.*, vol. 138, pp. 602–617, Oct. 2019, doi: 10.1016/J.IJBIOMAC.2019.07.096.

[40] N. Ul Amin, H. M. Siddiqi, Y. K. Lin, Z. Hussain, and N. Majeed, “Bovine Serum Albumin Protein-Based Liquid Crystal Biosensors for Optical Detection of Toxic Heavy Metals in Water,” *Sensors 2020, Vol. 20, Page 298*, vol. 20, no. 1, p. 298, Jan. 2020, doi: 10.3390/S20010298.

[41] A. Jahanban-Esfahlan, L. Roufegarinejad, R. Jahanban-Esfahlan, M. Tabibiazar, and R. Amarowicz, “Latest developments in the detection and separation of bovine serum albumin using molecularly imprinted polymers,” *Talanta*, vol. 207, p. 120317, Jan. 2020, doi: 10.1016/J.TALANTA.2019.120317.

[42] T. Nagel *et al.*, “Direct detection of tuberculosis infection in blood serum using three optical label-free approaches,” *Sensors Actuators B Chem.*, vol. 129, no. 2, pp. 934–940, Feb. 2008, doi: 10.1016/J.SNB.2007.10.009.

[43] Y. Zhang, X. Tian, L. Xue, Q. Zhang, L. Yang, and B. Zhu, “Super-high sensitivity of fiber temperature sensor based on leaky-mode bent SMS structure,” *IEEE*

Photonics Technol. Lett., vol. 25, no. 6, pp. 560–563, 2013, doi: 10.1109/LPT.2013.2245644.

[44] F. Chiavaioli, C. A. J. Gouveia, P. A. S. Jorge, and F. Baldini, “Towards a Uniform Metrological Assessment of Grating-Based Optical Fiber Sensors: From Refractometers to Biosensors,” *Biosens. 2017, Vol. 7, Page 23*, vol. 7, no. 2, p. 23, Jun. 2017, doi: 10.3390/BIOS7020023.

[45] K. E. Sapsford *et al.*, “Indirect competitive immunoassay for detection of aflatoxin B1 in corn and nut products using the array biosensor,” *Biosens. Bioelectron.*, vol. 21, no. 12, pp. 2298–2305, Jun. 2006, doi: 10.1016/J.BIOS.2005.10.021.

[46] Y. E. Marin *et al.*, “Silicon-photonic interferometric biosensor using active phase demodulation,” *https://doi.org/10.1117/12.2287803*, vol. 10510, pp. 20–28, Feb. 2018, doi: 10.1117/12.2287803.

[47] G. Sancho-Fornes, M. Avella-Oliver, J. Carrascosa, R. Puchades, and Á. Maquieira, “Interferometric multilayered nanomaterials for imaging unlabeled biorecognition events,” *Sensors Actuators B Chem.*, vol. 331, p. 129289, Mar. 2021, doi: 10.1016/J.SNB.2020.129289.

6. Fiber Optics Sensing Platform for Low-Concentration Monitoring of Biological and Chemical Species

6.1 Introduction and Background

The problem of detecting and monitoring contamination levels with toxic heavy metal ions, such as the mercury, in water is no different to the problem of rapid detection and monitoring of infectious diseases such as tuberculosis. Portable, specific, sensitive, and cost-effective technology for the rapid detection of substances with low concentration is required to address these health problems which particularly affect vulnerable populations in remote regions [1], [2]. In response to this problem, a wide range of approaches have been reported in the literature for detecting chemical and biological substances, including electrochemical sensing platforms [3], microchip electrophoresis [4], portable mass spectrometers [5], handheld Raman [6]–[8], smartphones [9]–[11], and near infrared spectrometer (NIR) instruments [12], as well as and point-of-need devices [13]–[15], like paper-based platforms for in-field analysis of substances [16], [17]. The mentioned examples have successfully demonstrated the huge potential of portable devices for on-site applications.

Regarding the optical fiber sensing platforms, there are not too many of these devices reported in the literature, in contrast with the large amount of scientific papers on optical fiber sensors for measuring chemical and biological species that are published almost on a daily bases on all types of journals of wide international circulation [18], [19]. It means that there is a vast opportunity for the development of scientific and technological research related to the effective implementation and on-site deployment of sensors based on fiber optics for chemical, biomedical and biochemical measurements. Some prototypes that are more related to the fiber optics sensing platform proposed in this thesis including fiber optics sensing platform based on Raman spectroscopy [20], carbon quantum dots [21], Bragg

gratings [22], fluorescence [23], interferometers [24], [25], surface plasmons [26], lossy mode resonance [27], and evanescent field systems [28], [29] .

Most of these fiber sensing platforms, however, require sophisticated instrumentation for their fabrication and implementation, or are limited in selectivity, sensitivity, compactness, and rapidness, which might be challenging for field implementation in remote regions [30]. This is precisely the motivation for this last chapter of this thesis, in which it is reported the design, modeling, fabrication, and implementation of a portable and compact alternative for on-site testing of chemical and biological species. This fiber optics platform alternative was designed striving to ensure compliance of the democratization criteria of the sensing advanced technology such as the high affordability, user-friendliness, robustness, selectivity, sensitivity, rapidness, equipment-free, and available to people in need [31].

The proposed platform is based on a spectrophotometer with a working spectrum in the visible range that integrates an E-SMS fiber sensor. This cost-effective and practical sensor was selected instead of the sensor based on slanted end, mainly because of the difficulty of controlling the optical power of the coupled high power 670 nm LED and for its best features of sensitivity, repeatability, and smaller transmission losses; without implying that, the other selective sensor cannot be implemented in the sensing platform if a low-noise current and temperature control unit is incorporated. Thereon, several spectrophotometers can be found in the literature including the versatile color measurement spectrophotometer [32]; ultra violet spectrophotometer [33] and near infrared spectrometer [34], based on CCD detectors (for non-visible ranges of the spectrum) [35], and based on LEDs for the visible spectrum range [36]–[38]. These sensing platforms based on spectrophotometers are generally expensive and complicated, principally due to the sophisticated sensors that are included in them, which limits their portability or accessibility [39], [40]. The cost of these portable devices varies between $500 and $9,000 USD at the time of this research [41]–[43]. Here, however, the integration of a cost-effective (less than $10 USD for materials and manufacturing) selective, simple to fabricate, and easy to implement, functionalized E-SMS sensor can contribute to decrease the cost of the sensing technology based on spectrophotometers.

In response to that opportunity, in this last chapter the design, modeling, fabrication, integration of sensors, and preliminary evaluation of a compact optical fiber sensing platform based on spectrophotometer in the visible range, for detection of chemical and

biological species at low concentrations, is reported in detail. Although to date the studies on the performance of the sensors based on E-SMS structures were performed using an infrared light source, in the proposed device an illumination source in the visible range was chosen to develop a truly cost-effective platform (a high power 670 nm LED is at least 100 times less costly than an infrared superluminescent diode). Since, according to the analysis of Section 3.3.1, the reduction of the wavelength of the illumination source, which implies a linear decrease of the sensitivity, can be compensated with the reduction of the diameter of the MMF section; and the optical elements, such as the diffraction grating, and the detection system are substantially less expensive and more affordable at local stores. In the Table 6-1 a comparison of the cost of available commercial components and the cost-effective of production or adaptation of the systems implemented in the sensing platform is presented.

Table 6-1: Comparation of cost of similar commercial components and the system implemented in the sensing platform.

Commercial component	Implemented component	Cost ratio (Commercial/implemented)
Fiber-Connected IR LED [44]	Fiber-Connected high power 670 nm LED	50
Colorimetric sensor for Hg^{2+} [45]	E-SMS sensor for Hg^{2+}	1
Biosensor for BSA [46]	E-SMS biosensor for BSA	13
IR Monochromator [47]	Visible Monochromator	100
IR detector [48]	Visible detector	5
IR Optics [49]	Visible optics	20
Commercial sensing platform [41]	Proposed sensing platform	30

In the following paragraphs the operating principles of the sensing platform were theoretically and numerically analyzed. Then the design of the functional blocks, the description of the mechanical assembly, the optical mounting, and the electronic modeling were detailed in the second section of the chapter. Finally, the fabrication of the fiber optics sensing platform was reported and evaluated with some test measuring low concentrations of mercury in water and anti-BSA under laboratory conditions.

6.2 Operating Principles and Resolution Review

The sensing platform based on fiber optics described in the present chapter is supported on visible spectrophotometry for optical spectrum analysis. Optical spectrum analysis is the

measurement of optical power as a function of wavelength of the illumination source that illuminates the sample [44]. Figure 6-1 (a) shows the optical spectrum produced by an E-SMS fiber sensor to which a broad-spectrum light source based on a red LED is coupled. The detected illumination profile is not purely monochromatic, but it consists of a continuous power distribution within a limited wavelength domain and with an amplitude profile determined by the characteristics of the coupled illumination source. Applications of the spectrometry for optical analysis include chemical and biological sensing, biometry, and various light level measurements: testing laser and LED light sources for spectral characterization and power distribution, as well as testing transmission characteristics of optical devices [45], [46].

On the operating principle of the spectrophotometer for optical analysis, the Figure 6-1 (b) shows the typical structure of a conventional spectrophotometric device of the type used for food inspection [47], drinking water quality monitoring [48], bioanalysis [49], chemical characterization [50]–[52], and illumination measurements [53]. In that configuration, the incoming light from a broad-spectrum light source illuminates the sample and passes through optical components, including collimation lenses and a diffraction grating, to reach a photodetector system. The photogenerated current creates a voltage signal through an analog circuit, which is then digitized and analyzed using a computer. Despite its simple description, the conventional spectrophotometry system for optical analysis is too bulky for portable and cost-effective applications.

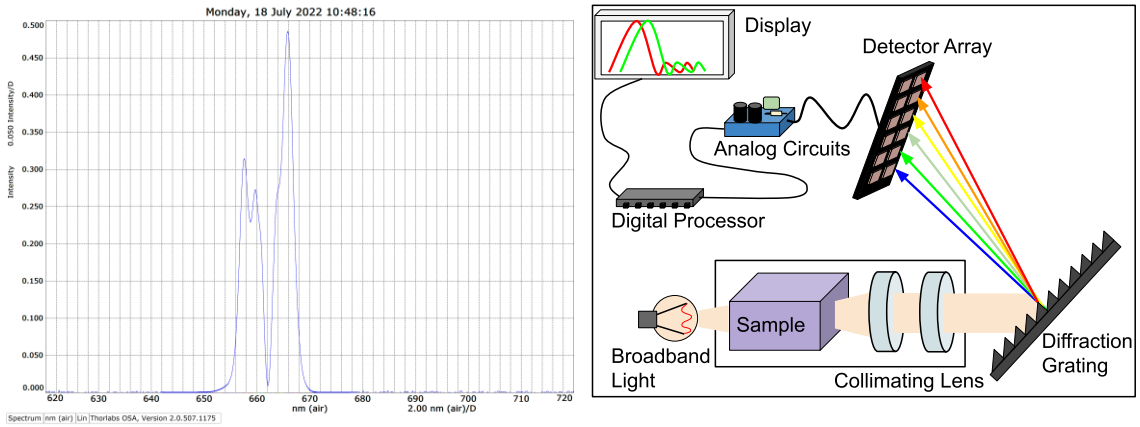

(a) (b)

Figure 6-1: (a) Optical spectrum produced by an illumination source based on a red LED coupled to the E-SMS fiber sensor. (b) Typical structure of a conventional spectrophotometric device.

The spectrophotometers for optical analysis, as the proposed in this thesis, are usually called optical spectrum analyzers (OSA). These can be classified into three main categories: (I) OSA based on diffraction gratings and based on two interferometers [54], [55], (II) the OSA based on Fabry-Perot [56], and (III) based on Michelson interferometers [57]. In terms of resolution, which is defined as the measure of the smallest spatial variation (measured in wavelengths) produced by a small variation of optical power that can be resolved by the photodetector [54]; the optical spectrum analyzers based on diffraction gratins are capable of measuring spectra of lasers and LEDs, with a variable resolution, typically ranging from 0.1 nm to 10 nm [58]. For its part, The OSA based on Fabry-Perot-interferometer have a fixed, narrow resolution, between 0.02 nm and 0.2 nm [59]. Michelson interferometer-based optical spectrum analyzers, which are used for direct coherence length measurements, analyses the optical spectrum by calculating the Fourier transform of the measured interference pattern with resolutions between 0.015 and 0.15 nm [57].

The sensing platform based on optical fiber proposed in this thesis uses a diode laser as illumination source, the E-SMS sensor as sample holder, a diffraction grating as monochromator, a light to frequency sensor as photodetector, and a microcontroller as signal processor; the conceptual image of the compact and portable sensing platform is illustrated in Figure 6-2 (a). Each of these components and their connections, described on the block diagram in Figure 6-2 (b), are explicated in detail in the following section, where, moreover, the resolution capacity of the OSA in the sensing platform is calculated to be up to 0.2 nm.

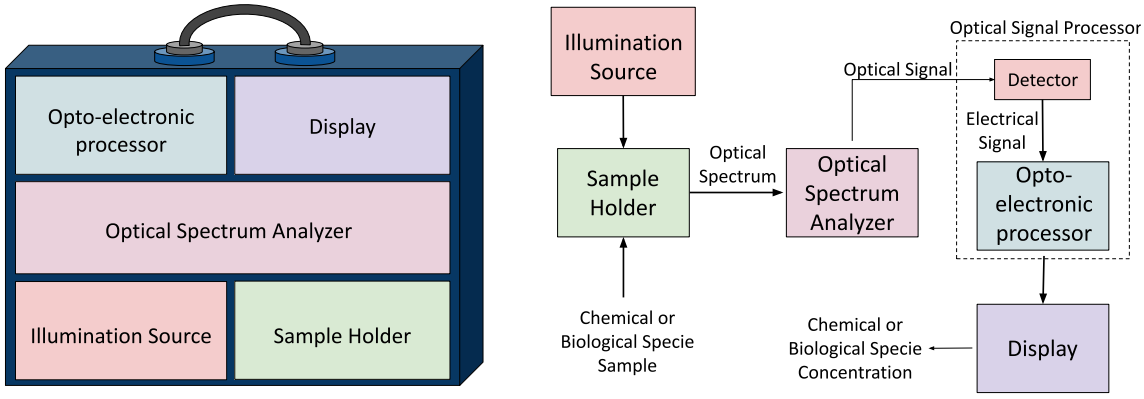

Figure 6-2: (a) Portable and compact sensing platform concept. (b) Block diagram of the sensing platform based on optical fiber for monitoring biological and chemical species.

6.3 Design

Illumination Source.

The light source of the proposed sensing platform is composed of a high power 670 nm LED of 1 W, two 5 degrees light beam collimator lens, and a FC/PC single mode fiber connector, as shown in Figure 6-3 (a). These components are embedded into a cylindrical metal casing with threaded end caps that ensures the proper alignment and position, as shown in Figure 6-3 (b). The lens focuses the light beam on the core at the cleaved end of a singlemode fiber (Thorlabs® SMS 600), which is spliced at the proximal end of the E-SMS fiber sensor. Another piece of single mode fiber is also spliced at the distal end of the E-SMS fiber sensor.

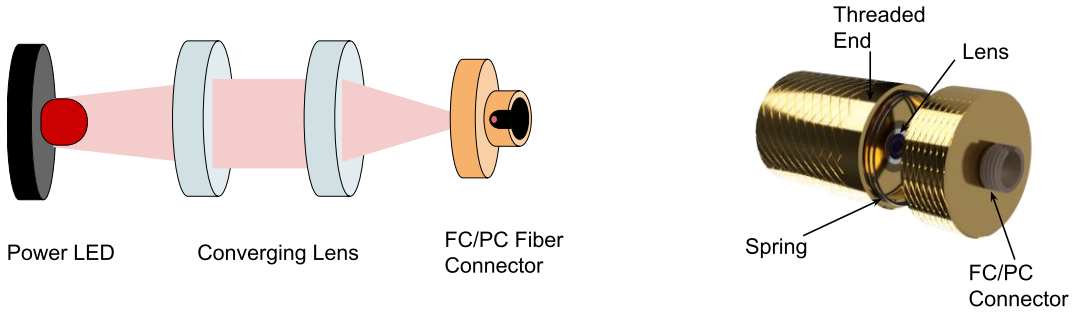

Figure 6-3: (a) Illumination source based on a fiber coupled power LED. (b) Model of the fiber coupled power LED embedded into a cylindrical metal casing with threaded end caps.

Sensor and Sample Holder

E-SMS fiber sensor functionalized for detection of a particular chemical or biological species is integrated to the sensing platform into the sensor module. This module consists in a plastic container with small lateral slits to hold it in place the E-SMS structure and a central cavity which is filled with the sample to analyze, as shown in Figure 6-4 (a). One end of the E-SMS fiber is connected to the illumination source and the other end fiber transmits the light to a fiber with its distal end shaped on a conical geometry, where the light is collimated and focused on a small surface of the diffraction grating. The cone shaped optical fiber at an angle of 15° is used to ensure collimation of the light propagating into the fiber. Since, as indicated above, and as can be verified in [60], the apex angle of a cone-shaped optical fiber controls the numerical aperture, leading to a collimation of the light when that angle is set to 15°, as shown in Figure 6-4 (b).

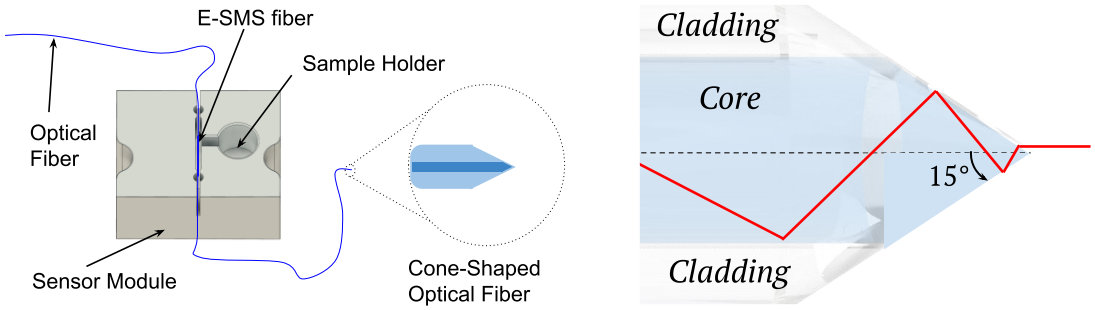

Figure 6-4: (a) Sensor module with the sample holder. (b) Cone shaped optical fiber at the end of the E-SMS fiber sensor collimates the light propagating into the fiber.

Monochromator.

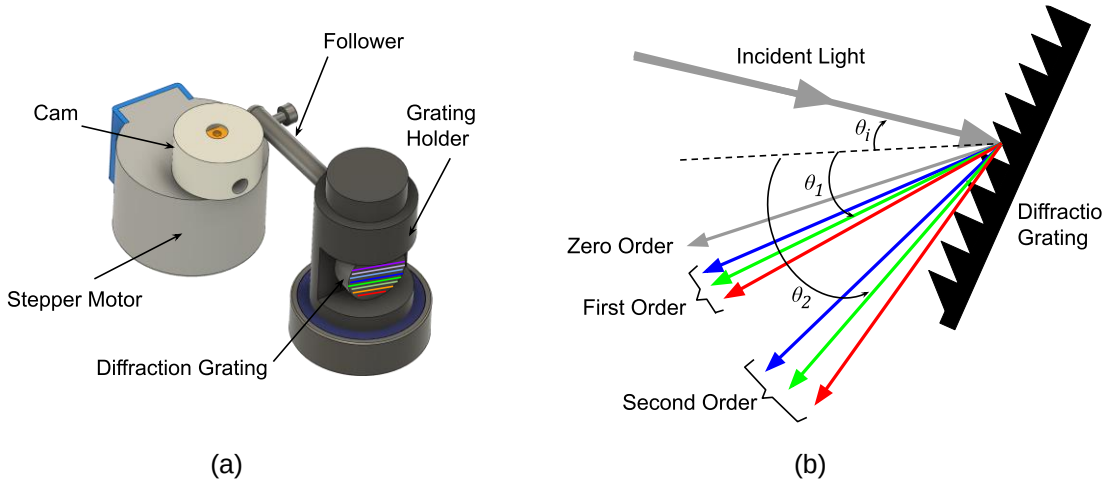

Figure 6-5: (a) Monochromator based on a cam follower mechanism. (b) Principle of the reflective diffraction grating.

The monochromator is composed of a stepper motor with a gearbox, a cam follower, and a diffraction grating obtained from a blank DVD disc, as shown in Figure 6-5 (a). A stepper 28BYJ-48 – 5V with 64 steps per revolution, 5.6° of rotation per step, is used. The stepper motor produces the rotation of the diffraction grating and it is controlled by a microcontroller (MCU) together with an ST Microelectronics® ULN2003 motor driver. Using the cam follower connected to, and driven by, the stepper motor, the new resolution of the rotation of the diffraction grating is about 0.2 degrees per step. The reflective diffraction grating acts as the dispersive element to separate the spectrum in individual wavelengths by cause of the large number of equally spaced parallel slits on its surface, which diffract the incident

light on it allowing to observe an individual wavelength, or color, when the conditions for constructive interference for a given wavelength are satisfied, as shown in Figure 6-5 (b). The reflective diffraction grating used in the sensing platform was built using a small circular portion of a blank DVD (0.72 μm grating spacing, 1351 lines per mm).

The proposed sensing platform works in the in the red wavelength region, with a constant spectral bandwidth of 10 nm. To increase the spectral resolution, the position of the stepper motor was adjusted so that detector can capture the reflected light from the second order produced by the diffraction grating, considering that the smallest resolvable wavelength difference of grating is given by [60]:

$$\Delta\lambda = \frac{\lambda}{mN}, \tag{6.1}$$

where λ is the wavelength of light, *N* is the total number of slits illuminated and *m* is the order of the diffraction. With *N*=1351 lines/mm, λ=633 nm, and *m*=2, the designed monochromator has a selectivity of 0.2 nm per step sweeping all of the 10 nm of the spectrum in 50 steps. In order to detect a specific wavelength, the grating equation can be used [60]:

$$\alpha[sin\theta_i + sin\theta_m] = \lambda m. \tag{6.2}$$

This equation states that a diffraction grating with spacing α will deflect light at discrete angles θ_m, dependent upon the value λ and the order m of principal maxima. For the diffraction grating based on DVD, $\alpha = 740$ nm.

Photodetector.

A light to frequency sensor AMS OSRAM ® TSL235R is used as photodetector, which combines a silicon photodiode and a current-to-frequency converter on a single monolithic CMOS integrated circuit [61]. This semiconductor device converts measurements of light intensity to a digital form for direct interfacing to a microcontroller, as shown in Figure 6-6. The output of this electronic component is a square wave whose frequency is linearly proportional to the light intensity.

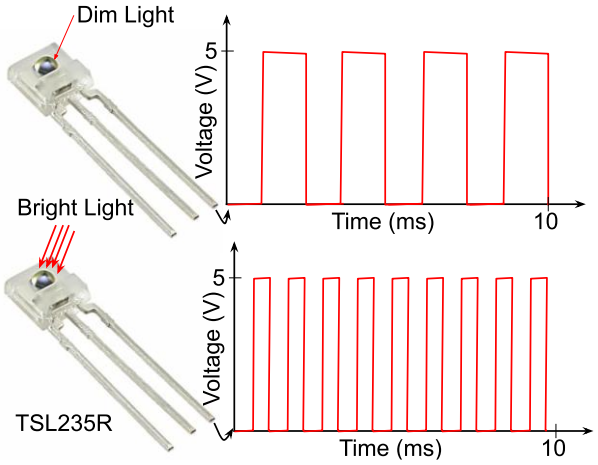

Figure 6-6: Response of the photodetector TSL235R to the intensity of the incident light.

Microcontroller.

A microcontroller Microchip© PIC18F2550 was used as processor of the digital signal generated by the light to frequency sensor and as controller of the motor driver and the display. Digital ports were used for reading the square wave and sending direction signals to the motor driver to sweep the complete spectra in 2 s. The code uses 18% of the memory. The microcontroller was also used to compute the shift of the optical spectrum when the biological or chemical sample was put in contact with the functionalized E-SMS sensor. The shift in wavelength of the optical spectrum is then analyzed as a change in the spatial position, measured by the angular position of the diffraction grating, of the global minimum of frequency.

6.4 Hardware Setup

With the aim of verifying distances and positions of the functional elements that constitute the spectrophotometer of the fiber optics sensing platform, a numerical study in COMSOL Multiphysics® was carried out using the Ray Tracing Module and the optical elements provided by the application, such as mirrors, reflective diffraction grating set up in 1351 lines/mm, and optical power and wavelength detectors, as shown in Figure 6-7 (a). From this simulation analysis it was possible to optimize the dimensions of the mechanical support structure in a compact box of 120 mm x 200 mm x 50 mm, placing the diffraction grating 75 mm from the second mirror, and this to 85 mm from the detectors to ensure the greatest dispersion of the light still under confined dimensions.

Geometrical arrangement of the functional elements was experimentally verified mounting each item on the optical table in the laboratory, by following the disposition indicated by the aforementioned framework of the simulation. For this purpose, a DC voltage source was used to energize the electronic circuits. The microcontroller, the E-SMS fiber sensor, and the detector were incorporated into the experimental setup, as show in Figure 6-7 (b). The diffraction grating was mounted on a manual rotating stage Newport ™ RSP-1T (resolution 0.1 degrees) in order to control the angular position. This experimental setup also resulted in the identification of individual functional modules to be fabricated to get a compact and portable fiber optics sensing platform as illustrated in Figure 6-7 (c).

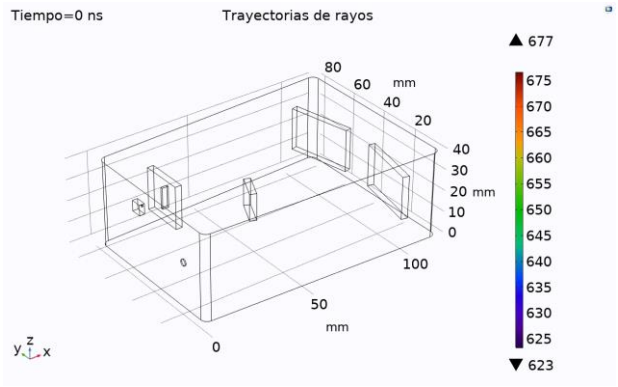

(a)

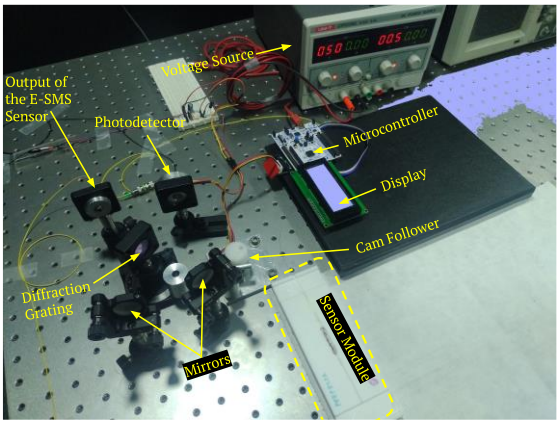

(b)

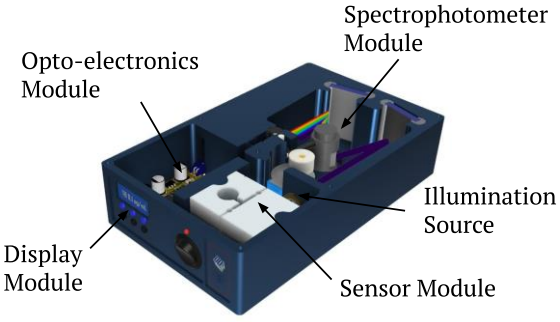

(c)

Figure 6-7: (a) Numerical study in COMSOL Multiphysics® of the designed spectrophotometer. (b) Experimental setup in the laboratory of the fiber optics sensing platform. (c) CAD model of the portable and compact fiber optics sensing platform.

The compact and portable fiber optics sensing platform was assembled after fabricated each individual functional module: Illumination source, sample holder, optical spectrum

analyzer (spectrophotometer), opto-electronics processor, and display. Apart from a more compact sample holder for the E-SMS fiber sensor, only the supports for the mirrors and the grating were redesigned to ensure the appropriated guidance of the optical signal within the portable sensing platform. All other functional modules remained unmodified when they were integrated into the aluminum support structure, which was fabricated using a Haas ® CNC Milling Machine.

6.5 Results and Discussion

The light source based on a high power 670 nm LED of 1 W, two 5 degrees light beam collimator lens, and a FC/PC single mode fiber connector was implemented and tested using a Power Meter EXFO® FPM600, obtaining a measure of up to -15.1 dBm, which is 40% smaller than the typical measurement values in fiber-coupled diode lasers $(\sim -10\ \mathrm{dBm})$, but with intensity enough for sensing purposes. The photograph in Figure 6-8 shows a photograph of the red beam emerging of the fabricated light source based on a fiber-coupled power LED.

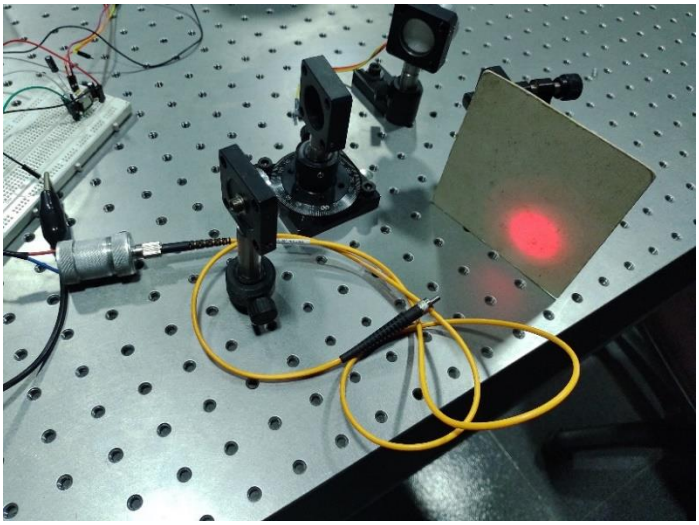

Figure 6-8: Light source based on a fiber-coupled power LED.

With the aim of verifying the ability of the design spectrophotometer to reproduce the optical intensity distribution of a broad-spectrum light source, a stabilized tungsten-halogen source (Thorlabs SLS201L), 360 - 2600 nm, was located in the illumination source module of the sensing platform. The diffraction grating was rotated from -75° to 75 ° with the manual rotating stage and the frequency measured by the photodetector was captured by the microcontroller. The graph of the frequency versus the angle of the grating for this broad-

spectrum source is shown in Figure 6-9. The characteristic spectral power distribution of the source provided by the manufacturer is shown in inset. In direct comparison, the results show an identical intensity distribution in the corresponding spectral region, with the same slope between 550 and 850 nm, which would allow to characterize the angular position of the grating with the wavelength. However, this characterization is not necessary because the aim of the sensing platform is to track the position, anyone whether angular or in wavelength, of the global minimum of the spectrum when the concentration of the sample is modified.

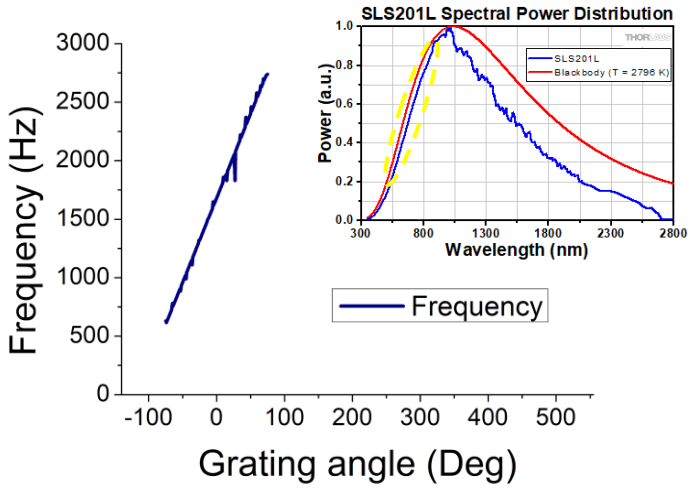

Figure 6-9: Frequency versus the grating angle for the broad-spectrum stabilized tungsten-halogen source. Inset: Characteristic spectral power distribution taken from [63] pointing out with a yellow oval the corresponding spectral region.

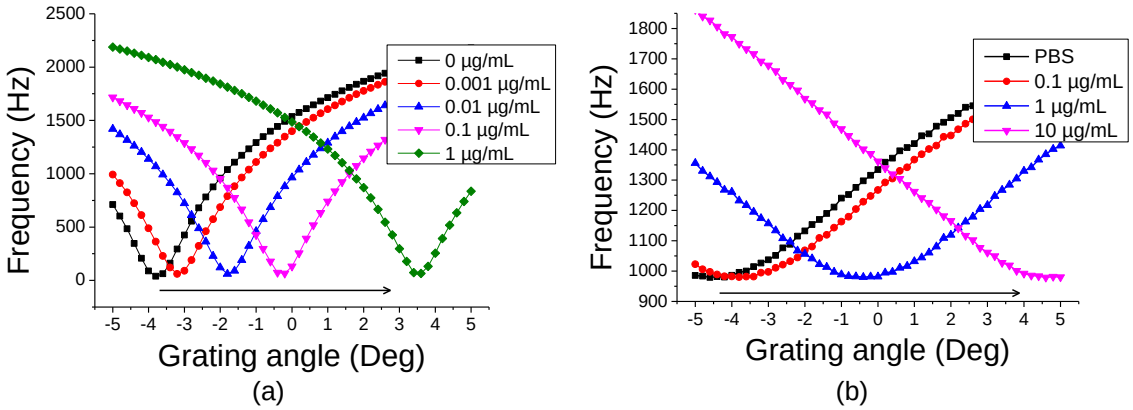

Figure 6-10: Spectrum response of the functionalized E-SMS sensors for different concentrations of (a) mercury in water and (b) Anti-BSA.

The E-SMS fiber sensors were subsequently connected to the illumination source module to experimentally evaluate the ability of the fiber optics sensing platform to detect the

changes of the concentration of Hg^{2+} ions in water and Anti-BSA in PBS in the sensing surface of the functionalized sensors as described in chapters 4 and 5. The Figure 6-10 (a) and (b) show correspondingly the spectrum response for the E-SMS structures to the different concentrations of Hg^{2+} in water, from 0 to 0.001 to 1 µg/mL, and concentrations of Anti-BSA between 0 to 10 µg/mL. As expected, a shift in the angular position of the global minimum is clearly observed due to concentration change of the chemical and the biological specie in the sensing surface of both E-SMS sensors. These results show that the fiber optics sensing platform can monitor chemical interactions up to a minimum of 0.001 µg/mL (one part per billion) of Hg^{2+} in water and 0.1 µg/mL of Anti-BSA, proving to be very promising, rapid, sensitive, and potentially suitable cost-effective sensing technology for detection of chemical and biological species at low concentrations.

The results obtained with the fiber optics sensing platform mounted on the optical tabletop, validated the geometrical arrangement, the optimal sizes, the functional characteristics, and the applicability limits of the different functional modules of the designed compact platform. All of these modules were integrated into the aluminum support structure especially built for this purpose. In order to achieve a portable device, a lithium-ion battery was incorporated as DC voltage source for energizing the electronic circuits that control the illumination source, the photodetector, the digital processor, and the display. The photograph of the fabricated compact and portable fiber optics sensing platform is shown in Figure 6-11. More information on the final adjustments, operation principle, and definitive results, are not provided in this thesis because it forms part of the undisclosed information, in the patent application that led the sensing platform developed in this research:

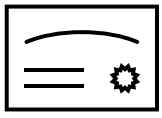

Universidad Nacional de Colombia y Universidad EIA. Patiño-Jurado, Brayan; Cardona-Maya, Yamile; Montagut-Ferizzola, Yeison; Botero-Cadavid, Juan F. Garcia-Sucerquia, Jorge “Dispositivo de sensado basado en interferometría de fibra Óptica.”

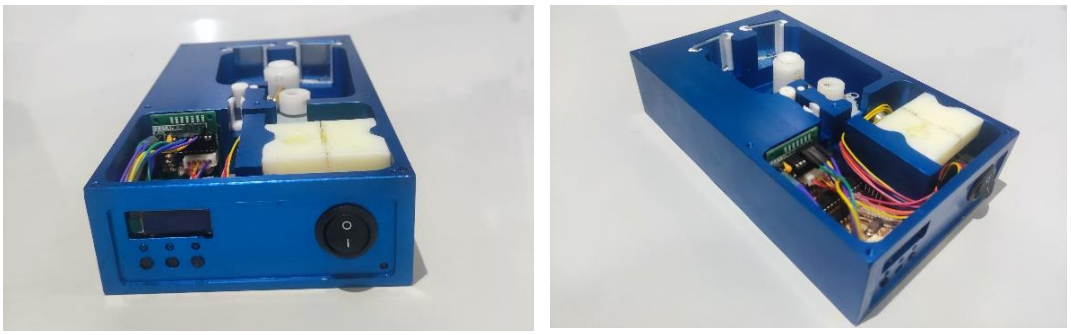

Figure 6-11: Photographs of the Fiber optics sensing platform for monitoring biological and chemical species at low-concentrations.

6.6 References for Chapter 6

[1] S. Kumari, Amit, R. Jamwal, N. Mishra, and D. K. Singh, “Recent developments in environmental mercury bioremediation and its toxicity: A review,” *Environ. Nanotechnology, Monit. Manag.*, vol. 13, p. 100283, May 2020, doi: 10.1016/J.ENMM.2020.100283.

[2] C. Maphanga, S. Manoto, S. Ombinda-Lemboumba, L. Hlekelele, and P. Mthunzi-Kufa, “Optical biosensing of mycobacterium tuberculosis for point-of-care diagnosis,” vol. 11251, p. 112510R, Feb. 2020, doi: 10.1117/12.2545842.

[3] A. Fethi, “Novel materials for electrochemical sensing platforms,” *Sensors Int.*, vol. 1, p. 100035, Jan. 2020, doi: 10.1016/J.SINTL.2020.100035.

[4] N. Nuchtavorn, W. Suntornsuk, S. M. Lunte, and L. Suntornsuk, “Recent applications of microchip electrophoresis to biomedical analysis,” *J. Pharm. Biomed. Anal.*, vol. 113, pp. 72–96, Sep. 2015, doi: 10.1016/J.JPBA.2015.03.002.

[5] B. Jiao *et al.*, “Handheld Mass Spectrometer with Intelligent Adaptability for On-Site and Point-of-Care Analysis,” *Anal. Chem.*, vol. 93, no. 47, pp. 15607–15616, Nov. 2021, doi: 10.1021/ACS.ANALCHEM.1C02508/SUPPL_FILE/AC1C02508_SI_001.PDF.

[6] J. Huehnerhoff, J. A. Lozo, E. R. Deutsch, and A. R. Hajian, “High resolution handheld Raman and reflectance hyperspectral imaging for remote sensing and threat detection,” *https://doi.org/10.1117/12.2304374*, vol. 10657, p. 21, May 2018, doi: 10.1117/12.2304374.

[7] P. G. Wilcox and J. A. Guicheteau, “Comparison of handheld Raman sensors through opaque containers,” *https://doi.org/10.1117/12.2303968*, vol. 10629, pp. 64–69, May 2018, doi: 10.1117/12.2303968.

[8] P. Vargas Jentzsch, F. Gualpa, L. A. Ramos, and V. Ciobotă, “Adulteration of clove essential oil: Detection using a handheld Raman spectrometer,” *Flavour Fragr. J.*, vol. 33, no. 2, pp. 184–190, Mar. 2018, doi: 10.1002/FFJ.3438.

[9] Y. Fan, J. Li, Y. Guo, L. Xie, and G. Zhang, “Digital image colorimetry on smartphone for chemical analysis: A review,” *Measurement*, vol. 171, p. 108829, Feb. 2021, doi: 10.1016/J.MEASUREMENT.2020.108829.

[10] K. Shrivas *et al.*, “Smartphone coupled with paper-based chemical sensor for on-site determination of iron(III) in environmental and biological samples,” *Anal. Bioanal. Chem. 2020 4127*, vol. 412, no. 7, pp. 1573–1583, Jan. 2020, doi: 10.1007/S00216-019-02385-X.

[11] S. C. Kishore *et al.*, “Smartphone-Operated Wireless Chemical Sensors: A Review,” *Chemosens. 2022, Vol. 10, Page 55*, vol. 10, no. 2, p. 55, Jan. 2022, doi: 10.3390/CHEMOSENSORS10020055.

[12] K. B. Beć, J. Grabska, and C. W. Huck, “Principles and Applications of Miniaturized Near-Infrared (NIR) Spectrometers,” *Chem. – A Eur. J.*, vol. 27, no. 5, pp. 1514–1532, Jan. 2021, doi: 10.1002/CHEM.202002838.

[13] F. Weihs, A. Anderson, S. Trowell, and K. Caron, “Resonance Energy Transfer-Based Biosensors for Point-of-Need Diagnosis—Progress and Perspectives,” *Sensors 2021, Vol. 21, Page 660*, vol. 21, no. 2, p. 660, Jan. 2021, doi: 10.3390/S21020660.

[14] M. J. Aernecke, K. P. Schultze, K. H. Blakeman, S. E. Miller, and C. D. Brown, “Enabling point-of-need chemical detection by miniaturizing ion-trap mass spectrometry,” *Sensors and Actuators Reports*, vol. 4, p. 100076, Nov. 2022, doi: 10.1016/J.SNR.2022.100076.

[15] S. Jafari *et al.*, “ASSURED Point-of-Need Food Safety Screening: A Critical Assessment of Portable Food Analyzers,” *Foods 2021, Vol. 10, Page 1399*, vol. 10, no. 6, p. 1399, Jun. 2021, doi: 10.3390/FOODS10061399.

[16] S. Cinti, D. Moscone, and F. Arduini, “Preparation of paper-based devices for reagentless electrochemical (bio)sensor strips,” *Nat. Protoc. 2019 148*, vol. 14, no. 8, pp. 2437–2451, Jul. 2019, doi: 10.1038/s41596-019-0186-y.

[17] L. R. Sousa, L. C. Duarte, and W. K. T. Coltro, “Instrument-free fabrication of microfluidic paper-based analytical devices through 3D pen drawing,” *Sensors Actuators B Chem.*, vol. 312, p. 128018, Jun. 2020, doi: 10.1016/J.SNB.2020.128018.

[18] R. Zamith, “Transparency, Interactivity, Diversity, and Information Provenance in Everyday Data Journalism,” *https://doi.org/10.1080/21670811.2018.1554409*, vol. 7, no. 4, pp. 470–489, Apr. 2019, doi: 10.1080/21670811.2018.1554409.

[19] E. Landhuis, “Scientific literature: Information overload,” *Nat. 2016 5357612*, vol. 535, no. 7612, pp. 457–458, Jul. 2016, doi: 10.1038/nj7612-457a.

[20] U. Ullah, Z. Tahir, O. Qazi, S. Mirza, and M. I. Cheema, “Raman Spectroscopy and Machine Learning-based Optical Sensor for Rapid Tuberculosis Diagnosis via Sputum,” Apr. 2022, doi: 10.48550/arxiv.2204.12157.

[21] Y. Cai, J. Zhang, M. Zhang, M. Wang, and Y. Zhao, “The optical fiber sensing

platform for ferric ions detection: A practical application for carbon quantum dots," *Sensors Actuators B Chem.*, vol. 364, p. 131857, Aug. 2022, doi: 10.1016/J.SNB.2022.131857.

[22] Y. F. Zhang, C. Y. Hong, R. Ahmed, and Z. Ahmed, "A fiber Bragg grating based sensing platform fabricated by fused deposition modeling process for plantar pressure measurement," *Measurement*, vol. 112, pp. 74–79, Dec. 2017, doi: 10.1016/J.MEASUREMENT.2017.08.024.

[23] L. Zhao *et al.*, "A luminescent metal–organic framework integrated hydrogel optical fibre as a photoluminescence sensing platform for fluorescence detection," *J. Mater. Chem. C*, vol. 7, no. 4, pp. 897–904, Jan. 2019, doi: 10.1039/C8TC05154B.

[24] G. Wang *et al.*, "Lab-on-fiber sensing system based on responsive Fabry–Perot optical resonance cavities prepared through in situ construction strategy," *Nanotechnology*, vol. 32, no. 41, p. 41LT01, Jul. 2021, doi: 10.1088/1361-6528/AC121D.

[25] L. V. Nguyen, K. Hill, S. Warren-Smith, and T. Monro, "Interferometric-type optical biosensor based on exposed core microstructured optical fiber," *Sensors Actuators B Chem.*, vol. 221, pp. 320–327, Dec. 2015, doi: 10.1016/J.SNB.2015.06.068.

[26] A. Patnaik, J. K. Nayak, K. Senthilnathan, and R. Jha, "Localized plasmon-based optical fiber sensing platform for operation in infrared," *IEEE Photonics Technol. Lett.*, vol. 28, no. 19, pp. 2054–5057, Oct. 2016, doi: 10.1109/LPT.2016.2573287.

[27] P. Zubiate, C. R. Zamarreño, P. Sánchez, I. R. Matias, and F. J. Arregui, "High sensitive and selective C-reactive protein detection by means of lossy mode resonance based optical fiber devices," *Biosens. Bioelectron.*, vol. 93, pp. 176–181, Jul. 2017, doi: 10.1016/J.BIOS.2016.09.020.

[28] Y. Wang, B. Tan, S. Liu, T. Tian, G. Xu, and B. Cai, "An optical fiber-waveguide-fiber platform for ppt level evanescent field-based sensing," *Sensors Actuators B Chem.*, vol. 306, p. 127548, Mar. 2020, doi: 10.1016/J.SNB.2019.127548.

[29] L. V. Nguyen, S. C. Warren-Smith, and K. Hill, "Optical biosensor using an exposed core microstructured optical fiber," *IFMBE Proc.*, vol. 63, pp. 481–485, 2018, doi: 10.1007/978-981-10-4361-1_81/COVER/.

[30] J. W. Lim, T. Y. Kim, and M. A. Woo, "Trends in sensor development toward next-generation point-of-care testing for mercury," *Biosens. Bioelectron.*, vol. 183, p. 113228, Jul. 2021, doi: 10.1016/J.BIOS.2021.113228.

[31] S. Nayak, N. R. Blumenfeld, T. Laksanasopin, and S. K. Sia, "Point-of-Care Diagnostics: Recent Developments in a Connected Age," *Anal. Chem.*, vol. 89, no. 1, pp. 102–123, Jan. 2017, doi: 10.1021/ACS.ANALCHEM.6B04630/ASSET/IMAGES/ACS.ANALCHEM.6B04630.SOCIAL.JPEG_V03.

[32] Y.-T. Tai, C.-Y. Cheng, Y.-S. Chen, and F.-H. Ko, "A hydrogel-based chemosensor applied in conjunction with a Griess assay for real-time colorimetric detection of nitrite in the environment," *Sensors Actuators B Chem.*, vol. 369, p. 132298, Oct.

2022, doi: 10.1016/J.SNB.2022.132298.

[33] D. González-Morales, A. Valencia, A. Díaz-Nuñez, M. Fuentes-Estrada, O. López-Santos, and O. García-Beltrán, “Development of a Low-Cost UV-Vis Spectrophotometer and Its Application for the Detection of Mercuric Ions Assisted by Chemosensors,” *Sensors (Basel).*, vol. 20, no. 3, Feb. 2020, doi: 10.3390/S20030906.

[34] V. Cortés, J. Blasco, N. Aleixos, S. Cubero, and P. Talens, “Monitoring strategies for quality control of agricultural products using visible and near-infrared spectroscopy: A review,” *Trends Food Sci. Technol.*, vol. 85, pp. 138–148, Mar. 2019, doi: 10.1016/J.TIFS.2019.01.015.

[35] M. Nehir, C. Frank, S. Aßmann, and E. P. Achterberg, “Improving Optical Measurements: Non-Linearity Compensation of Compact Charge-Coupled Device (CCD) Spectrometers,” *Sensors 2019, Vol. 19, Page 2833*, vol. 19, no. 12, p. 2833, Jun. 2019, doi: 10.3390/S19122833.

[36] K. Laganovska *et al.*, “Portable low-cost open-source wireless spectrophotometer for fast and reliable measurements,” *HardwareX*, vol. 7, p. e00108, Apr. 2020, doi: 10.1016/J.OHX.2020.E00108.

[37] B. H. Al-Sabbagh and N. N. Abdulrazzaq, “Measuring Dyes Concentration Using a Low-Cost Visible-Light Spectrophotometer,” *Iraqi J. Chem. Pet. Eng.*, vol. 23, no. 2, pp. 27–33, Jun. 2022, doi: 10.31699/IJCPE.2022.2.4.

[38] A. B. D. Nandiyanto, R. Zaen, R. Oktiani, A. G. Abdullah, and L. S. Riza, “A Simple, Rapid Analysis, Portable, Low-cost, and Arduino-based Spectrophotometer with White LED as a Light Source for Analyzing Solution Concentration,” *TELKOMNIKA (Telecommunication Comput. Electron. Control.*, vol. 16, no. 2, pp. 580–585, Apr. 2018, doi: 10.12928/TELKOMNIKA.V16I2.7159.

[39] A. Łoś and A. Strachecka, “Fast and Cost-Effective Biochemical Spectrophotometric Analysis of Solution of Insect ‘Blood’ and Body Surface Elution,” *Sensors 2018, Vol. 18, Page 1494*, vol. 18, no. 5, p. 1494, May 2018, doi: 10.3390/S18051494.

[40] S. Khan, D. Newport, and S. Le Calvé, “Gas Detection Using Portable Deep-UV Absorption Spectrophotometry: A Review,” *Sensors 2019, Vol. 19, Page 5210*, vol. 19, no. 23, p. 5210, Nov. 2019, doi: 10.3390/S19235210.

[41] A. M. Noor, A. N. Norali, Z. Zakaria, C. Y. Fook, and B. N. Cahyadi, “An Open-Source, Miniature UV to NIR Spectrophotometer for Measuring the Transmittance of Liquid Materials,” *Lect. Notes Electr. Eng.*, vol. 842, pp. 407–416, 2022, doi: 10.1007/978-981-16-8690-0_37/COVER/.

[42] J. E. Thompson, “Low-Cost Microplate Reader with 3D Printed Parts for under 500 USD,” *Sensors 2022, Vol. 22, Page 3242*, vol. 22, no. 9, p. 3242, Apr. 2022, doi: 10.3390/S22093242.

[43] B. Wheeler, “Analysis of Low-Cost Color Sensor Device Performance as Compared to Standardized Spectrophotometers,” *All Theses*, May 2022, Accessed: Jul. 09,

2022. [Online]. Available: https://tigerprints.clemson.edu/all_theses/3722.

[44] Thorlabs©, “Thorlabs - M1450F1 1450 nm, 0.86 mW (Min), Fiber-Coupled LED, 1000 mA, SMA,” *Fiber-Coupled LED, 1000 mA, SMA*, 2023. https://www.thorlabs.com/thorproduct.cfm?partnumber=M1450F1 (accessed Feb. 25, 2023).

[45] F. Faghiri and F. Ghorbani, “Colorimetric and naked eye detection of trace Hg2+ ions in the environmental water samples based on plasmonic response of sodium alginate impregnated by silver nanoparticles,” *J. Hazard. Mater.*, vol. 374, pp. 329–340, Jul. 2019, doi: 10.1016/J.JHAZMAT.2019.04.052.

[46] M. Wu *et al.*, “Nanogratings fabricated by wet etching assisted femtosecond laser modification of silicon for surface plasmon resonance sensing,” *Appl. Surf. Sci.*, vol. 603, p. 154446, Nov. 2022, doi: 10.1016/J.APSUSC.2022.154446.

[47] “850 - 2200nm, Manual Mini-Chrom Monochromator Gold Coated,” *IR Monochromator* , 2023. https://www.edmundoptics.com/p/850---2200nm-manual-mini-chrom-monochromator-gold-coated/13082/ (accessed Feb. 25, 2023).

[48] “Infrared Emitters and Detectors [SEN-00241] :: Micro JPM,” *Infrared Emitters and Detectors*, 2023. https://www.microjpm.com/products/infrared-emitters-and-detectors/ (accessed Feb. 25, 2023).

[49] “Thorlabs - CFC5-C Adjustable Fiber Collimator, FC/PC, f = 4.6 mm, 1050 - 1620 nm AR Coating,” *Adjustable Fiber Collimator*, 2023. https://www.thorlabs.com/thorproduct.cfm?partnumber=CFC5-C (accessed Feb. 25, 2023).

[50] B. Shariati, M. Ruiz, J. Comellas, and L. Velasco, “Learning from the optical spectrum: Failure detection and identification,” *J. Light. Technol.*, vol. 37, no. 2, pp. 433–440, Jan. 2019, doi: 10.1109/JLT.2018.2859199.

[51] V. Kumar and K. D. Gill, “Photometry: Colorimeter and Spectrophotometer,” *Basic Concepts Clin. Biochem. A Pract. Guid.*, pp. 17–20, 2018, doi: 10.1007/978-981-10-8186-6_5.

[52] H. Ren, J. De Chen, Y. Q. Li, and J. X. Tang, “Recent Progress in Organic Photodetectors and their Applications,” *Adv. Sci.*, vol. 8, no. 1, p. 2002418, Jan. 2021, doi: 10.1002/ADVS.202002418.

[53] P. S. Minz and C. S. Saini, “Comparison of computer vision system and colour spectrophotometer for colour measurement of mozzarella cheese,” *Appl. Food Res.*, vol. 1, no. 2, p. 100020, Dec. 2021, doi: 10.1016/J.AFRES.2021.100020.

[54] A. Jayshree and N. Vasudevan, “Bacterial enzyme based spectrophotometric determination of phthalate esters in drinking water stored in PET bottles,” *J. Food Meas. Charact. 2019 133*, vol. 13, no. 3, pp. 2190–2202, Apr. 2019, doi: 10.1007/S11694-019-00139-Y.

[55] V. Ganesh, K. Sahini, P. Poorna Basuri, and C. N. Nalini, “Review of analytical and bioanalytical techniques for the determination of first-line anticytomegalovirus

drugs," *Chinese J. Anal. Chem.*, vol. 50, no. 8, p. 100123, Aug. 2022, doi: 10.1016/J.CJAC.2022.100123.

[56] X. Hou, F. Xiao, J. Wang, and S. Amirkhanian, "Identification of asphalt aging characterization by spectrophotometry technique," *Fuel*, vol. 226, pp. 230–239, Aug. 2018, doi: 10.1016/J.FUEL.2018.04.030.

[57] B. P. Kafle, "Chemical analysis and material characterization by spectrophotometry," *Chem. Anal. Mater. Charact. by Spectrophotometry*, pp. 1–336, Jan. 2019, doi: 10.1016/C2017-0-02426-6.

[58] L. Kong *et al.*, "A novel smartphone-based CD-spectrometer for high sensitive and cost-effective colorimetric detection of ascorbic acid," *Anal. Chim. Acta*, vol. 1093, pp. 150–159, Jan. 2020, doi: 10.1016/J.ACA.2019.09.071.

[59] Z. Huang, Q. Liu, M. R. Pointer, M. R. Luo, B. Wu, and A. Liu, "White lighting and colour preference, Part 1: Correlation analysis and metrics validation:," *https://doi.org/10.1177/1477153518824789*, vol. 52, no. 1, pp. 5–22, Feb. 2019, doi: 10.1177/1477153518824789.

[60] V. G. Kolobrodov, G. Tymchik, and M. Kolobrodov, "Increase of spatial resolution of the optical spectrum analyzer," *https://doi.org/10.1117/12.2551636*, vol. 11369, pp. 79–85, Feb. 2020, doi: 10.1117/12.2551636.

[61] H. S. C. Freire, Y. Yamaguchi, and T. Kawanishi, "High-Speed Characterization of Parallel Mach-Zehnder Optical Modulators," *OECC/PSC 2019 - 24th Optoelectron. Commun. Conf. Conf. Photonics Switch. Comput. 2019*, Jul. 2019, doi: 10.23919/PS.2019.8817823.

[62] H. Dang *et al.*, "Investigation of Rayleigh-Assisted Coherent Optical Spectrum Analyzer," *2021 Optoelectron. Glob. Conf. OGC 2021*, pp. 149–152, 2021, doi: 10.1109/OGC52961.2021.9654372.

[63] L. Liu, X. Wu, G. Liu, T. Ning, X. Jian, and H. You, "Optoelectronic oscillator based-interrogation system for Michelson interferometric sensors," *Chinese Phys. B*, Jan. 2022, doi: 10.1088/1674-1056/AC4F59.

[64] A. Misra *et al.*, "Integrated High-Resolution Optical Spectrum Analyzer with Broad Operational Bandwidth," *IEEE Photonics Technol. Lett.*, vol. 32, no. 17, pp. 1061–1064, Sep. 2020, doi: 10.1109/LPT.2020.3011609.

[65] R. Wang *et al.*, "Precise dynamic characterization of microcombs assisted by an RF spectrum analyzer with THz bandwidth and MHz resolution," *Opt. Express, Vol. 29, Issue 2, pp. 2153-2161*, vol. 29, no. 2, pp. 2153–2161, Jan. 2021, doi: 10.1364/OE.415933.

[66] B. Patiño-Jurado, J. F. Botero-Cadavid, and J. Garcia-Sucerquia, "Analytical study of the numerical aperture of cone-shaped optical fibers: A tool for tailored designs," *Heliyon*, 2019, doi: 10.1016/j.heliyon.2019.e01612.

[67] E. Hecht, *Optics, 5e*, 5th ed. Pearson Education India, 2002.

[68] “Light-to-Frequency | ams.” https://ams.com/light-to-frequency (accessed Jul. 10, 2022).

[69] “Thorlabs - SLS201L Stabilized Fiber-Coupled Light Source w/ Universal Power Adapter, 360 - 2600 nm, 1/4"-20 Taps.” https://www.thorlabs.com/thorproduct.cfm?partnumber=SLS201L (accessed Jul. 17, 2022).

7. Conclusions and Recommendations

7.1 Conclusions

A fiber optics sensing platform for rapid on-site detection and monitoring of biological species at low concentrations, such as the anti-BSA, and chemical species such as the mercury, was designed, modeled, and constructed in this thesis. The state-of-the-art of the technology of the optical fiber sensors was explored, reported, and exploited throughout this document. As a result of this review, the most affordable, low-cost, and with potential for sensing low concentrations of substances methodologies based on fiber optics interferometers were identified and evaluated. In particular, cone-shaped optical fibers, E-SMS structures, and fiber with slanted ends were investigated as refractive index and temperature sensors. The results achieved for the cone-shaped optical fiber were discouraging due to it was verified that this technology is not a proper alternative to measure refractive index changes of chemical species at low concentrations without the tip modification with a thin film coating. However, cone-shaped optical fibers with tailored numerical aperture were obtained and used as illumination source for the sensing platform developed in this thesis.

As another contribution, this thesis presented the development of a simultaneous wavelength-modulated temperature and an intensity-modulated RI sensor based on optical fiber structure with a slanted end, which demonstrated a sensitivity within the range of formerly reported sensors of its kind, but being very inexpensive, compact, and easier to fabricate than others of its type. This structure was theoretically analyzed, numerically verified using COMSOL Multiphysics®, fabricated and experimentally proved to verify the feasibility of this simple structure to measure temperature changes and RI in NaCl solutions, with sensitivities of 21.5 pm/°C and -136 dBm/RIU in the RI range from 1.3095 to 1.3439.

Furthermore, the model that describes the formation of the optical spectrum as a result of the multimodal interference phenomenon and the wavelength-modulation due to RI fluctuation for the E-SMS fiber structure was reported in this thesis. Along with the theoretical analysis, it was included a numerical verification of the theoretical model using COMSOL Multiphysics®. This compact structure was fabricated to experimentally demonstrate the feasibility to tailor the geometry and the sensitivity of this simple technology and therefore reliably to measure RI in NaCl solutions; proving at the same time that the sensitivity of this cost-effective sensor can reach to 766 nm/RIU in the RI range from 1.3095 to 1.3439. This innovative and highly reproducible sensor was also investigated as a biosensor and applied to immunoassays (detection of an antigen/antibody binding), proving the feasibility of this simple structure to measure low concentration of biological species such as the bovine serum albumin (BSA). The analytical and experimental study performed demonstrated that the functionalized E-SMS biosensor provided high selectivity in the detection of Anti-BSA, with the ability to detect biological interactions up to 100 ng/mL, with a sensitivity of 2.3 nm/(µg/ml) and LOD of 0.7 ug/mL, which represents a 30% improvement with respect to the previous reported literature.

Once the E-SMS fiber structure and the optical fiber with a slanted end were identified as the most cost-effective, simple to construct, and relatively easy to implement refractive index sensors, these were functionalized and tested for selective detection of ions Hg^{2+} in water at low concentrations, up to 1 ppb. A very suitable functionalization protocol was evaluated immobilizing a CS/Fe_2O_3 thin film for the absorption of mercury ions on the sensitive surface of the fiber probes. The experimental results obtained in this thesis demonstrated the ability to detect selectively chemical interactions up to 1 ppb (0.001µg/mL) of Hg^{2+} in water for both types of sensors, with sensitivities of up 290 pm/(µg/mL) for the sensor based on the E-SMS structure and -0.07 dBm/(µg/mL) for the sensor based on the slanted end structure.

The ultimate contribution of this thesis was the design, modeling, fabrication, and test of the compact, portable, and rapid fiber optics sensing platform based on a spectrophotometer, with a working spectrum in the visible, which integrates the E-SMS sensor in order to detect and monitor low-concentrations of the biological and chemical species. Reporting the functional modules optimized, the experimental setup proven on the optical table, and the final prototype were obtained the results that verified the ability of this

technological contribution to detect interactions up to a minimum of 0.001 µg/mL (one part per billion) of Hg^{2+} in water and 0.1 µg/mL of Anti-BSA.

7.2 Recommendations

As a complement to the research that has been undertaken on this thesis, the following is recommended:

1. Although in the introduction chapter and throughout the text the possibility to measure Mycobacterium tuberculosis by using functionalized biosensors based on E-SMS structures was suggested, this purpose could not be achieved in the time of development time of this thesis, principally due to the delays in the import process of the biological reagents, as a consequence of the restrictions made by foreign governments in exporting these type of products because of the Covid-19 world health emergency. However, as indicated previously, the results of the optimized biosensor and the functionalization protocol for the immobilization of the model molecule BSA, and the detection of Anti-BSA, are important advances in the effort to detect low concentrations of other biological species such as Mycobacterium tuberculosis. The latter is the main objective of the Minciencias research project entitled “Plataforma Basada en Biosensores a Fibra Óptica para la Detección Rápida de tuberculosis y el Seguimiento Evolutivo de Pacientes” that partially supported the development of this doctoral thesis, which continues to be developed by our research group and probably lead to results susceptible to be published.

2. The fiber optics sensing platform developed in this thesis was tested under laboratory conditions. A performance evaluation in the field, in remote regions, should be carried out in order to determinate the functional limitations when concentrations of real samples of biological and chemical species are demanded in unregulated or loosely controlled environments.

3. A compact and portable illumination source based on a power LED with minimum optical losses should be designed and implemented, with the aim of being able to evaluate the sensor based on fiber optics with a slanted end within the sensing

platform for monitoring the chemical and biological substances. This sensor is much easier and faster to fabricate than the E-SMS fiber sensor is; therefore, it is worth to integrate with the portable sensing prototype.